Harsh Environment Silicon Carbide UV Sensor and Junction Field-Effect Transistor

By

Wei-Cheng Lien

A dissertation submitted in partial satisfaction of the

requirements for the degree of

Doctor of Philosophy

in

Applied Science & Technology

in the

Graduate Division

of the

University of California, Berkeley

Committee in charge:

Professor Albert P. Pisano, Chair
Professor Tsu-Jae King Liu
Professor Elad Alon

Fall 2013

Harsh Environment Silicon Carbide UV Sensor and Junction Field-Effect Transistor

Copyright © 2013

by

Wei-Cheng Lien

Abstract

Harsh Environment Silicon Carbide UV Sensor and Junction Field-Effect Transistor

by

Wei-Cheng Lien

Doctor of Philosophy in Applied Science & Technology

University of California, Berkeley

Professor Albert P. Pisano, Chair

A harsh environment can be defined by one or more of the following: High temperature, high shock, high radiation, erosive flow, and corrosive media. Among all the harsh environment applications, high temperature applications have drawn lots of attention due to the emerging activity in automotive, turbine engine, space exploration and deep-well drilling telemetry. Silicon carbide has become the candidate for these harsh environment applications because of its wide bandgap, excellent chemical and thermal stability, and high breakdown electric field strength. This dissertation details the two building blocks of high-temperature UV sensing chip, namely Ultraviolet sensor and transistors. High temperature performance of silicon carbide metal-semiconductor-metal UV sensor is characterized at high temperatures for the first time. The sensor exhibits high photo-to-dark current ratio and fast rise and fall time even at high temperatures. Complementary SiC junction field-effect transistors of different gate configurations are proposed, fabricated and characterized from room temperature to 600 °C for the first time. High intrinsic gains at high temperatures suggest that complementary junction field-effect transistors are suitable devices for high temperature operational amplifier.

Contents

Contents **i**

List of Figures **iv**

List of Tables **x**

Acknowledgements **xii**

1. Introduction **1**

1.1 Harsh Environment Sensing Application……………………………………...1

1.2 Silicon Carbide……………………………………………………………...2

1.3 SiC Sensors for High Temperature Application………………………………5

1.3.1 UV Sensor…………………………………………………………...5

1.3.2 Pressure Sensor……………………………………………………...5

1.4 SiC Electronics Low Voltage High Temperature Application………………..6

1.5 High Temperature Effects in 4H-SiC…………………………………………8

1.6 Research Objective and Thesis Overview……………………………………9

1.7 References……………………………………………………………………10

2. Silicon Carbide Metal-Semiconductor-Metal Ultraviolet Photodetectors **14**

2.1 Introduction…………………………………………………………………..14

2.2 Physics of MSM Photodetectors……………………………………………..15

2.3 4H-SiC MSM Photodetectors………………………………………………..17

2.3.1 Fabrication Process and Characterization Methods………………..17

2.3.2 Characterization of 4H-SiC Thin Films……………………………18

2.3.3 Characterization of 4H-SiC MSM Photodetector…………………19

2.4 Antireflection Layer Using Nanostructure…………………………………...23

2.5 Summary……………………………………………………………………..25

2.6 References……………………………………………………………………26

3. Silicon Carbide N-Channel Raised Gate Junction Field-Effect Transistors 28

3.1 Introduction…………………………………………………………………..28

3.2 Physics of JFET……………………………………………………………...28

3.3 Fabrication Process…………………………………………………………..32

3.4 Metallization of N-Channel Raised Gate JFET……………………………...37

3.5 Electrical Properties of N-Channel Raised Gate JFET………………………43

3.5.1 Characterization of N-JFET at Room Temperature………………..43

3.5.2 Characterization of N-JFET at High Temperatures………………..45

3.5.3 Reliability……………………………………………………………..48

3.6 TCAD Simulation of N-Channel Raised Gate JFET………………………...50

3.7 SPICE Parameter Extraction and Device Modeling…………………………53

3.8 Summary……………………………………………………………………..55

3.9 Reference…………………………………………………………………….55

4. Silicon Carbide Complementary Buried Gate Junction Field-Effect Transistors 59

4.1 Introduction…………………………………………………………………..59

4.2 Design of Complementary Buried Gate JFET……………………………….59

4.3 Fabrication Process…………………………………………………………..64

4.4 Metallization of Complementary Buried Gate JFET………………………...68

4.5 Electrical Properties of N-Channel Buried Gate JFET………………………71

4.6 Electrical Properties of P-Channel Buried Gate JFET……………………….73

4.6.1 Characterization of P-Channel Buried Gate JFET at Room Temperature…………………………………………………………………...73

4.6.2 Characterization of P-Channel Raised Gate JFET at High Temperature…………………………………………………………………...75

4.7 Summary…………………………………………………………………..79

4.8 Reference…………………………………………………………………79

5. Conclusion and Future Work 82

5.1 Contributions of This Work…………………………………………………82

5.2 Integrated SiC Sensor Design Challenges…………………………………...83

5.3 Reference…………………………………………………………………83

List of Figures

Figure 1.1: The structure of SiC crystal…………………………………………………...2

Figure 1.2: Three most common polytypes of silicon carbide. *Copyright: Dr. Christopher S. Roper* ……………………………………………………………………………...3

Figure 1.3: Bi-layer stacking for the SiC polytypes 3C, 2H, 4H, and 6H………………..3

Figure 1.4: Calculated energy bandgap of Si, 6H-SiC, and 4H-SiC versus temperature…8

Figure 1.5: Intrinsic carrier concentration in Si, 6H-SiC, and 4H-SiC versus temperature……………………………………………………………………………..9

Figure 2.1: Schematic of MSM photodetector…………………………………………...15

Figure 2.2: (a) The MSM photodetector is considered as two back-to-back Schottky barriers. Energy-band diagrams of MSM PDs at equilibrium (b) with n-type semiconductor layers and (c) with p-type semiconductor layers………………………...16

Figure 2.3: Energy-band diagrams of MSM PDs for p-type semiconductor (a) without light and (b) with light at flat-band voltage……………………………………………...16

Figure 2.4: (a) Schematic and (b) optical image of 4H-SiC MSM PDs…………………17

Figure 2.5: Schematic of time-resolved measurement system…………………………...18

Figure 2.6: (a) Cross-sectional TEM image and (b) electron diffraction pattern of epitaxial p-type 4H-SiC layer…………………………………………………………19

Figure 2.7: The transmission spectrum (left y axis) and $(\alpha h\upsilon)^2$ (right y axis) vs. $h\upsilon$ plot of 4H-SiC substrates………………………………………………………………...19

Figure 2.8: I-V curves of the 4H-SiC MSM PDs measured in the dark and under 325-nm illumination at room temperature……………………………………………………...20

Figure 2.9: The time dependence of the photocurrent and dark current of SiC MSM PDs at 25 ℃ under a 5 V bias……………………………………………………………...21

Figure 2.10: (a) PDCR value and (b) responsivity as function of temperature under a 5 V bias……………………………………………………………………………….21

Figure 2.11: The time dependence of the photocurrent and dark current of SiC MSM PDs at 450 ℃ under a 5 V bias……………………………………………………………….22

Figure 2.12: The transient photocurrent of SiC MSM PDs at room temperature and 400 ℃ under a 5 V bias………………………………………………………………………22

Figure 2.13: (a) Top view and (b) cross-sectional SEM image of ZnO NRA/SiC layers……………………………………………………………………………………..24

Figure 2.14: Reflectance spectra of (a) bare SiC MSM PDs and (b) ZnO NRA/ SiC MSM PDs with a wide range of AOIs……………………………………………………….25

Figure 2.15: FDTD simulation of time-averaged and normalized TE electric field distribution at 532 nm (a) without and (b) with ZnO NRAs. The insets in (a) and (b) are the enlarged images at the top SiC surface…………………………………………25

Figure 3.1: Visualization of various phases of JFET operation and the corresponding I_D-V_D characteristics at V_{GS} = 0 V. Note the SiC substrate serves as the body biasing point. The blue color in schematic represents the depletion regions, and the yellow color shows the channel region. The shape of the channel is for the purpose of demonstration and it is not the real situation…………………………………………………………………...31

Figure 3.2: Schematic of a lateral n-channel raised gate 4H-SiC JFET…………………32

Figure 3.3: Completed fabrication process flow of 4H-SiC JFET and MSM photodetectors……………………………………………………………………………33

Figure 3.4: Simulated doping profile of heavily doped drain and source region……......34

Figure 3.5: (a) Cross-sectional scanning TEM image (b) Electron diffraction of implanted area after annealing at 1450 ℃ under Argon atmosphere for 30 minutes……………….35

Figure 3.6: AFM images of SiC samples before annealing and after annealing at 1450 ℃ under Argon atmosphere for 30 minutes………………………………………………...35

Figure 3.7: Fabricated 3” 4H-SiC wafer…………………………………………………36

Figure 3.8: High temperature probe station……………………………………………...36

Figure 3.9: HP 4156B semiconductor parameter analyzer and Agilent B2912A precision source/measurement unit………………………………………………………………...37

Figure 3.10: Ideal Ohmic contact of metal with (a) p-type semiconductor and (b) n-type semiconductor……………………………………………………………………………38

Figure 3.11: Several metal workfunctions compared with the 4H-SiC band diagram…..38

Figure 3.12: Optical image of TLM structure…………………………………………39

Figure 3.13: Measure I-V curves of metal and n-type 4H-SiC before and after RTA annealing for TLM structure with d = 80 μm…………………………………………40

Figure 3.14: Measured resistance between contacts vs. different distances at room temperature of Ti/Ni/TiW metal stacks and n-type 4H-SiC……………………………..41

Figure 3.15: Temperature dependences of specific contact resistance of Ti/Ni/TiW metal stacks to n^+ 4H-SiC……………………………………………………………………42

Figure 3.16: Measure I-V curves of metal and p-type 4H-SiC for TLM structure with d = 5 μm…………………………………………………………………………………...43

Figure 3.17: Optical image of a n-channel raised gate 4H-SiC JFET with L = 10 μm and W = 100 μm………………………………………………………………………………44

Figure 3.18: I_{DS}-V_{DS} characteristics of a n-channel 4H-SiC JFET (a) before RTA (b) after RTA under different V_{GS} and with W/L= 100 μm/10 μm at 25 ℃………………………44

Figure 3.19: (a) I_{DS}-V_{GS} (b) $\sqrt{I_{DS}}$-V_{GS} characteristics of a n-channel 4H-SiC JFET with W/L= 100 μm/10 μm and V_{DS} = 20 V at 25 ℃……………………………………..44

Figure 3.20: I_{DS}-V_{DS} characteristics of a n-channel 4H-SiC JFET under different V_{GS} and with W/L= 100 μm/10 μm (a) at 110 ℃ (b) at 210 ℃ (c) at 300 ℃ (d) at 400 ℃ (e) at 500 ℃ (f) at 550 ℃ (g) at 600 ℃. (h) Temperature dependences of I_{Dsat} of a n-channel 4H-SiC JFET at V_{GS} = 0 V and with W/L= 100 μm/10 μm……………………………...46

Figure 3.21: (a) I_{DS}-V_{GS} (b) $\sqrt{I_{DS}}$-V_{GS} characteristics of a n-channel 4H-SiC JFET under V_{DS} = 20 V and with W/L= 100 μm/10 μm at different temperatures……………………47

Figure 3.22: Temperature dependence of threshold voltage of a n-channel 4H-SiC JFET with W/L= 100 μm/10 μm…………………………………………………….….47

Figure 3.23: Temperature dependence of transconductance and intrinsic gain of of a n-channel 4H-SiC JFET with W/L= 100 μm/10 μm……………………………………..48

Figure 3.24: (a) I_{DS}-V_{DS} characteristics at V_{GS} = 0 V and (b) I_{DS}-V_{GS} characteristics at V_{DS} = 20 V during 0, 25th, 50th, 75th, and 90 hours of electrical operation at 540 ℃ for a n-channel 4H-SiC JFET with W/L = 100 μm/10 μm ……………………………………49

Figure 3.25: Normalized g_m versus test time at 540 ℃ through 90 hours for a n-channel 4H-SiC JFET with W/L = 100 μm/10 μm……………………………………………..50

Figure 3.26: Optical image of a n-channel 4H-SiC JFET with W/L = 100 μm/10 μm after thermal reliability test at 540 ℃ after 90 hours………………………………………50

Figure 3.27: Raised gate JFET structure generated by the Sentaurus structure editor…..52

Figure 3.28: Measured and Simulated (a) I_{DS}-V_{DS} characteristics at V_{GS} = 0 V and (b) I_{DS}-V_{GS} characteristics at V_{DS} = 20 for n-channel 4H-SiC JFETs with W/L = 100 μm/10 μm at 25 and 600 ℃……………………………………………………………………52

Figure 3.29: Arrhenius plot of log of drain leakage current versus 1/T at V_{GS} = -10 V of a n-channel 4H-SiC JFET with W/L = 100 μm/10 μm……………………………………52

Figure 3.30: Modeled and measured I_{DS}-V_{DS} characteristics of a n-channel 4H-SiC JFETs under different V_{GS} and with W/L= 100 μm/10 μm (a) at 110 ℃ (b) at 210 ℃ (c) at 300 ℃ (d) at 400 ℃ (e) at 500 ℃ (f) at 600 ℃. The black dot lines are modeled devices and the red solid lines are measured devices. From the top curve to the bottom curve, V_{GS} are 0, -2, -4, -6, -8 V, respectively………………………………………………………...54

Figure 4.1: Buried gate JFET structure generated by the Sentaurus structure editor……60

Figure 4.2: Simulated I_{DS}-V_{GS} of n-channel JFETs with L = 8 μm and (a) different channel doping with fixed channel depth of 250 nm (b) different channel depth with fixed channel doping of 2.5×10^{17} cm^{-3} at 25 ℃..………………………………………………...60

Figure 4.3: Simulated I_{DS}-V_{GS} of p-channel JFETs with L = 8 μm and (a) different channel doping with fixed channel depth of 400 nm (b) different channel depth with fixed channel doping of 1.5×10^{17} cm^{-3} at 25 ℃..………………………………………………...61

Figure 4.4: Simulated I_{DS}-V_{GS} of a (a) n-channel (b) p-channel JFET with L = 8 μm…...61

Figure 4.5: Temperature dependence of (a) carrier mobility and (b) degree of ionization...64

Figure 4.6: Schematic of 4H-SiC complementary JFETs………………………………..65

Figure 4.7: Completed fabrication process flow of 4H-SiC c-JFETs……………………66

Figure 4.8: Simulated phosphorous doping profile in the p-channel area with N_A = 1.5×10^{17} cm^{-3}……………………………………………………………………………67

Figure 4.9: Simulated aluminum doping profile in the n-channel area with N_D = 2.5×10^{17} cm^{-3}…………………………………………………………………………………67

Figure 4.10: SEM image of etching pits after thermal annealing at 1550 ℃ for 15 minute……………………………………………………………………………………68

Figure 4.11: Measure I-V curves of metal and n-type 4H-SiC before and after RTA annealing for TLM structure with d = 5 μm…………………………………………..69

Figure 4.12: Temperature dependences of specific contact resistance of Ni/Ti/Al/TiW metal stacks to n^+ 4H-SiC………………………………………………………..69

Figure 4.13: Measure I-V curves of metal and p-type 4H-SiC before and after RTA annealing for TLM structure with d = 20 μm…………………………………………70

Figure 4.14: Temperature dependences of specific contact resistance of Ni/Ti/Al/TiW metal stacks to p^+ 4H-SiC………………………………………………………..71

Figure 4.15: Optical image of a n-channel buried gate 4H-SiC JFET with L = 10 μm and W = 100 μm……………………………………………………………………………72

Figure 4.16: I_{DS}-V_{DS} characteristics of a n-channel buried gate 4H-SiC JFET under different V_{GS} and with W/L= 100 μm/10 μm at 25 ℃…………………………………...72

Figure 4.17: I-V characteristics of pn junction in the n-channel buried gate 4H-SiC JFET structure.………………………………………………………………………………73

Figure 4.18: Optical image of a p-channel buried gate 4H-SiC JFET with L = 10 μm and W = 100 μm……………………………………………………………………………74

Figure 4.19: $|I_{DS}|$-V_{DS} characteristics of a p-channel 4H-SiC JFET under different V_{GS} and with W/L= 100 μm/10 μm at 25 ℃…………………………………………………74

Figure 4.20: (a) $/I_{DS}|$-V_{GS} (b) $\sqrt{|I_{DS}|}$-V_{GS} characteristics of a p-channel 4H-SiC JFET with W/L= 100 μm/10 μm and V_{DS} = -20 V at 25 ℃……………………………………75

Figure 4.21: I_{DS}-V_{DS} characteristics of a p-channel 4H-SiC JFET under different V_{GS} and with W/L= 100 μm/10 μm (a) at 110 ℃ (b) at 210 ℃ (c) at 300 ℃ (d) at 400 ℃ (e) at 500 ℃ (f) at 550 ℃ (g) at 600 ℃. (h) Temperature dependences of I_{Dsat} of a p-channel 4H-SiC JFET at V_{GS} = 0 V and with W/L= 100 μm/10 μm…………………………...76

Figure 4.22: $|I_{DS}|$-V_{GS} characteristics of a p-channel 4H-SiC JFET under V_{DS} = -20 V and with W/L= 100 μm/10 μm at different temperatures……………………………………77

Figure 4.23: Temperature dependence of threshold voltage of a p-channel 4H-SiC JFET with W/L= 100 μm/10 μm…………………………………………………………..78

Figure 4.24: Temperature dependence of transconductance and intrinsic gain of of a p-channel 4H-SiC JFET with *W*/*L*= 100 μm/10 μm……………………………………..78

List of Tables

Table 1.1: High temperature electronics applications……………………………………..2

Table 1.2: Mechanical properties of Si and wide bandgap semiconductors. If the thermal expansion coefficient has two values, the first one is along the a-axis and the second one is along the c-axis…………………………………………………………………………4

Table 1.3: Electrical properties of Si and wide bandgap semiconductors. If the electron mobility has two values, the first one is perpendicular to the c-axis and the second one is parallel to the c-axis………………………………………………………………………4

Table 1.4: A sampling of published single transistors for high temperature applications...7

Table 2.1: Response time of fabricated 4H-SiC MSM photodetectors………………….23

Table 3.1: Specific contact resistance measurements on 4H-SiC in the literature………41

Table 3.2: Sheet resistance and specific contact resistance of Ti/Ni/TiW metal stacks and n-type 4H-SiC at different temperatures…………………………………………………42

Table 3.3: Extracted parameters of n-channel raised gate 4H-SiC JFET with W/L= 100 μm/10 μm at various temperatures. g_m, R_{on}, r_o , λ and $g_m r_o$ is based on V_{GS} = 0 V. I_{Dsat}/I_{off} is the ratio of current at V_{GS} = 0 V and V_{GS} = -9 V……………………………………….48

Table 3.4: The extracted SPICE parameters of a n-channel 4H-SiC JFET with W/L= 100 μm/10 μm from 25 to 600 °C………………………………………………………….53

Table 4.1: Optimized parameters of complementary JFETs with L = 10 μm. g_m, r_o, and $g_m r_o$ is based on V_{GS} = 0 V…………………………………………………………….62

Table 4.2: Fitting parameters for low field mobility of 4H-SiC…………………………63

Table 4.3: Sheet resistance and specific contact resistance of Ni/Ti/Al/TiW metal stacks and n-type 4H-SiC at different temperatures……………………………………………..70

Table 4.4: Sheet resistance and specific contact resistance of Ni/Ti/Al/TiW metal stacks and p-type 4H-SiC at different temperatures……………………………………………..71

Table 4.5: Extracted parameters of a p-channel buried gate 4H-SiC JFET with W/L= 100 μm/10 μm at various temperatures. g_m, R_{on}, r_o , λ and $g_m r_o$ is based on V_{GS} = 0 V. I_{Dsat}/I_{off} is the ratio of current at V_{GS} = 0 V to current at V_{GS} = 7 V....................................79

Acknowledgments

There are many people who deserve my acknowledgments during the three and half years of my Ph. D. study at the University of California at Berkeley. I would like to express my sincere thanks to my advisor, Professor Albert P. Pisano. He is a caring advisor offering me endless help on my research, course work and even life at Berkeley. He gives me the freedom to explore interesting research topics and encourages me, rather than blaming me, when I am frustrated and make mistakes.

I am also grateful for the support from my dissertation committee members Professor Tsu-Jae King Liu and Professor Elad Alon.

Professors Debbie Senesky, Roya Maboudian, Ali Javey, and Roger Howe have provided me with many inspiring ideas and invaluable advice. The members of the Pisano lab, past and present, have taught me the skills, techniques and valuable discussions for this work. In addition, Dr. Louis Hutin and Nattapol Damrongplasit from Professor Tsu-Jae King Liu's group, and Jun-Chau Chien from Professor Ali Niknejad's group, and Yang Lin and Wei-Chun Li from Professor Clark Nguyen's group shared their knowledge and offered valuable help for me. I would like to thank the staff at Berkeley Marvell Nanolab for providing much assistance related to operating the machines in Nanolab. I also want to thank the staff of the BSAC and ERSO office for helping with purchase orders and grant administration.

My wonderful friends, Fabian Goericke, Matt Chan, Yegan Erdem, Albert Gutes, Ting-Ta Yen, Chih-Ming Lin, Yun-Ju Lai, Ting-Ying Chung, Chih-Wei Chu, Stefano Fissolo, Kuo-Ken Huang and Terry Tsai, deserve my special thanks for their unremitting support and encouragement with everything.

Finally, and most importantly, I want to express my deepest gratitude to my parents and two sisters for their love.

Chapter 1

Introduction

1.1 Harsh Environment Sensing Application

Recently, much research effort has focused on advancing renewable energy resources, such as solar, hydro, wind and geothermal energy. While developing these new technologies, reducing inefficiencies in generation and transmission should be considered. For example, the total energy lost is 61% of energy supply in U.S. in 2012 [1]. One method of addressing the inefficiencies in energy use is through the development of harsh environment sensing technology. Power systems can be advanced by integration of electronics (e.g., communication, signal processing, microactuator control, etc.) to operate at high temperature [2, 3]. Specifically, smart harsh environment electronic sensing systems enable real-time condition based monitoring of temperature and incomplete combustion, and reduce emission of greenhouse gases (NO_x and CO_2) in gas turbine system or combustion engine [4, 5]. In addition, wireless technology helps telemetry systems to guide deep-well oil drilling operation or monitors the subsurface environments found in geothermal power plants.

A harsh environment can be defined by one or more of the following: High temperature (> 350 ℃), high shock (> 50,000 g), high radiation (> 100 Mrads), erosive flow, and corrosive media [6]. Silicon is a widely used semiconductor material because of such factors as its high quality, stable oxide, and low cost. However silicon-based microelectronics are not suitable for harsh environments, because the electronic properties of silicon degrade above 300 ℃ due to the more intrinsic carrier presented than dopant carriers and mechanical properties degrade above 600 ℃ due to decline in its elastic modulus [3]. As the need increases for electronics and microelectromechanical systems (MEMS) devices suitable for harsh environment applications, including automobile, aerospace, nuclear and military purposes, several technologies such as silicon-on-insulator (SOI) or wide bandgap (WBG) electronics are needed. SOI technology can extend the CMOS operating temperature due to reduce leakage and less parasitic bipolar action [7]. A wide bandgap material has large energy bandgap of 3 eV so the generation of intrinsic carriers will not surpass the dopant carriers at high temperature.

In order to realize integration of the sensing system, the building blocks of the sensor system, such as sensors and transistors, need to be developed. Among all the harsh environment applications, high temperature applications have drawn lots of attention due to the emerging activity in several areas (Table 1.1) [3]. In this work, we focus on

developing the sensor and electronics for high temperature application. Silicon carbide (SiC) has been chosen as the base semiconductor material for this work due to its wide bandgap, high electric field breakdown strength, high thermal conductivity, and high saturated carrier drift velocity [8].

Application	Area	Peak ambient (°C)	Chip power (kW)	Target technology
Autimotive	On-cylinder & Exhaust pipe	600	< 1	WBG
Turbine engine	Sensors, telemetry, control	600	< 1	WBG
	Electric actuation	600	> 10	WBG
Spacecraft	Power management	300	> 10	WBG
	Venus & Mercury exploration	550	1	WBG
Industrial	High temperature processing	600	< 1	SOI & WBG
Deep-well drilling telemetry	Oil and gas	300	< 1	SOI & WBG
	geothermal	600	< 1	WBG

Table 1.1: High temperature electronics applications.

1.2 Silicon Carbide

The silicon carbide unit cell is a tetrahedron consisting of four carbon atoms with a silicon atom in the center, as shown in Figure 1.1. There are approximately 200 polytypes of SiC existing in the world [9]. Figure 1.2 shows the three most common polytypes of silicon carbide, consisting of different stacking sequences of SiC bilayer. They are cubic (3C, β-SiC) and hexagonal (H, α-SiC) with the number denoting the number of SiC bilayer stackings [10]. Because of the possible stacking sequences of SiC bilayer, there are lattice sites in SiC that have a surrounding layer stacking in hexagonal form and others with cubic form, which are denoted hexagonal sites and cubic sites, respectively [11]. Figure 1.3 shows that 3C-SiC has one cubic site and 2H-SiC includes only one hexagonal site. 4H-SiC has one hexagonal and one cubic site, while 6H-SiC exhibits one hexagonal and two cubic sites. 4H-SiC and 6H-SiC polytypes already have commercially available wafers and epitaxy, while 3C-SiC is the only polytype that can be grown heteroepitaxially on a Si wafer. The basic mechanical and electrical properties of the three SiC polytypes, as well as those for Si, GaN, AlN, and diamond are shown in Table 1.2 and 1.3 [11-13].

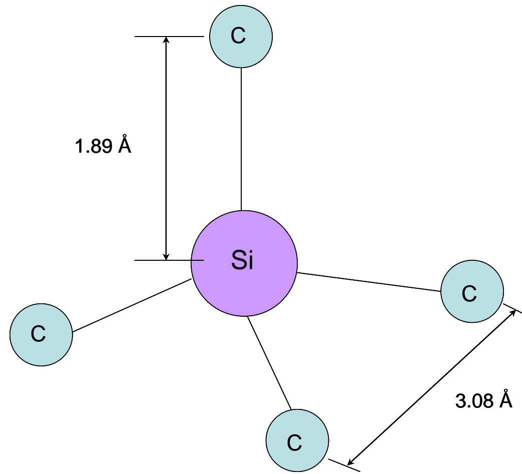

Figure 1.1: The structure of SiC crystal.

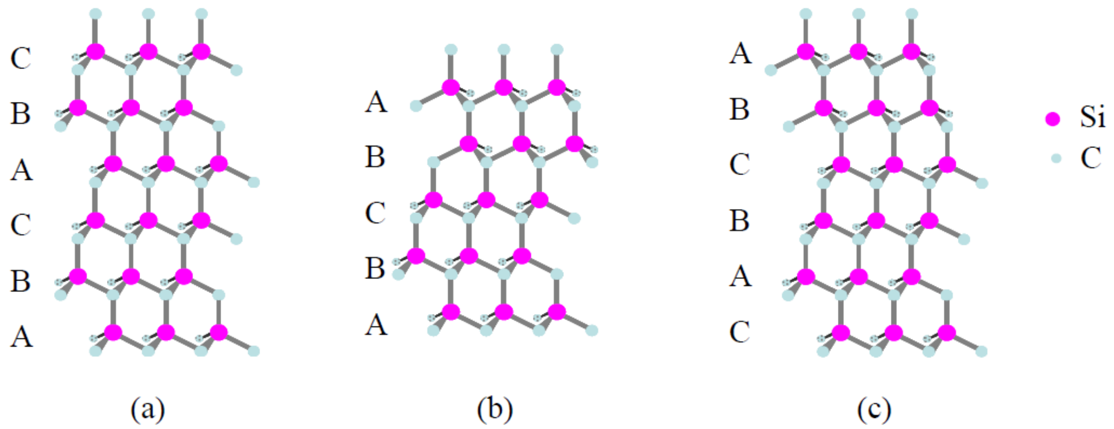

Figure 1.2: Three most common polytypes of silicon carbide [10]. *Copyright: Dr. Christopher S. Roper*

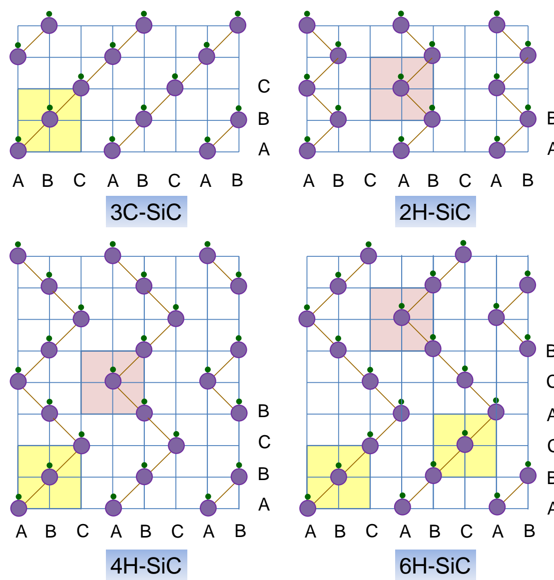

Figure 1.3: Bi-layer stacking for the SiC polytypes 3C, 2H, 4H, and 6H [11].

	Si	3C-SiC	6H-SiC	4H-SiC	2H-GaN	2H-AlN	Diamond
Lattice a (Å)	5.43	4.36	3.08	3.08	3.189	3.112	3.567
Lattice c (Å)	NA	NA	15.12	10.08	5.185	4.982	NA
Thermal expansion coefficient (10^{-6}/K)	2.6	3.28	3.35/3.25	3.3/3.16	5.59/3.17	5.27/4.15	0.8
Density (g/cm^3)	2.33	3.21	3.21	3.21	6.15	3.23	3.5
Thermal conductivity (W/cm K)	1.5	3.6	4.9	4.9	1.3	2.85	20
Melting point (°C)	1420	2830	2830	2830	2500	3000	4000
Mohs hardness	7	9	9	9		7	10

Table 1.2: Mechanical properties of Si and wide bandgap semiconductors. If the thermal expansion coefficient has two values, the first one is along the a-axis and the second one is along the c-axis.

	Si	3C-SiC	6H-SiC	4H-SiC	2H-GaN	2H-AlN	Diamond
Energy bandgap (eV)	1.12	2.4	3.0	3.23	3.4	6.2	5.6
Breakdown field(MV/cm)	0.25	2.5	2.5	2.2	3.0	2.0	20
Electron saturation velocity (10^7 cm/s)	1.0	2.5	2.0	2.0	2.5	2.0	2.7
Electron mobility (Cm/V s)	1400	1000	500/100	950/1150	1245	135	2200
Hole mobility (cm/V s)	600	50	80	120	370	14	1600
Dielectric constant	11.9	9.7	10.0	10.0	9.5	8.5	5.5

Table 1.3: Electrical properties of Si and wide bandgap semiconductors. If the electron mobility has two values, the first one is perpendicular to the c-axis and the second one is parallel to the c-axis.

Owing to its superior mechanical properties, SiC is quite suitable for Microelectromechanical systems (MEMS). SiC based MEMS devices have been previously used as temperature and pressure sensors in a high temperature environment [14], high-g accelerometers [15], biomedical sensors [16], and strain sensor [5]. SiC may also be suitable for high frequency MEMS resonators as micromechanical oscillators and

filters due to its high E/ρ ratio. The resonant frequency of a micromachined device can be expressed as

$$\omega = Cf\sqrt{\frac{E}{\rho}} \tag{1.1}$$

where C is constant, f is a function of Poisson's ratio, E is the material Young's modulus and ρ is the material density. SiC has been successfully used to fabricate Lamé mode MEMS resonators for signal processing [17].

SiC may be used for high temperature, high power, high frequency and radiation resistance electronics applications. For example, its wide bandgap makes SiC desirable for electronics in high temperature environments. Additionally, the breakdown electric field strength (E_{max}) is perhaps the most important factor for high power applications: the E_{max} of SiC is ten times that of silicon. As high-frequency devices, the saturated electron drift velocity of SiC is twice that of silicon, thereby enabling microwave devices to reach high channel currents [18].

1.3 SiC Sensors for High Temperature Application

SiC sensor technology has been significantly improved in material growth technology and processing over the last few years [19]. Several SiC sensor platforms have been developed for high temperature applications, such as ultraviolet (UV) sensor, gas sensor, pressure sensor. The following sections report some device performance of the SiC sensors.

1.3.1 UV Sensor

A SiC UV sensor is mainly based on the pn diode, and was the first wide bandgap photodetectors to reach the market [13, 20, 21]. The main advantage is the low reverse current, which is ~ 10^{-13} A/cm^2 at room temperature, 10^{-9} A/cm^2 at 200 ℃ and ~ 2×10^{-7} A/cm^2 at 350 ℃ at -10 V for 6H-SiC photodiode [20]. At 25 ℃, the peak responsivity typically falls between 0.15-0.175 A/W at 270 nm, corresponding to a quantum efficiency of 70-85%. When the temperature increases, the peak response redshifts and long wavelength responsivity increases. The corresponding quantum efficiency varies between 82 and 96% from -50 to 450 ℃ [13, 20].

Another type of photodetector (PD), metal-semiconductor-metal (MSM) PD, has also been developed for operating temperatures up to 200 ℃ using nanocrystalline SiC deposited by ion-beam assisted deposition [22]. MSM offers high speed operation and can be readily integrated with optoelectronic and MEMS for signal detection.

1.3.2 Pressure Sensor

Conventional Si-based pressure sensors are temperature limited and require a cooling system, while a SiC-based pressure sensor can operate at a higher temperature [5, 23]. Both bulk and thin film SiC are employed as a platform for SiC pressure sensors. Bulk micromachining of SiC diaphragms have been employed for the pressure sensor design. A polycrystalline SiC capacitive pressure sensor has been fabricate and packaged in a high-temperature ceramic package [24]. It can detect ~ 5.17 MPa with a sensitivity of 251 μV/psi at 300 °C, and ~ 0.7 MPa with a sensitivity of 7.2 fF/psi at 574 °C. A 6H-SiC diaphragm using photoelectrochemically etching and epitaxially grown n-type 6H-SiC was used to create a 6H-SiC piezoresistive pressure sensor [25]. It can detect 6.9 MPa at 600 °C with minimum junction leakage and no plastic deformation.

3C-SiC thin film grown on Si substrate with potential large scale fabrication can also be used for a pressure sensor. A polycrystalline SiC capacitive pressure sensor grown on Si substrate has been proposed [26]. The linear range of capacitance change with applied pressure is between 22.2 and 31.2 per inch absolute pressure (PSIA) at 500 °C. The sensitivity is 0.62 pF/PSIA at 400 °C and decreases to 0.53 pF/PSIA at 500 °C.

1.4 SiC Electronics Low Voltage High Temperature Application

Much progress has been made for the development of high temperature SiC electronic devices for low voltage or low power analog and digital circuit applications. D. M Brown et al. from Generic Electric Company reported a 6H-SiC operational amplifier based on the n-channel enhancement and depletion mode metal-oxide-semiconductor field effect transistors (MOSFETs). It operates up to 300 °C with a low frequency gain of 53 dB and the bandwidth of 269 kHz [27]. A monolithic 6H-SiC CMOS digital integrated circuits has been developed [28]. The threshold voltages of PMOS and NMOS at 300 °C are -6 V and 0.5 V, respectively. The effect channel mobilities of PMOS and NMOS at 300 °C are 7.01 and 20.8 cm^2/Vs, respectively. Raytheon has been developed the 4H-SiC CMOS integrated circuit with operating temperature of 400 °C [29]. The gate leakage current is less than 1 pA at 350 °C.

A differential amplifier using 6H-SiC metal-semiconductor field effect transistor (MESFETs) and thick film hybrid technology has been reported [30]. It has a voltage gain of 61 dB, common mode rejection ratio (CMRR) of 60 dB, bandwidth of 910 kHz, offset voltage of 151 mV, and power dissipation of 178 mW at 350 °C. NASA Glenn Research Center has demonstrated a 4H-SiC MESFET based hybrid, ultra high frequency band differential oscillator [31]. The oscillator delivers 4.9 dBm at 453 MHz at 475 °C. M. Alexandru et al. designed and characterized 4H-SiC MESFET based inverter, NAND and NOR gates that operate up to 300 °C [32]. 4H-SiC bipolar junction transistor (BJT) with operating temperature up to 500 °C have been reported [33]. The current gain is approximately 42 at 500 °C using Ti/TiW/Al metallization.

Numerous studies exist on SiC junction field effect transistor (JFETs) for high temperature applications, because the JFET structure is based on pn junction which is

free of oxide reliability and Schottky contact stability existing in MOSFET and MESFET in the temperature range of 500 ℃. A back gate n-channel 6H-SiC JFET has been developed and modeled up to 400 ℃ [34]. Daimler Benz Research Laboratories reported the 6H-SiC implanted-gate n-channel JFETs with operating temperature of 400 ℃. The transconductance is approximately 0.16 mS/mm and on/off saturation drain current ratio is ~ 106 at 400 ℃. NASA Glenn Research Center has demonstrated very stable long term operation of 6H-SiC n-channel JFETs at 500 ℃ for more than 3007 hours [35]. A 600 ℃ of NAND and NOR gates have also been developed at this center [36]. An AC coupled differential amplifier using 4H-SiC vertical JFET has been developed, and the voltage gain is 47.8 dB with CMRR of ~ 45 dB at 500 kHz at 450 ℃ [37]. A. C. Patil et al. has reported a 6H-SiC JFET based two stage differential amplifier with a voltage gain of 69.2 dB and unit gain frequency of 1.4 MHz at 576 ℃ [38].

Table 1.4 below summarizes the maximum operating temperature of recent works for low voltage high temperature single transistors including SiC, GaN and diamond. SiC shows promising preliminary results in high temperature electronics. However, many challenges still need to be address before the commercialization. First, the process of making SiC based electronics devices is not as mature as that for Si CMOS, because the design and process approaches for Si based electronics can not be directly used for SiC based electronics due to different materials properties. Besides, the reliability and resistivity of Ohmic contact areas need to be further improved for high temperature operations. Perhaps the most important factor however is that large scale, high quality, and low cost epitaxial or single crystal SiC films have not yet been fully developed. A technology capable of providing these would greatly improve the availability of SiC high temperature electronic devices. In summary, there exist many limitations for SiC based electronics and their integrate circuits; however, the superior material properties of SiC makes it desirable for extremely high temperature electronics.

References	Material	Device	Max. Temperature (°C)
IMB-CNM, Spain (2012) [32]	4H-SiC	MESFET	300
Raytheon, UK (2011) [29]	4H-SiC	MOSFET	350
Semisouth Lab, USA (2009) [39]	4H-SiC	VJFET	450
JPL, USA (2010) [40]	AlGaN/GaN	MOS HEMT	450
Tokyo Insitute of Technology, Japan (2013) [41]	Diamond	JFET	450
KTH, Sweden (2013) [33]	4H-SiC	BJT	500
NASA, USA [35]	6H-SiC	JFET	500
University of Ulm, Germany (2012) [42]	InAlN/GaN	HEMT	1000

Table 1.4: A sampling of published single transistors for high temperature applications.

1.5 High Temperature Effects in 4H-SiC

To successfully design the high temperature 4H-SiC sensors and electronics, it is crucial to understand the temperature effect of the fundamental semiconductor physical properties.

The energy bandgap (E_G) in 4H-SiC as a function of temperature is approximated by [43]

$$E_G = 3.265 - 6.5 \times 10^{-4}\left(\frac{T^2}{T+1300}\right) \tag{1.2}$$

where T is temperature. The calculated bandgap of Si, 6H-SiC, and 4H-SiC are plotted in Figure 1.4. 4H-SiC has the highest bandgap through the entire temperature range. As temperature increases, the bandgap is reduced, resulting in larger intrinsic carrier concentrations, larger leakage current in pn junctions and poorer device isolation by reversed-biased junctions [38].

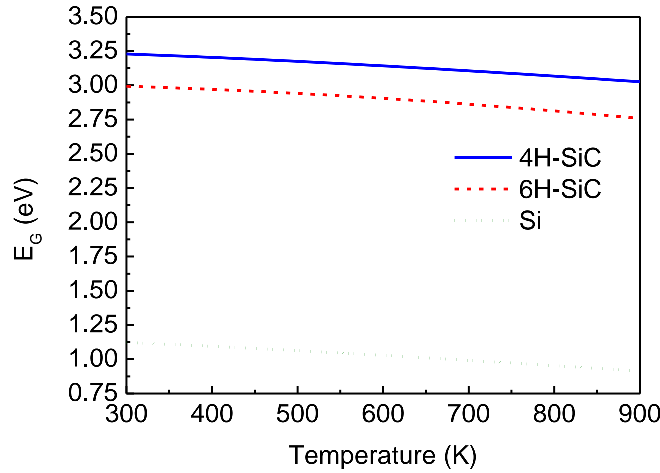

Figure 1.4: Calculated energy bandgap of Si, 6H-SiC, and 4H-SiC versus temperature.

The intrinsic carrier concentration (n_i) in 4H-SiC is given by [44]

$$n_i = \sqrt{N_c N_v}\exp\left(-\frac{E_G}{2k_B T}\right) \tag{1.3}$$

$$N_c = 2M_c\left(\frac{2\pi m_n^* k_B T}{h^2}\right)^{3/2} \tag{1.4}$$

$$N_v = 2\left(\frac{2\pi m_p^* k_B T}{h^2}\right)^{3/2} \tag{1.5}$$

where N_c and N_v are effective density-of-states of electrons in the conduction band and holes in the valence band, respectively. k_B is Boltzmann constant, h is Planck's constant, M_c represent the number of equivalent energy minima in the conduction band and is 3 for

4H-SiC, m_n^* and m_p^* are the electron effective mass and hole effective mass, respectively. Figure 1.5 compares the intrinsic carrier concentration of Si, 6H-SiC, and 4H-SiC versus temperature. For a given temperature, 4H-SiC has the smallest n_i due to the largest bandgap energy. The intrinsic carrier concentration of Si at 900 K is 4.3×10^{17} cm^{-3} which is comparable with the dopant carrier concentrations. Even at 900 K, n_i of 6H-SiC and 4H-SiC are only 4.32×10^{12} and 3.24×10^{11} cm^{-3}, respectively, suggesting a fundamental advantage of wide bandgap SiC over Si for high temperature application.

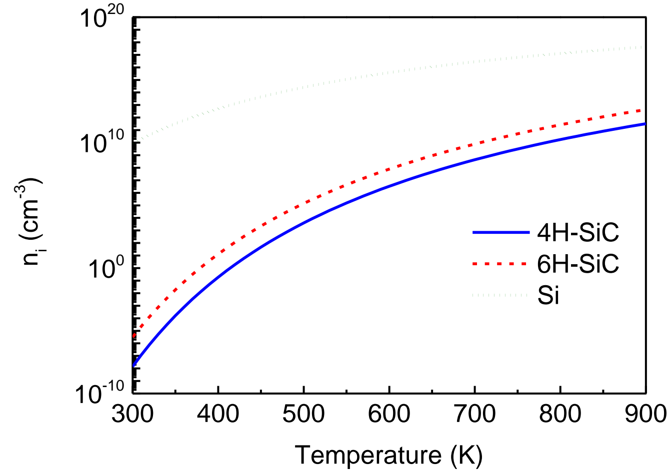

Figure 1.5: Intrinsic carrier concentration in Si, 6H-SiC, and 4H-SiC versus temperature.

There are some fundamental properties, such as carrier mobilities and degree of ionization, will be discussed in the following chapter since they are close related to the JFET transistor parameters.

1.6 Research Objective and Thesis Overview

High-temperature UV sensing chip is beneficial for combustion monitoring and space exploration [45-47]. This dissertation details the two building blocks of high-temperature UV sensing chip, namely UV sensor and transistors.

Chapter 2 investigates the SiC metal-semiconductor-metal (MSM) UV photodetectors (PDs) for high temperature operation. The physics of MSM PDs is first described, then fabrication process. The photo-to-dark current and responsivity of PD are evaluated from room temperature to 450 ℃. Finally, the scheme of antireflection layer to boost the PD responsivity is discussed.

In Chapter 3, the study of 4H-SiC n–channel JFET with raised gate configuration is presented. The physics of JFET is discussed and the integration fabrication process of MSM PDs and JFET is described. Metallization scheme for p- and n-type SiC is presented. The basic properties of JFET from 25 to 600 ℃ is characterized and summarized. TCAD simulation is compared with the measured data, and the possible

reasons for different threshold voltage and leakage current are proposed. Finally, a SPICE DC model level 1 is build for the future circuit simulation.

Chapter 4 presents the design of complementary JFET with buried gate configuration. TCAD simulation is used to design the parameters of device structures. One metal stacks forming Ohmic contact with both n- and p- type 4H-SiC at high temperature is described. Current-voltage characteristics and the extracted device parameters are studied in the temperature range of 25-600 ℃.

Finally, in Chapter 5 the contributions of this work are summarized and future research directions are suggested.

1.7 References

[1] L. L. N. Laboratory. *Energy flow*. Available: https://flowcharts.llnl.gov/

[2] X. Gong, L. An, and C. Xu, "Wireless passive sensor development for harsh environment applications," in *IEEE International Workshop on Antenna Technology (iWAT) 2012*, 2012, pp. 140-143.

[3] P. G. Neudeck, R. S. Okojie, and L.-Y. Chen, "High-temperature electronics-a role for wide bandgap semiconductors?," *Proceedings of the IEEE,* vol. 90, pp. 1065-1076, 2002.

[4] N. A. Riza, M. Sheikh, and F. Perez, "Hybrid wireless-wired optical sensor for extreme temperature measurement in next generation energy efficient gas turbines," *Journal of Engineering for Gas Turbines & Power,* vol. 132, p. 051601, 2010.

[5] D. G. Senesky, B. Jamshidi, K. B. Cheng, and A. P. Pisano, "Harsh environment silicon carbide sensors for health and performance monitoring of aerospace systems: A review," *IEEE Sensors Journal,* vol. 9, pp. 1472-1478, 2009.

[6] M. Mehregany, "Advances in silicon carbide micro-and nano-electro-mechanical systems fabrication technology and applications," in *2013 Transducers & Eurosensors XXVII: The 17th International Conference on Solid-State Sensors, Actuators and Microsystems (TRANSDUCERS & EUROSENSORS XXVII) ,* 2013, pp. 2397-2402.

[7] F. Udrea, S. Ali, M. Brezeanu, V. Dumitru, O. Buiu, I. Poenaru, M. Chowdhury, A. De Luca, and J. Gardner, "SOI sensing technologies for harsh environment," in *2012 International Semiconductor Conference (CAS),* 2012, pp. 3-10.

[8] J. Casady and R. W. Johnson, "Status of silicon carbide (SiC) as a wide-bandgap semiconductor for high-temperature applications: A review," *Solid-State Electronics,* vol. 39, pp. 1409-1422, 1996.

[9] M. R. Werner and W. R. Fahrner, "Review on materials, microsensors, systems and devices for high-temperature and harsh-environment applications," *IEEE Transactions on Industrial Electronics,* vol. 48, pp. 249-257, 2001.

[10] C. S. Roper, "Silicon Carbide Thin Films via Low Pressure Chemical Vapor Deposition for MEMS," Ph. D., Chemical Engineering, University of California at Berkeley, 2007.

[11] C.-M. Zetterling, *Process technology for silicon carbide devices*: IET, 2002.

[12] V. Cimalla, J. Pezoldt, and O. Ambacher, "Group III nitride and SiC based MEMS and NEMS: materials properties, technology and applications," *Journal of Physics D: Applied Physics,* vol. 40, p. 6386, 2007.

[13] E. Monroy, F. Omnes, and F. Calle, "Wide-bandgap semiconductor ultraviolet photodetectors," *Semiconductor Science and Technology,* vol. 18, pp. R33-R51, Apr 2003.

[14] M. Mehregany, C. Zorman, S. Roy, A. Fleischman, C.-H. Wu, and N. Rajan, "Silicon carbide for microelectromechanical systems," *International materials reviews,* vol. 45, pp. 85-108, 2000.

[15] A. R. Atwell, R. S. Okojie, K. T. Kornegay, S. L. Roberson, and A. Beliveau, "Simulation, fabrication and testing of bulk micromachined 6H-SiC high-*g* piezoresistive accelerometers," *Sensors and Actuators A: Physical,* vol. 104, pp. 11-18, 2003.

[16] P. Godignon, "SiC materials and technologies for sensors development," in *Materials Science Forum*, 2005, pp. 1009-1014.

[17] S. A. Bhave, D. Gao, R. Maboudian, and R. T. Howe, "Fully-differential poly-SiC Lame mode resonator and checkerboard filter," in *18th IEEE International Conference on Micro Electro Mechanical Systems (MEMS 2005),* 2005, pp. 223-226.

[18] W.-C. Lien, "Porous and Epitaxial 3C-SiC Thin Films Technology for Micro-electromechanical Systems and Electronics Applications," University of California, Berkeley, 2008.

[19] N. Wright and A. Horsfall, "SiC sensors: a review," *Journal of Physics D: Applied Physics,* vol. 40, p. 6345, 2007.

[20] J. Edmond, H. Kong, A. Suvorov, D. Waltz, and C. Carter Jr, "6H-Silicon Carbide Light Emitting Diodes and UV Photodiodes," *Physica Status Solidi A,* vol. 162, pp. 481-491, 1997.

[21] D. M. Brown, E. T. Downey, M. Ghezzo, J. W. Kretchmer, R. J. Saia, Y. S. Liu, J. A. Edmond, G. Gati, J. M. Pimbley, and W. E. Schneider, "Silicon carbide UV photodiodes," *IEEE Transactions on Electron Devices,* vol. 40, pp. 325-333, 1993.

[22] W. C. Lien, D. S. Tsai, S. H. Chiu, D. G. Senesky, R. Maboudian, A. P. Pisano, and J. H. He, "Low-Temperature, Ion Beam-Assisted SiC Thin Films With Antireflective ZnO Nanorod Arrays for High-Temperature Photodetection," *IEEE Electron Device Letters,* vol. 32, pp. 1564-1566, Nov 2011.

[23] G. Hunter, R. Okojie, P. Neudeck, G. Beheim, G. Ponchak, G. Fralick, J. Wrbanek, and L. Chen, "High temperature electronics, communications, and supporting technologies for Venus missions," in *Proceedings of the Fourth Annual International Planetary Probe Workshop, June*, 2006, pp. 27-30.

[24] L. Chen and M. Mehregany, "A silicon carbide capacitive pressure sensor for in-cylinder pressure measurement," *Sensors and Actuators A: Physical,* vol. 145, pp. 2-8, 2008.

[25] R. S. Okojie, G. M. Beheim, G. J. Saad, and E. Savrun, "Characteristics of Hermetic 6H-SiC Pressure Sensor at 600 C," in *AIAA Space 2001 Conference and Exposition, AIAA Paper*, 2001, pp. 28-30.

[26] J. Du and C. A. Zorman, "A polycrystalline SiC-on-Si architecture for capacitive pressure sensing applications beyond 400° C: Process development and device performance," *Journal of Materials Research,* vol. 1, pp. 1-9, 2013.
[27] D. Brown, E. Downey, M. Ghezzo, J. Kretchmer, V. Krishnamurthy, W. Hennessy, and G. Michon, "Silicon carbide MOSFET integrated circuit technology," *Physica Status Solidi A,* vol. 162, pp. 459-479, 1997.
[28] S. Ryu, K. Kornegay, J. Cooper Jr, and M. Melloch, "Monolithic CMOS digital integrated circuits in 6H-SiC using an implanted p-well process," *IEEE Electron Device Letters,* vol. 18, pp. 194-196, 1997.
[29] D. Clark, E. P. Ramsay, A. Murphy, D. A. Smith, R. Thompson, R. Young, J. D. Cormack, C. Zhu, S. Finney, and J. Fletcher, "High temperature silicon carbide CMOS integrated circuits," in *Materials Science Forum*, 2011, pp. 726-729.
[30] M. Tomana, R. W. Johnson, R. C. Jaeger, and W. C. Dillard, "A hybrid silicon carbide differential amplifier for 350° C operation," *IEEE Transactions on Components, Hybrids, and Manufacturing Technology,* vol. 16, pp. 536-542, 1993.
[31] Z. D. Schwartz and G. E. Ponchak, "High temperature performance of a SiC MESFET based oscillator," in *2005 IEEE MTT-S International Microwave Symposium Digest,* 2005.
[32] M. Alexandru, V. Banu, M. Vellvehi, P. Godignon, and J. Millán, "Design of Digital Electronics for High Temperature using Basic Logic Gates made of 4H-SiC MESFETs," in *Materials Science Forum*, 2012, pp. 104-108.
[33] B. G. M. L. Lanni, C.-M. Zetterling, M. Ostling, "A 4H-SiC bipolar technology for high-temperature integrated circuits " in *IMAPS Conference & Exhibition on High Temperautre Network (HiTEN 2013)*, 2013.
[34] S. Zappe, M. Leone, F. Yang, and E. Obermeier, "Characterisation of silicon carbide JFETs with respect to microsystems for high temperature applications," *Microsystem Technologies,* vol. 3, pp. 134-138, 1997.
[35] P. G. Neudeck, D. J. Spry, L.-Y. Chen, G. M. Beheim, R. S. Okojie, C. W. Chang, R. D. Meredith, T. L. Ferrier, L. J. Evans, and M. J. Krasowski, "Stable Electrical Operation of 6H–SiC JFETs and ICs for Thousands of Hours at 500," *IEEE Electron Device Letters,* vol. 29, pp. 456-459, 2008.
[36] P. G. Neudeck, G. M. Beheim, and C. S. Salupo, "600 C Logic Gates Using Silicon Carbide JFET's," in *2000 Government Microcircuit Applications Conference,* 2000, pp. 20-23.
[37] J. Fraley, M. Schupbach, J. Yang, B. Western, and A. B. Lostetter, "A 450° C High Voltage Gain AC Coupled Differential Amplifier," in *Materials Science Forum*, 2012, pp. 1253-1256.
[38] A. C. Patil, "Silicon Carbide JFET Integrated Circuit Technology For High-Temoerature Sensors," Electrical Engineering and Computer Science, Case Western Reserve University, 2009.
[39] I. Sankin, V. Bondarenko, D. C. Sheridan, M. S. Mazzola, J. B. Casady, J. Fraley, and M. Schupbach, "SiC Lateral Trench JFET for Harsh-Environment Wireless Systems," in *Materials Science Forum*, 2009, pp. 1087-1090.
[40] K.-A. Son, A. Liao, G. Lung, M. Gallegos, T. Hatake, R. D. Harris, L. Z. Scheick, and W. D. Smythe, "GaN-based high-temperature and radiation-hard electronics

for harsh environments," in *SPIE Defense, Security, and Sensing*, 2010, pp. 76790U-76790U-8.

[41] T. Iwasaki, Y. Hoshino, K. Tsuzuki, H. Kato, T. Makino, M. Ogura, D. Takeuchi, H. Okushi, S. Yamasaki, and M. Hatano, "High-Temperature Operation of Diamond Junction Field-Effect Transistors With Lateral pn Junctions," *IEEE Electron Device Letters,* vol. 34, pp. 1175-1177, 2013.

[42] D. Maier, M. Alomari, N. Grandjean, J.-F. Carlin, M.-A. Diforte-Poisson, C. Dua, S. Delage, and E. Kohn, "InAIN/GaN HEMTs for Operation in the 1000° C Regime: A First Experiment," *IEEE Electron Device Letters,* vol. 33, pp. 985-987, 2012.

[43] M. E. Levinshtein, S. L. Rumyantsev, and M. S. Shur, *Properties of Advanced Semiconductor Materials: GaN, AIN, InN, BN, SiC, SiGe*: Wiley, 2001.

[44] T. Ayalew, "SiC Semiconductor Devices Technology, Modeling, and Simulation, " Technical University of Vienna, 2004.

[45] A. A. Kazemi, "Intersatellite laser communication systems for harsh environment of space," in *SPIE Defense, Security, and Sensing*, 2013, pp. 872010-872010-13.

[46] E. Kolawa, "Extreme environments technologies for future space science missions," N. A. S. A., 2007.

[47] D. M. Brown, E. Downey, J. Kretchmer, G. Michon, E. Shu, and D. Schneider, "SiC flame sensors for gas turbine control systems," *Solid-State Electronics,* vol. 42, pp. 755-760, 1998.

Chapter 2

Silicon Carbide Metal-Semiconductor-Metal Ultraviolet Photodetectors

2.1 Introduction

Photodetectors (PDs), especially for ultraviolet (UV) detection, have drawn interest for use in chemical and biological analysis, combustion flame monitoring, and optical communication devices [1-3]. Over the past few years, different types of PDs have been developed including photoconductor, Schottky barrier photodiodes, p-n and p-i-n photodiodes, avalanche photodiode, phototransistor, metal-insulator-semiconductor structures, and metal-semiconductor-metal (MSM) photodiodes [2, 4].

Most operation environments under UV radiation require the PDs to work at elevated temperatures [2]. However, conventional Si-based PDs, with a narrow bandgap of 1.12 eV, are limited to low operation temperatures (below 125 ℃) due to the generation of thermal carriers, significant shifts in the optical properties, and device aging under UV radiation, leading to the severe deterioration in photosensitivity and spectral response [3]. For example, the Si photodiodes exhibit a high dark current density of 0.01 and 10 A/cm^2 at 300 and 500 ℃, respectively [5]. Wide-bandgap materials, such as AlN and SiC are potential candidates for the UV photodetection at a high temperature. However, several obstacles need to be overcome before employing wide bandgap semiconductors as UV photodetectors. The first limitation is that the high dopant activation energy is required for these materials making the heavily doped layers with different type of dopants difficult to achieve [6]. The second limitation, which comes with the consequence of the first limitation, is that the lack of reliable Ohmic metal contact to wide bandgap semiconductor at a high temperature [2, 6]. These drawbacks hinder the development of p-n, p-i-n photodiodes and phototransistor by using the wide bandgap materials. On the other hand, MSM PDs based on the two back-to-back Schottky contacts do not require the Ohmic contact, which is beneficial for wide bandgap semiconductors. Furthermore, compared to p-i-n diodes or Schottky barrier photodiodes, MSM PDs offer high operation speed and low capacitance operation, and can be readily integrated with field effect transistors in a single chip without complex fabrication steps [4, 7, 8]. Therefore, MSM PDs using wide bandgap materials is suitable for the development of UV detectors at a high temperature.

Among the variety of wide bandgap materials, 4H-SiC has high thermal conductivity (~4.9 W/cm K, three times larger than Si), strong chemical bond, high electron saturation velocity (2×10^{-7} cm/s, two times larger than Si) which enables 4H-SiC PDs to operate at high temperature, high power and high radiation environments with high operation speed [6]. In this chapter, we demonstrate a 4H-SiC MSM PD with working temperatures as high as 450 ℃. The responsivity under the 325-nm illumination is 0.305 A/W at 20 V bias. 4H-SiC MSM PDs exhibit a fast photoresponse even at 400 ℃ with rise time and fall time as low as 684 and 786 μs, respectively, demonstrating excellent temperature tolerance and operation speed. This study paves the way for SiC PDs for UV detector applications within extremely harsh conditions.

2.2 Physics of MSM Photodetectors

The first metal-semiconductor-metal (MSM) photodetector is demonstrated by T. Sugeta et al. [4]. The structure consists of planar interdigitated metal-semiconductor contacts as shown in Figure 2.1. This structure can be viewed as two back-to-back Schottky barriers of both n- and p- type semiconductor as shown in Figure 2.2. The interdigitated structures allow PDs collecting more photocurrent when they are fully functional. Light is penetrated into semiconductor layers at the gap between of the metal contacts, the layers should have a thickness at least larger than the absorption length (1/α), where α is optical absorption coefficient.

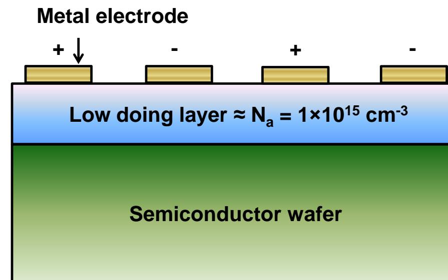

Figure 2.1: Schematic of MSM photodetector.

In typical operation, MSM photodetectors consists of two Schottky barriers, bias of any polarity will make one Schottky barrier in the reverse direction and the other in forward bias. When there is no light shinning on the MSM photodetectors, the dark current saturation is mainly due to thermionic-emission current at low bias as shown in Figure 2.3(a) for p-type semiconductor. The saturation current, considering both electron and hole currents, can be expressed as follows

$$I_{dark} = A_1 A_n^* T^2 \exp\left(\frac{-q\phi_{Bn}}{kT}\right) + A_2 A_p^* T^2 \exp\left(\frac{-q\phi_{Bp}}{kT}\right) \quad (2.1)$$

where A_1 and A_2 are the forward bias and reverse bias contact area, A_n^* and A_p^* are the effective Richardson constants for electron and holes, respectively, φ_{Bn} and φ_{Bp} are the

Schottky barrier height on n-type and p-type semiconductor, respectively, k is Boltzmann constant, and T is absolute temperature. In reality, the current increase with higher bias because of the image-force lowering that modifies the barrier height, and carrier tunneling through the Schottky barrier.

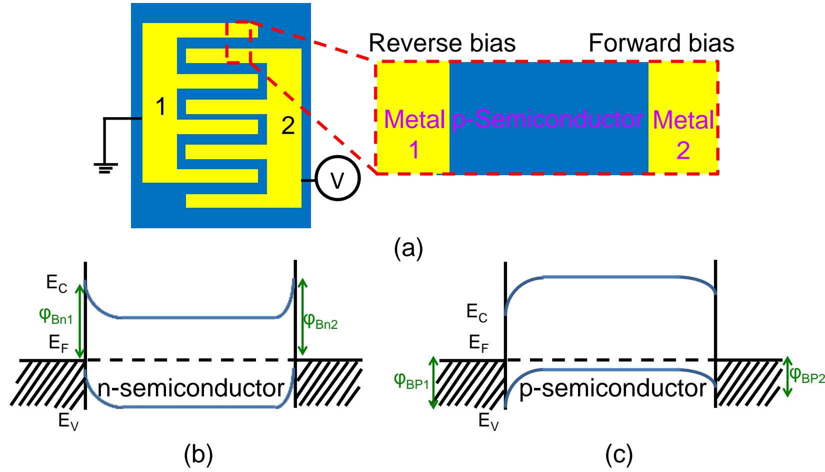

Figure 2.2: (a) The MSM photodetector is considered as two back-to-back Schottky barriers. Energy-band diagrams of MSM PDs at equilibrium (b) with n-type semiconductor layers and (c) with p-type semiconductor layers.

When the photodetectors is shinning with the light, the photocurrent rises at low voltage bias due to the expansion of the depletion region in reverse-biased Schottky junction. The degeneration of photocurrent is via band-to-band excitation as shown in Figure 2.3(b).

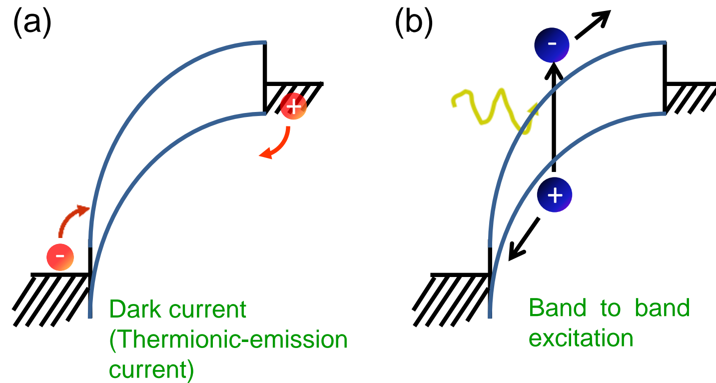

Figure 2.3: Energy-band diagrams of MSM PDs for p-type semiconductor (a) without light and (b) with light at flat-band voltage.

The photocurrent reaches saturation at the flat-band voltage in which the electric field becomes zero at forward-biased junction. The quantum efficiency at this condition can be close to 100%. The flat-band voltage can be estimated by a one-dimensional depletion equation as follows

$$V_{FB} = \left(\frac{qN}{2\varepsilon_s}\right) s^2 \tag{2.2}$$

where N is the doping concentration, ε_s is permittivity of semiconductor and s is the spacing between the interdigitated fingers. The major disadvantage of the MSM photodetectors is high dark current due to the Schottky-barrier junction rather than p-n junction [4]. The MSM photodetectors has two primary advantages: high speed and compatibility with CMOS technology. Conventionally, the response speed of p-n photodiode is limited by drift time in the depletion region, diffusion of carriers, and capacitance of the depletion region. On the other hand, the high speed operation of MSM PDs could be attributed to the low capacitance per area of the PD due to two-dimensional effects on a low doping thin film or semi-insulating substrate [4].

2.3 4H-SiC MSM Photodetectors

2.3.1 Fabrication Process and Characterization Methods

Figure 2.4(a) is a schematic of the 4H-SiC MSM structures used in this work. The PDs were fabricated on p-type 3-inch research-grade 4H-SiC wafers (sheet resistivity < 2.5 Ω-cm, from Cree Inc.) with a 7-um-thick lightly p-type Al-doped epitaxial layer with a carrier concentration of 2×10^{15} cm^{-3}. A 100-nm-thick SiO_2 passivation layer was deposited on substrate using plasma enhanced chemical vapor deposition. As shown in Figure 2.4(b), the planar MSM PDs were defined using photolithography, e-beam evaporation and metal lift-off process with active areas of 500 µm ×158 µm and utilized 8-µm-wide, 150-µm-long interdigitated 20 nm Cr/150 nm Pd electrodes, which have high melting point, with 8-µm-wide spacing on the 4H-SiC substrates. This 4H-SiC MSM PD could be fabricated with 4H-SiC JFET in the same process. Detail fabrication process will be discussed in Chapter 3.

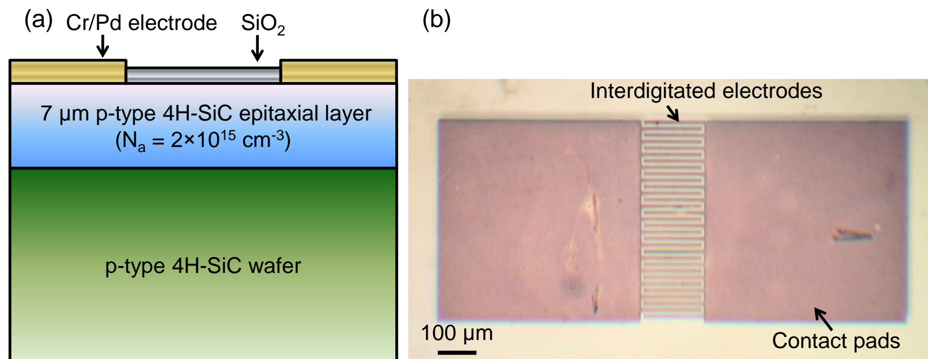

Figure 2.4: (a) Schematic and (b) optical image of 4H-SiC MSM PDs.

The crystal structure of the films was monitored with transmission electron microscopy, TEM (JEOL JEM-2100F, operating at 200 kV). The transmission spectra were measured with a JASCO V-670 UV-visible spectrometer in the spectral range from 250 nm to 800 nm. Photocurrent was generated under the illumination of a He–Cd laser at a wavelength of 325 nm with laser power density of 1.02×10^4 W/m^2. The Keithley 4200-SCS semiconductor characterization system with Tungsten probe tips were used to measure I-V characteristics of the fabricated PDs. The time-resolved measurements were measured by the ADLINK DAQ-2214-005 data acquisition system with Stanford Research System SR570 low noise current preamplifier and assisted by a mechanical chopper to switch on/off the UV light as shown in Figure 2.5. For high-temperature characterization, the PDs are heated on hot plate and the device temperature was monitored with calibrated thermocouple.

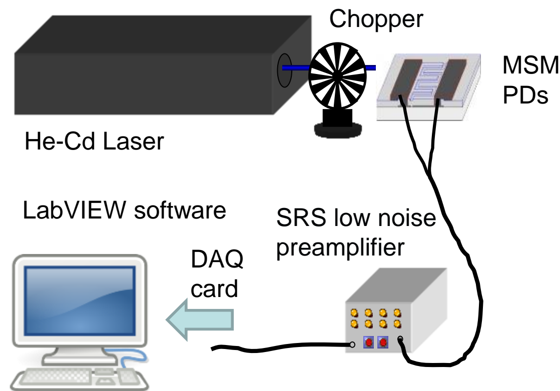

Figure 2.5: Schematic of time-resolved measurement system.

2.3.2 Characterization of 4H-SiC Thin Films

The cross-sectional transmission electron microscopy (TEM) image of a 7-um-thick, lightly Al doped epitaxial 4H-SiC films and its corresponding electron diffraction pattern are shown in Figure 2.6. There is no obvious structural defect such as micropipes observed in the epitaxial thin films. The results suggest that the lightly doped p-type epitaxial 4H-SiC thin films have hexagonal structure and exhibit the superior crystallinity.

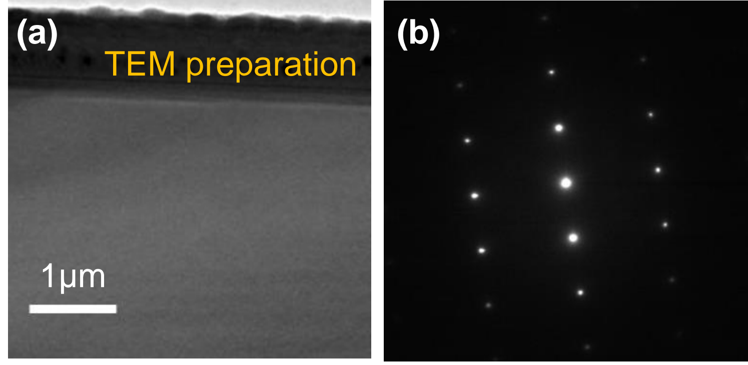

Figure 2.6: (a) Cross-sectional TEM image and (b) electron diffraction pattern of epitaxial p-type 4H-SiC layer.

The transmission spectrum of 4H-SiC substrates is shown in Figure 2.7. The 4H-SiC substrate shows nearly no absorption in visible/IR regions, implying that the as-fabricated 4H-SiC MSM PDs have intrinsic visible-blindness. Based on the Tauc relation [9], by extrapolating the linear region (red line in Figure 2.7(b)) of the $(\alpha h\upsilon)^2$ versus incident energy ($h\upsilon$) plot as shown in Figure 2.7, where α is optical absorption coefficient, h is Planck's constant, and υ is photon frequency, the optical bandgap of 4H-SiC substrates is approximately 3.23 eV.

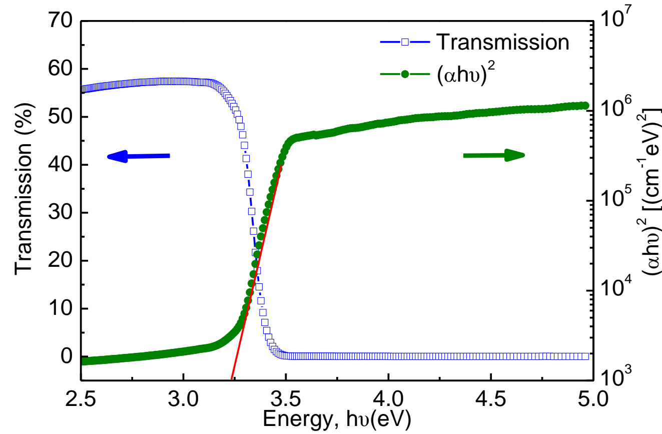

Figure 2.7: The transmission spectrum (left y axis) and $(\alpha h\upsilon)^2$ (right y axis) vs. $h\upsilon$ plot of 4H-SiC substrates.

2.3.3 Characterization of 4H-SiC MSM Photodetector

The I-V curves of the SiC MSM PD in the dark and under 325-nm He-Cd laser illumination at room temperature are shown in Figure 2.8. The dark current of the 4H-SiC MSM PD is approximately 6×10^{-11} A at 5 V bias which corresponds to a leakage current density of 1.5×10^{-7} A/cm^2. The photocurrent of PDs is approximately five orders of magnitude larger than the dark current at 5 V bias. The responsivity (R_i) of PDs can be obtained as follows [4]

$$R_i = \frac{I_{photo}}{P_{opt}} \tag{2.3}$$

where I_{photo} is the net photocurrent and the P_{opt} is the optical incident power, which is 4×10^{-4} W in our case. The calculated responsivities under the 325-nm illumination are 0.0167 A/W and 0.0305 A/W at 5 V and 20 V bias, respectively. The sensitivity factor, photo-to-dark current ratio (PDCR), which is defined as follows [9]

$$PDCR = \frac{(I_p - I_d)}{I_d} \tag{2.4}$$

where I_d is the dark current and I_p is the photocurrent under illumination. Figure 2.9 shows the time-resolved measurements at a fixed bias of 5 V and at room temperature. The calculated PDCR value is 1.28×10^5 at 25 ℃. The temperature-dependent response of PDCR and responsivity shown in Figure 2.10 indicates that the 4H-SiC MSM PDs are capable of significant UV light sensing up to 450 ℃ due to the low levels of dark currents and the high thermal stability of the 4H-SiC films at high temperatures. A further increase in temperature lowers the sensitivity factor of SiC PDs due to an increase in dark current at a high temperature by generating the thermal carriers which cannot be completely eliminated [9]. However, the responsivity increases as temperature increases till 400 ℃ under a 5 V bias. This might be because the energy bandgap of 4H-SiC decreases at higher temperature with the rate of 6.5×10^{-4} eV/K and thus boost the photocurrent at high temperatures. Since the definition of responsivity is only counting the photocurrent by subtracting the photocurrent by dark current, the PDCR value, further divide by the dark current, is more suitable to express and understand the temperature effect of the PDs.

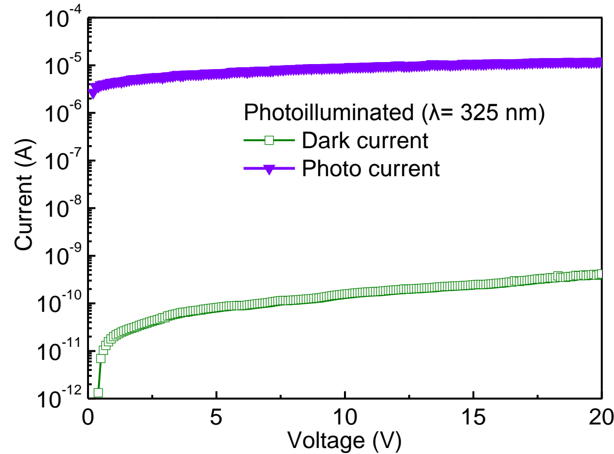

Figure 2.8: I-V curves of the 4H-SiC MSM PDs measured in the dark and under 325-nm illumination at room temperature.

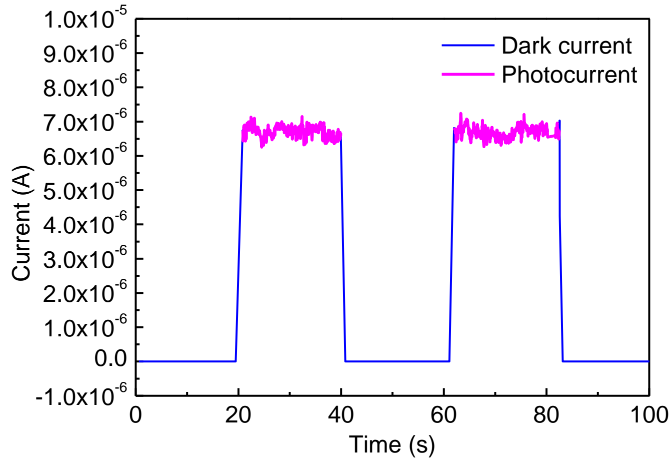

Figure 2.9: The time dependence of the photocurrent and dark current of SiC MSM PDs at 25 ℃ under a 5 V bias.

To highlight the ultrafast photoresponse characteristics of the SiC PDs even at high temperature, the time-resolved measurements were performed at a fixed bias of 5 V and 450 ℃. As shown in Figure 2.11, the current abruptly increased and then decreased to its initial value as the light was on and off, respectively; a fully reversible response was obtained in spite of the small PDCR value of 0.62. The shifting of the dark current at 450 ℃ is probably due to the thermal agitation of probe tips which is absence in the room temperature measurement as shown in Figure 2.9. Note that the contributions of the measured dark current are not only from the thermal carriers of MSM PDs but also from the thermal noise of the probe tips used in the characterization set up. Suitable high-temperature ceramic packages [10] or a high-temperature probe station can reduce the amount of the thermal noise generated from the probe-testing and thus boost the operating temperature for 4H-SiC MSM PDs. The set up information of the high-temperature probe station could be found in chapter 3.

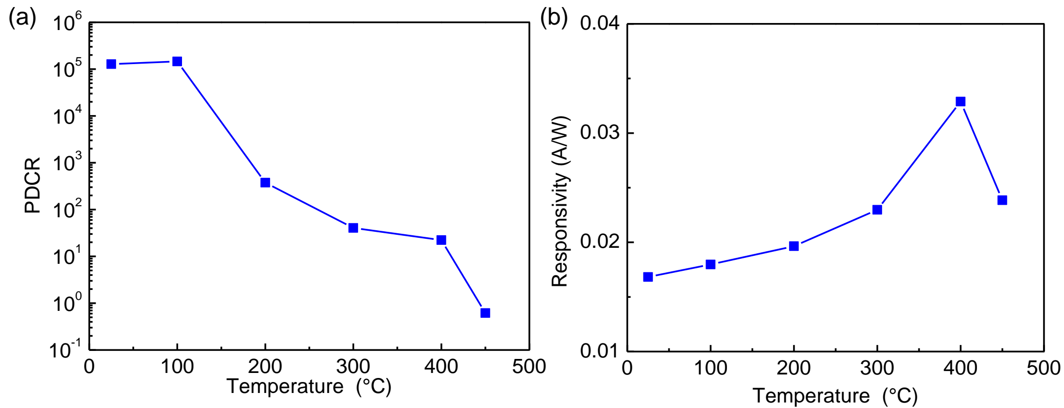

Figure 2.10: (a) PDCR value and (b) responsivity as function of temperature under a 5 V bias.

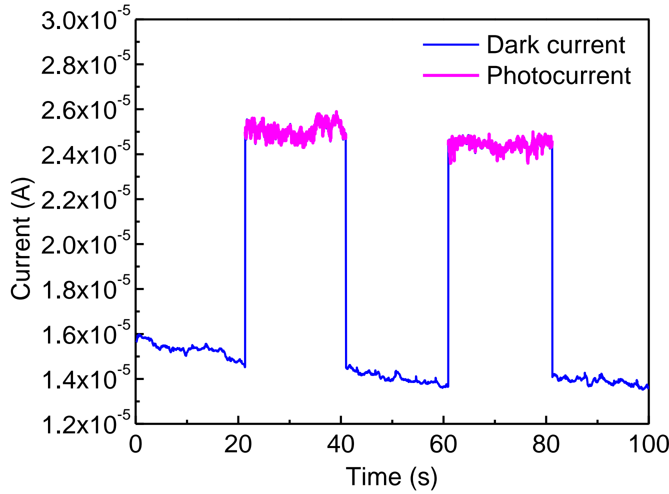

Figure 2.11: The time dependence of the photocurrent and dark current of SiC MSM PDs at 450 °C under a 5 V bias.

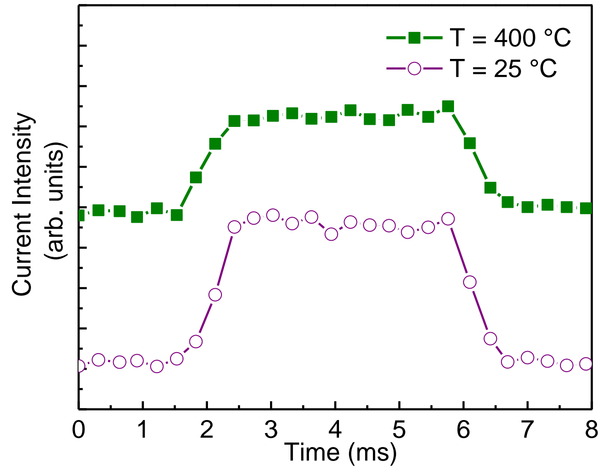

Figure 2.12: The transient photocurrent of SiC MSM PDs at room temperature and 400 °C under a 5 V bias.

Figure 2.12 shows the transient photocurrent of 4H-SiC MSM PDs at room temperature and 400 °C. The operation speed of the MSM PDs can be determined by performing the time-resolved measurement. Note that the PDCR value of time-resolved measurement is different from the values presented in Figure 2.10. The PDCR value of the fabricated PDs shown in figure 2.10 was measured by Keithley 4200-SCS semiconductor characterization system which has the resolution of ~ 10^{-15} A. However, the time resolution in our Keithley 4200-SCS system is only ~ 150 mS which is too big for 4H-SiC PDs. The time-resolved measurements were then measured by custom-made data acquisition system with Stanford Research System SR570 low noise current preamplifier and assisted by a mechanical chopper to switch on/off the UV light. This system has the time resolution of ~ 10 μS. Due to the unperfected ground of the

connecting cables, the current resolution of this custom-made system is only ~ 10^{-7} A which makes the PDCR values are different than the one measured by Keithley system. Therefore, the y axis in the time-resolved measurement (Fig. 4(b)) is labeled as arbitrary units. The quantitative parameters of describing how fast the photodetector responds to external light illumination are rise time and fall time. The rise time is the time required reaching the steady-state photocurrent and is defined as the time difference between 10% and 90% of photocurrent. Fall time means the time required for the decay when the optical excitation is interrupted and is the time difference between 90% and 10% of photocurrent [11]. Extracted rise time and fall time are summarized and listed on Table 1. Rise time and fall time of PD at room temperature are 594 and 699 μs, respectively. As temperature increases to 400 ℃, the rise time and the fall time are increased to 684 and 786 μs, respectively, indicating that temperature-tolerant photoresponse of SiC MSM PDs. Due to the unperfected ground problem of time-resolved measurement system, the rise and fall time of 4H-SiC MSM PDs are slightly underestimated. The reason for the decrease in the operation speed of PDs with temperature is stated as follows. The transit-time-limited bandwidth is proportional to the saturation velocity at fixed spacing between fingers [12]

$$f_{tr} = \frac{0.441}{\sqrt{2}}\left(\frac{v_s}{s}\right) \tag{2.5}$$

where f_{tr} is the transit-time-limited 3-dB bandwidth, v_s is the saturation velocity, and s is the spacing between electrode fingers. The hole/electron saturation velocity of 4H-SiC is decreased as temperature increases [13], leading to the decrease in the bandwidth and thus the speed of the PD at a high temperature.

Temperature (℃)	Rise Time (μs)	Fall Time (μs)
25	594	699
400	684	786

Table 2.1: Response time of fabricated 4H-SiC MSM photodetectors.

2.4 Antireflection Layer Using Nanostructure

The responsivity of 0.0305 A/W at 20 V and under 325-nm illumination is comparable with the commercial SiC UV detector chip fabricated by Cree Inc. (~0.056 A/W) at room temperature [2]. For high temperature characterization, there are several works reporting the PDCR value of approximately 2, 2.5, 7.5 by using amorphous SiCN [14], SiCBN [3], nanocrystalline SiC [9] at 200 °C, respectively. The PDCR value of 375 at 200 °C of this work is superior to the previous works. In order to further boost the responsivity and PDCR value of 4H-SiC MSM PDs, antireflection coating can be added on PDs by reducing the surface reflection and allowing more light to reach the active region. A conventional single layer antireflection coating (ARC) works only in a limited

spectral range for a specific angle of incidence (AOI), typically for a near normal incidence. Recently, it was reported that nanostructures exhibit superior broadband, omnidirectional AR characteristics [15-19]. Despite the numerous investigations on optical characterizations of AR nanostructures, more practical applications are required to demonstrate their feasibility. Recently ZnO nanostructures also demonstrated exciting possibilities for next-generation ARCs to suppress the Fresnel reflection effectively as shown in Figure 2.13 [9]. Detail synthesis process of ZnO nanostructures could be found in Ref. 10. For example, the reflection spectra of bare nanocrystalline SiC MSM PDs without any ARC are shown in Figure 2.14 (a). The dip of reflection at 455 nm corresponds to the bandgap absorption of amorphous SiC. Figure 2.14 (b) confirms that the use of ZnO NRAs as an AR layer significantly reduces the reflection over a wide range of wavelengths. The reflectance of MSM PD with ZnO NRAs is decreased to below 2% in the UV region and 20% in the visible/NIR regions over a wide range of AOIs. The dip of reflection at 380 nm corresponds to the bandgap absorption of ZnO NRAs.

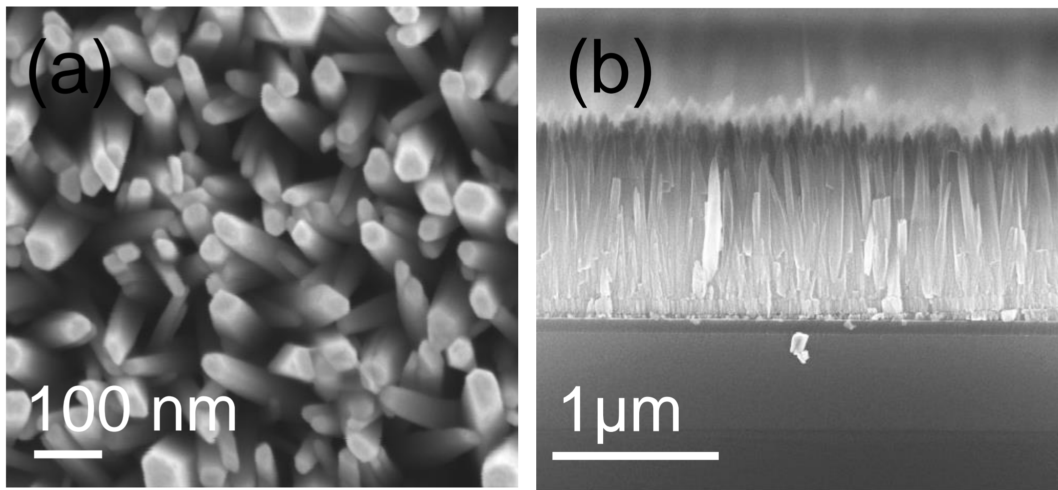

Figure 2.13: (a) Top view and (b) cross-sectional SEM image of ZnO NRA/SiC layers [9].

To gain insight into light coupling into the SiC PDs, the steady-state distribution of electromagnetic fields was simulated by FDTD analysis based on Maxwell's equations (Figure 2.15), indicating the time-averaged TE-polarized electric field intensity distribution with PDs at 532 nm. The insets in Figure 2.15(a)-2.15(b) reveal that the ZnO NRAs guide propagating light efficiently across the interfaces by reducing the refractive index mismatch between air and SiC, and also widening the field distribution within the PDs by increasing the light scattering on the SiC surface.

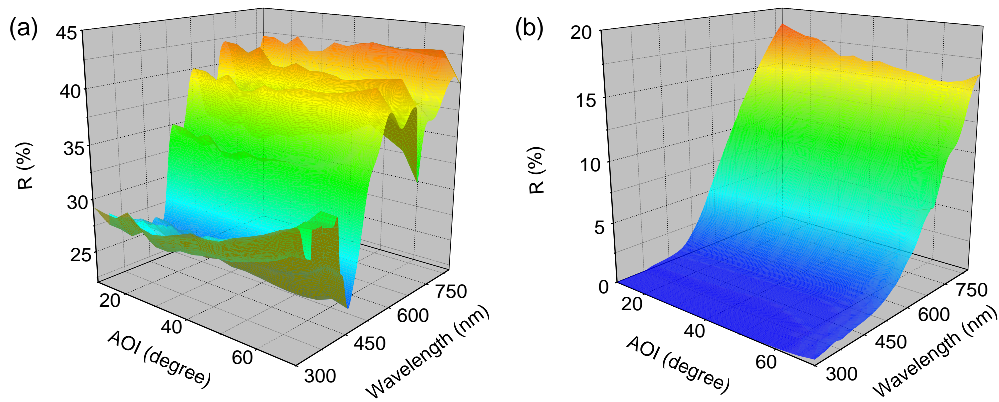

Figure 2.14: Reflectance spectra of (a) bare SiC MSM PDs and (b) ZnO NRA/ SiC MSM PDs with a wide range of AOIs.

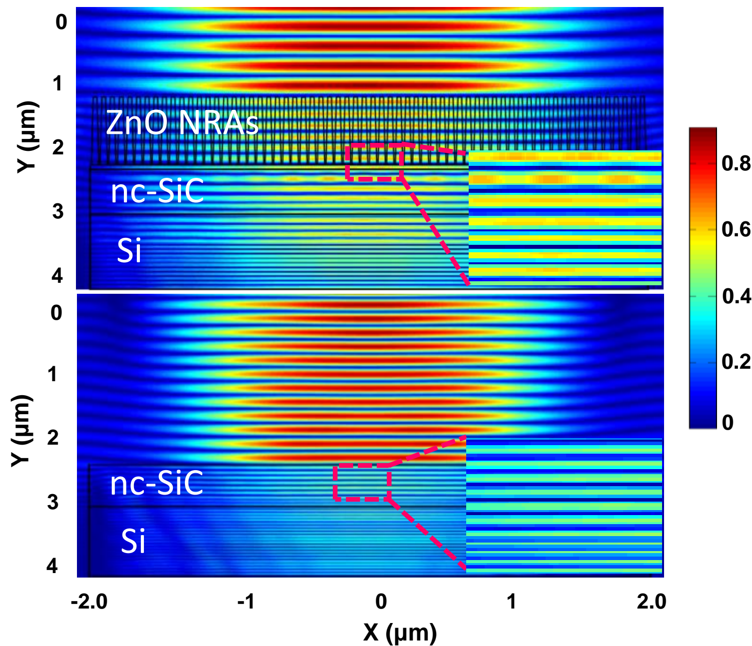

Figure 2.15: FDTD simulation of time-averaged and normalized TE electric field distribution at 532 nm (a) without and (b) with ZnO NRAs. The insets in (a) and (b) are the enlarged images at the top SiC surface.

2.5 Summary

In summary, the MSM PDs employing lightly Al-doped epitaxial 4H-SiC thin films with working temperatures up to 450°C were fabricated. The PDCR value is 1.3×105 at 25°C and decreases to 0.62 at 450°C under a 325-nm illumination. The

responsivity is 0.0305 A/W at 20 V bias under the 325-nm illumination. Moreover, the operation speed of PDs exhibits temperature-tolerant characteristics; as the temperature increased from 25°C and 400°C, the rise time and the fall time of the PD increase from 594 to 684 μs and from 699 to 786 μs, respectively. This work demonstrates that the 4H-SiC holds promise for the next-generation visible-/IR-blind UV PDs for use in extremely harsh environments.

2.6 References

[1] W.-R. Chang, Y.-K. Fang, S.-F. Ting, Y.-S. Tsair, C.-N. Chang, C.-Y. Lin, and S.-F. Chen, "The hetero-epitaxial SiCN/Si MSM photodetector for high-temperature deep-UV detecting applications," *IEEE Electron Device Letters,,* vol. 24, pp. 565-567, 2003.

[2] E. Monroy, F. Omnes, and F. Calle, "Wide-bandgap semiconductor ultraviolet photodetectors," *Semiconductor Science and Technology,* vol. 18, pp. R33-R51, Apr 2003.

[3] A. Vijayakumar, K. Sundaram, and R. Todi, "Amorphous-SiCBN-based metal–semiconductor–metal photodetector for high-temperature applications," *IEEE Electron Device Letters,* vol. 28, pp. 713-715, 2007.

[4] S. M. Sze and K. K. NG, *Physics of semiconductor devices*: Wiley, 2007.

[5] D. M. Brown, E. T. Downey, M. Ghezzo, J. W. Kretchmer, R. J. Saia, Y. S. Liu, J. A. Edmond, G. Gati, J. M. Pimbley, and W. E. Schneider, "Silicon carbide UV photodiodes," *IEEE Transactions on Electron Devices,* vol. 40, pp. 325-333, 1993.

[6] A. A. Stephen E. Saddow, *Advances in Silicon Carbide Processing and Applications*, 2004.

[7] S. Assefa, F. N. Xia, S. W. Bedell, Y. Zhang, T. Topuria, P. M. Rice, and Y. A. Vlasov, "CMOS-integrated high-speed MSM germanium waveguide photodetector," *Optics Express,* vol. 18, pp. 4986-4999, Mar.

[8] D.-S. Tsai, C.-A. Lin, W.-C. Lien, H.-C. Chang, Y.-L. Wang, and J.-H. He, "Ultra-High-Responsivity Broadband Detection of Si Metal–Semiconductor–Metal Schottky Photodetectors Improved by ZnO Nanorod Arrays," *ACS nano,* vol. 5, pp. 7748-7753, 2011.

[9] W. C. Lien, D. S. Tsai, S. H. Chiu, D. G. Senesky, R. Maboudian, A. P. Pisano, and J. H. He, "Low-Temperature, Ion Beam-Assisted SiC Thin Films With Antireflective ZnO Nanorod Arrays for High-Temperature Photodetection," *IEEE Electron Device Letters,* vol. 32, pp. 1564-1566, Nov 2011.

[10] P. G. Neudeck, S. L. Garverick, D. J. Spry, L. Y. Chen, G. M. Beheim, M. J. Krasowski, and M. Mehregany, "Extreme temperature 6H-SiC JFET integrated circuit technology," *Physica Status Solidi A-Applications and Materials Science,* vol. 206, pp. 2329-2345, Oct 2009.

[11] K. Wang, F. Chen, N. Allec, and K. S. Karim, "Fast Lateral Amorphous-Selenium Metal-Semiconductor-Metal Photodetector With High Blue-to-Ultraviolet

Responsivity," *IEEE Transactions on Electron Devices,* vol. 57, pp. 1953-1958, Aug.

[12] J. Kim, W. B. Johnson, S. Kanakaraju, L. C. Calhoun, and C. H. Lee, "Improvement of dark current using InP/InGaAsP transition layer in large-area InGaAs MSM photodetectors," *IEEE Transactions on Electron Devices,* vol. 51, pp. 351-356, Mar 2004.

[13] S. Potbhare, N. Goldsman, A. Lelis, J. M. McGarrity, F. B. McLean, and D. Habersat, "A physical model of high temperature 4H-SiC MOSFETs," *IEEE Transactions on Electron Devices,* vol. 55, pp. 2029-2040, Aug 2008.

[14] W. R. Chang, Y. K. Fang, S. F. Ting, Y. S. Tsair, C. N. Chang, C. Y. Lin, and S. F. Chen, "The hetero-epitaxial SiCN/Si MSM photodetector for high-temperature deep-UV detecting applications," *IEEE Electron Device Letters,* vol. 24, pp. 565-567, Sep 2003.

[15] J. Huang, X. Wang, and Z. L. Wang, "Bio-inspired fabrication of antireflection nanostructures by replicating fly eyes," *Nanotechnology,* vol. 19, p. 025602, 2008.

[16] Y.-C. Chao, C.-Y. Chen, C.-A. Lin, Y.-A. Dai, and J.-H. He, "Antireflection effect of ZnO nanorod arrays," *Journal of Materials Chemistry,* vol. 20, pp. 8134-8138, 2010.

[17] Y.-A. Dai, H.-C. Chang, K.-Y. Lai, C.-A. Lin, R.-J. Chung, G.-R. Lin, and J.-H. He, "Subwavelength Si nanowire arrays for self-cleaning antireflection coatings," *Journal of Materials Chemistry,* vol. 20, pp. 10924-10930, 2010.

[18] Y.-L. Chueh, Z. Fan, K. Takei, H. Ko, R. Kapadia, A. A. Rathore, N. Miller, K. Yu, M. Wu, and E. Haller, "Black Ge based on crystalline/amorphous core/shell nanoneedle arrays," *Nano letters,* vol. 10, pp. 520-523, 2009.

[19] G. Lin, K. Lai, C. Lin, Y. Lai, and J. He, "Efficiency enhancement of InGaN-based multiple quantum well solar cells employing antireflective ZnO nanorod arrays," *IEEE Electron Device Letters,* vol. 32, pp. 1104-1106, 2011.

Chapter 3

Silicon Carbide N-Channel Raised Gate Junction Field-Effect Transistors

3.1 Introduction

High temperature sensors and electronics that operate at 300-600 ℃ are required for in-situ monitoring of fuel combustion, subsurface reservoirs (deep well drilling), and Venus and Jupiter surface exploration [1-4]. The sensors and electronics capable of high-temperature operation not only minimize the expensive and large cooling systems, but also improve the reliability of the system [5]. Silicon carbide has become the candidate for these harsh environment sensing applications because of its wide bandgap (3.2 eV for 4H-SiC), excellent chemical and thermal stability, and high breakdown electric field strength (5 MV/cm) [4]. Operational amplifiers (Opamps) are the main elements of complex integrated circuits. SiC-based opamps have been investigated based on the MOSFET and JFET device structures [6-8]. While MOSFETs suffer from the low inversion mobility and poor gate oxide reliability, which limit the operating temperature to 400 ℃ [7-9], transistors utilizing SiC pn junctions (JFET and BJT) enable increased operation durations at high temperature [10-12]. BJTs exhibit superior electrical properties, but require higher power consumption and rapidly degraded at temperature above 350 ℃, and more studies on long time stability are needed [13]. Currently, most SiC JFETs for low voltage analog signal amplification utilize 6H-SiC and show long term reliability more than 5000 hours of continuous 500 ℃ electrical operation in air [6]. However, replacing 6H-SiC with 4H-SiC substrates has attracted attention recently, because 4H-SiC has a larger bandgap, higher electron mobility than 6H-SiC (950 cm^2/Vs perpendicular to c-axis and 1150 cm^2/Vs parallel to c-axis) and has commercially available wafers up to 6 inches [14, 15]. In this chapter, we develop the low voltage, normally-on, lateral JFETs using 4H-SiC and characterize their electrical properties from room temperature up to 600 ℃ in air.

3.2 Physics of JFET

The junction field-effect transistor was invented by W. Shockley in 1952 [16]. The gate voltage changes the pn junction depletion width and electric field in the direction normal to the semiconductor surface. It is a unipolar transistor which means only one type of carrier is involved in the operation. Using the pn junction to control the associated electric field and conducting current with majority carriers offers the advantage of using a JFET for high temperature applications, as it eliminates the chance of metal-semiconductor-oxide interface traps, increase oxide reliability, and reduces the minority carrier instability [5].

The fundamental operation principle of n-channel JFET is described as follows [11, 16, 17]. First, the gate terminal is grounded and the drain voltage is 0 V. JFET is in thermal equilibrium. As shown in Figure 3.1 (a), once the p^+-n junction is deposited, the depletion width is formed. Due to the heavily doped p-type gate area, the depletion region primarily extends into the lightly doped n-channel area of the device. The device at this stage is in off state (Figure 3.1 (b)). Applying V_D to small positive voltages, the channel is formed at the non-depleted and current-carrying region as shown in Figure 3.1 (c). The channel acts like a simple resistor, and the drain current is increased linearly with drain voltage as shown in point B of Figure 3.1 (d). As V_D keeps increasing, the depletion width around drain side is widened as shown in Figure 3.1 (e). The channel region is still like a resistor, but because of the loss of the conduction channel near the drain side, the resistance between the source and drain is increased and the increasing rate of I_D is reduced which results the slope of I_D-V_D characteristic decreases at larger V_D as shown in point C of Figure 3.1 (f). If we continue to increase the V_D, the channel is further narrowed and eventually reaches the pinch-off state shown in Figure 3.1 (g). The slope of I_D-V_D characteristic is approximately zero at the pinch-off set, as shown at point D in Figure 3.1 (h), and the drain bias at this point is called saturation drain voltage (V_{Dsat}). As the drain voltage becomes larger than V_{Dsat}, the pinch-off area widens to the extent of ΔL. The voltage difference between V_D and V_{Dsat} is mainly dropped along the ΔL, and the major mechanism of current flow is through drift current as shown in Figure 3.1 (i). The corresponding I_D-V_D characteristic saturates, namely remaining constant at the saturation drain current shown in point E of Figure 3.1 (j).

The drain current (I_{DS}) versus drain-to-source voltage (V_{DS}) characteristics of JFET can be expressed using the conventional 3/2 power model which originally developed for long channel Si JFET [5, 17]. The basic assumptions are uniformly doped channel with gradual-channel approximation (i.e., electric field perpendicular to channel is smaller than electric field parallel to channel), abrupt depletion layer, small gate leakage current and constant mobility. Assuming that the Fermi level on the heavily doped side is positioned at the band edge, the built-in potential (V_{bi}) of p^+-n junction is given by

$$V_{bi} = \frac{1}{q}\left[E_g - kTln\left(\frac{N_D^+}{n_i}\right)\right] \tag{3.1}$$

where q is unit electronic charge, E_g is bandgap of semiconductor, k is Boltzmann constant, T is temperature, N_D^+ is ionized donor impurity concentration, and n_i is intrinsic carrier concentration. The pinch-off potential (V_P) is given by

$$V_P = \frac{qN_D D}{2\varepsilon_s} \tag{3.2}$$

where D is the channel depth and ε_s is permittivity of 4H-SiC. The normalized pinch-off current ($I_P{}'$) is given by

$$I_P' = \left(\frac{q^2 N_D n \mu_n D^3}{6\varepsilon_s}\right) \tag{3.3}$$

where n is ionized carrier concentration in the channel and μ_n is mobility of carriers. The gate threshold voltage (V_T) around which the JFET is turned on and off is given by

$$V_T = V_{bi} - V_P \tag{3.4}$$

In triode region, where $V_{DS} < V_{Dsat} = V_{GS} - V_T$, the drain current is given by

$$I_{DS} = \left(\frac{W}{L}\right) I_P' \left[\frac{3V_{DS}}{V_p} - 2\left[\left\{\frac{V_{DS} - V_{GS} + V_{bi}}{V_p}\right\}^{3/2} - \left\{\frac{(-V_{GS} + V_{bi})}{V_p}\right\}^{3/2}\right]\right](1 + \lambda V_{DS}) \tag{3.5}$$

In saturation region, where $V_{DS} \geq V_{Dsat} = V_{GS} - V_T$,

$$I_{DS} = \left(\frac{W}{L}\right) I_P' \left[1 - 3\left(\frac{-V_{GS} + V_{bi}}{V_{po}}\right) + 2\left(\frac{-V_{GS} + V_{bi}}{V_{po}}\right)^{3/2}\right](1 + \lambda V_{DS}) \tag{3.6}$$

where W and L are channel width and length, respectively, V_{GS} is the gate-to-source voltage, and λ is channel length modulation parameter of the JFET.

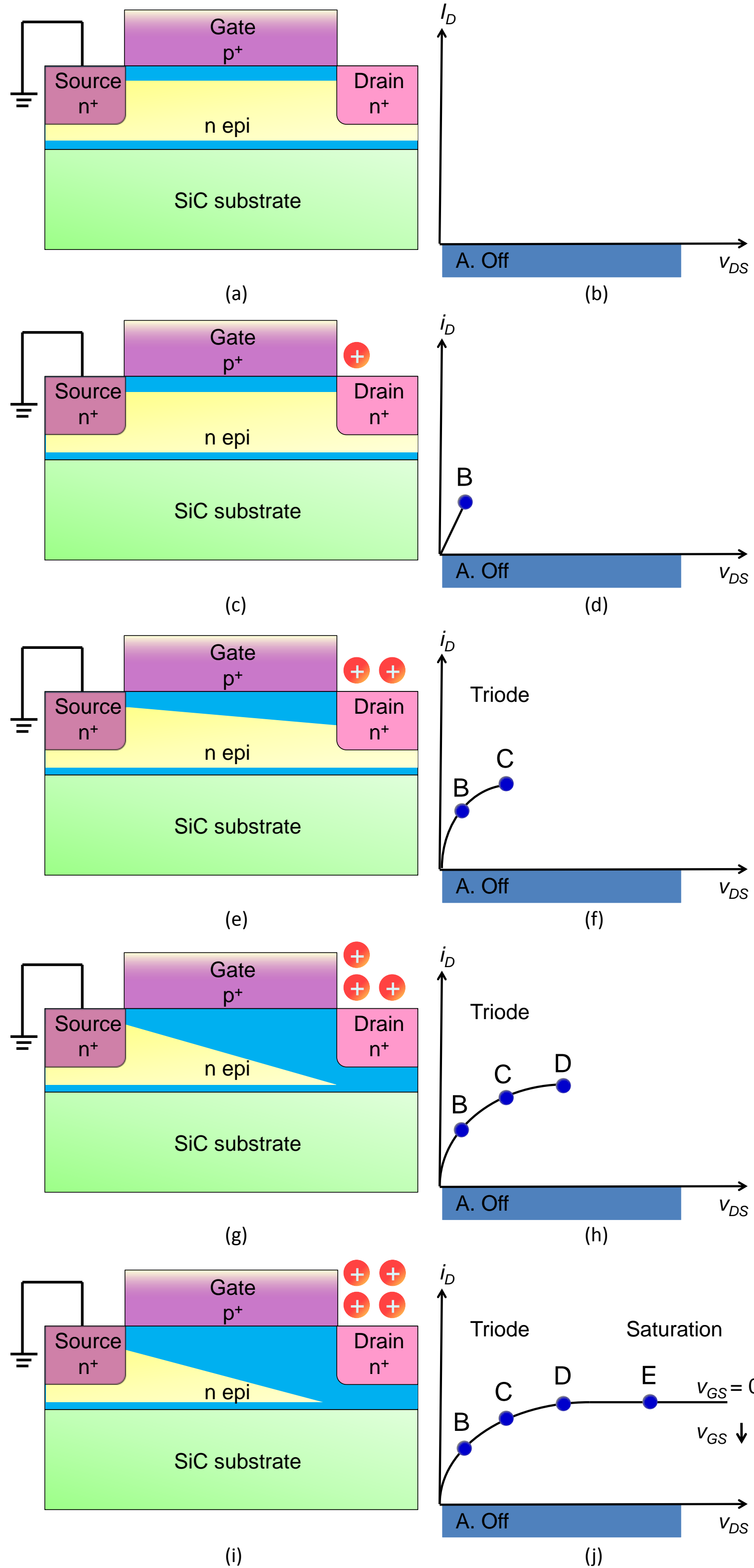

Figure 3.1: Visualization of various phases of JFET operation and the corresponding I_D-V_D characteristics at V_{GS} = 0 V. Note the SiC substrate serves as the body biasing point. The blue color in schematic represents the depletion regions, and the yellow color shows the channel region. The shape of the channel is for the purpose of demonstration and it is not the real situation.

3.3 Fabrication Process

Figure 3.2 is a cross-sectional schematic of a lateral n-channel raised gate 4H-SiC JFET used in this work. The device structure is similar to that work of the NASA Glenn Research Center except the material is changed to 4H-SiC [18]. The transistor consists of p-type 4H-SiC wafer (from Cree Inc.) with three epitaxial layers (from Ascatron AB). A 5 µm p- epitaxial layer with doping concentration of 2×10^{15} cm^{-3}, followed by 300 nm n-epitaxial layer with doping concentration of 1×10^{17} cm^{-3} and 200 nm p^+ epitaxial layer with doping concentration of 2×10^{19} cm^{-3} were grown on the p-type wafer with the resistivity of approximately 1 Ω-cm. The p^+ epitaxial layer served as the gate and n epitaxial layer is used for the channel of JFET. The entire fabrication process flow is shown in Figure 3.3 including seven lithography masks. First, the p^+ gate was time etched using transformer coupled plasma (TCP) etcher with 90 sccm Cl_2 and 10 sccm BCl_3 under RF bias of 150 W. 1 µm plasma-enhanced chemical vapor deposition (PECVD) SiO_2 was patterned to define the source and drain area with nitrogen implantation at 600 ˚C which facilitates Ohmic contact to the metal with reduced damage of crystallinity [19].

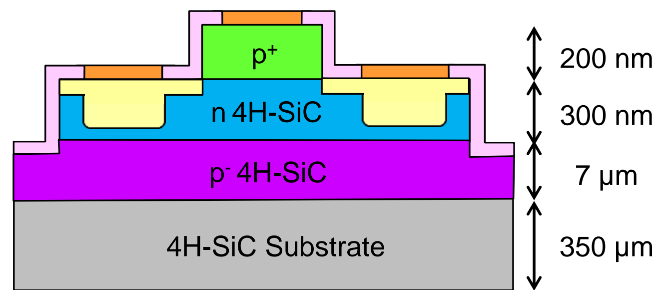

Figure 3.2: Schematic of a lateral n-channel raised gate 4H-SiC JFET.

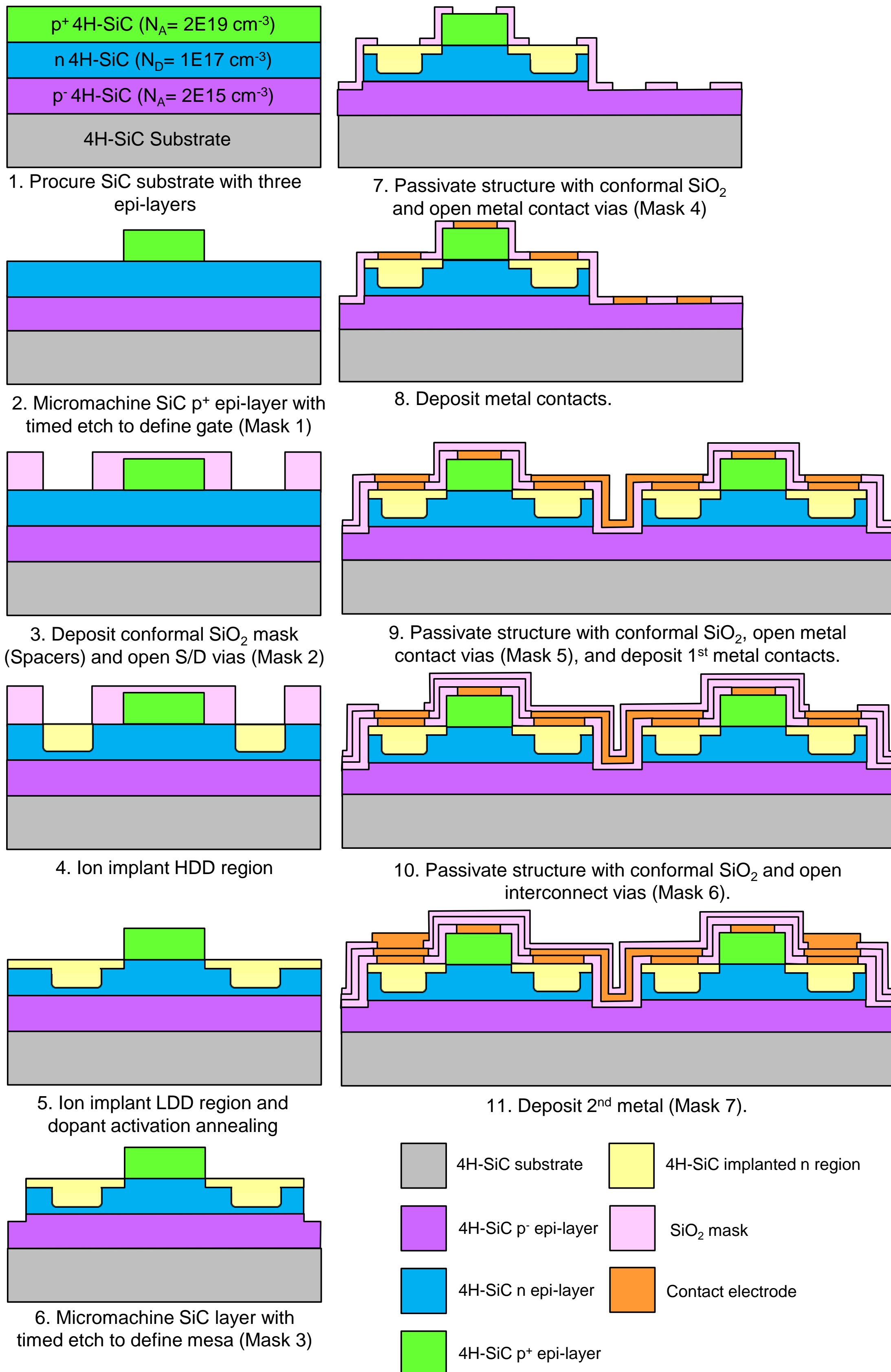

Figure 3.3: Completed fabrication process flow of 4H-SiC JFET and MSM photodetectors.

The implantation of a box profile was formed using 1.4×10^{15}, 7×10^{14}, and 3.6×10^{14} doses at 60, 40, and 20 keV energies, respectively. An example of SiC insulated-gate bipolar transistor (IGBT) of TCAD Sentaurus process simulation has been modified for predicting the dopants concentration distribution and depth profile. The simulation of ion implantation uses the stopping and range of ions in matter (SRIM) which is based on the Monte Carlo simulation method. Based on this simulation, the implantation yields a nitrogen concentration higher than 10^{19} cm^{-3} as shown in Figure 3.4. After ion implantation, the oxide layers were removed by the buffer oxide etching solution (hydrofluoric acid). The second lighter-dose nitrogen was implanted using 3.2×10^{12}, 8×10^{11}, 8×10^{11}, and 1×10^{12} doses at 33, 24, 18, and 10 keV energies, respectively [18].

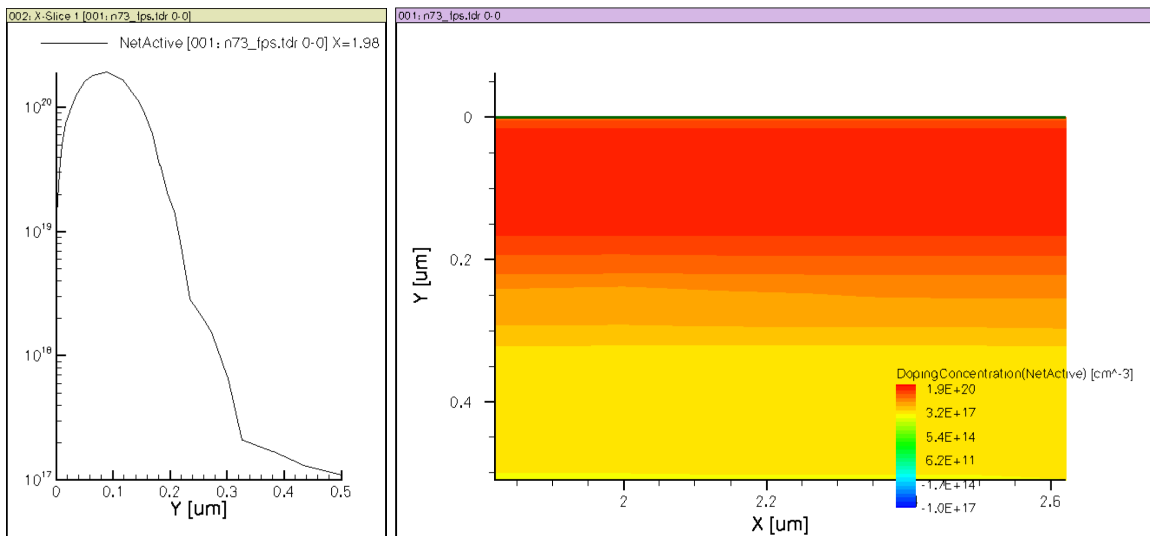

Figure 3.4: Simulated doping profile of heavily doped drain and source region.

The implanted dopants were electrically activated by annealing samples capped with 2 µm PECVD SiO_2 at 1450 °C under an Argon atmosphere for 30 minutes. Figure 3.5 (a) shows the cross-sectional scanning TEM image of the implanted area after annealing. Electron diffraction of the implanted area suggests that the implanted area can be restored back to single crystal after high temperature annealing as shown in Figure 3.5 (b). Figure 3.6 shows the atomic force microscope (AFM) images of SiC sample before and after annealing. The root-mean-square (RMS) roughness is slightly increased from 0.366 nm to 2.65 nm which could be attributed to combination of Si outdiffusion due to the strain created by the ion-implantation damage and non uniform thermal oxidation of SiC surface at high temperature [20].

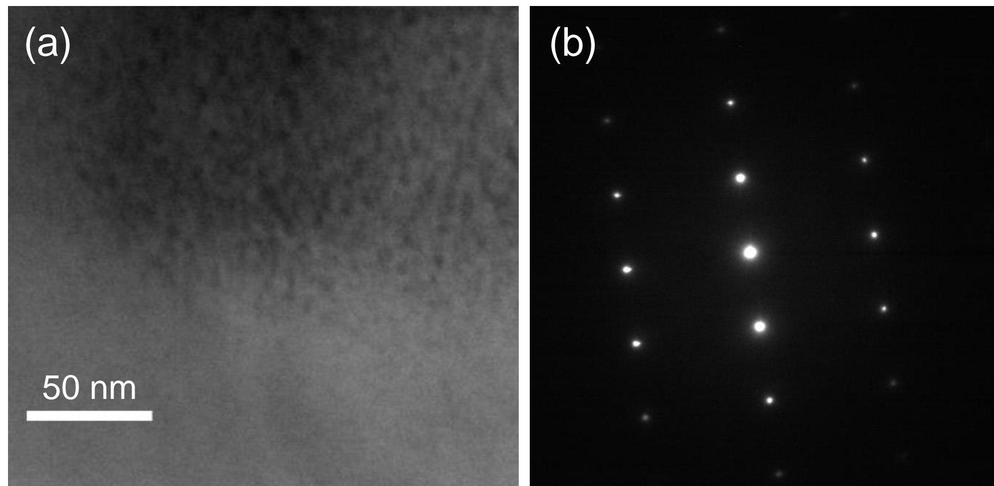

Figure 3.5: (a) Cross-sectional scanning TEM image (b) Electron diffraction of implanted area after annealing at 1450 ℃ under Argon atmosphere for 30 minutes.

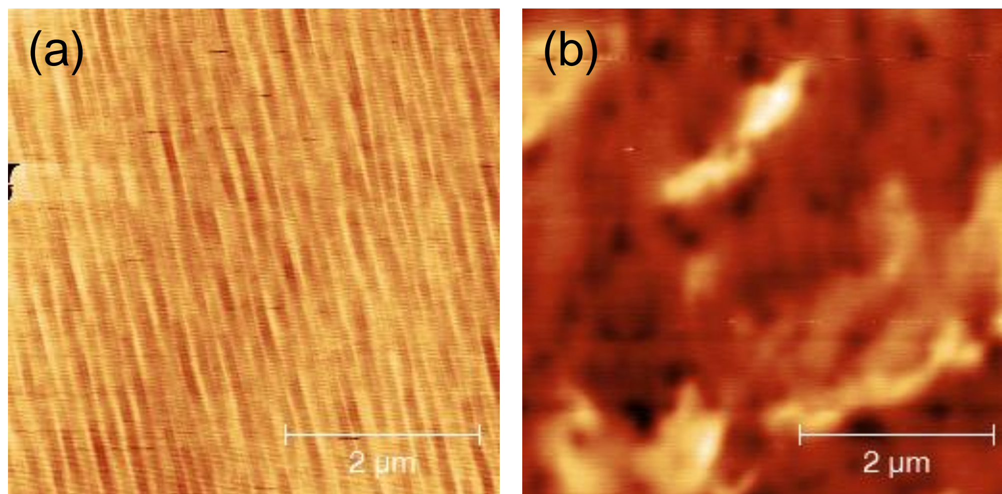

Figure 3.6: AFM images of SiC samples before annealing and after annealing at 1450 ℃ under Argon atmosphere for 30 minutes.

A mesa etch was then used to define the device area using a transformer coupled plasma etcher. The JFET surface was then passivated with PECVD SiO_2 and the 50 nm Ti, 100 nm Ni, and a 50 nm TiW (10% Ti, 90% W) contact was deposited and patterned via lift-off to form the contact electrodes. Note that both JFETs and MSM UV photodetectors (Chapter 2) could be fabricated, as is shown in step 8 of Figure 3.3. The left device is JFET and the right two electrodes represent of one set of interdigitated fingers of MSM photodetector. The metal contacts were annealed with rapid thermal annealing (RTA) at 1000 ℃ for 2 minute under Ar ambient. 200 nm TiW (10% Ti, 90% W) was used for the 1st level of metal interconnects. Finally, the 20 nm Cr and 180 nm Pt was used for 2nd level of metal interconnect and the backside contact of the wafer. Pt was chosen as the final contact due to the compatibility for wire bonding and also helps contacts operate for a significantly longer time under a high temperature environment by protecting the underlying metals [21]. Figure 3.7 shows the as-fabricated 3” 4H-SiC wafer before the final step of the deposition of backside metal contact.

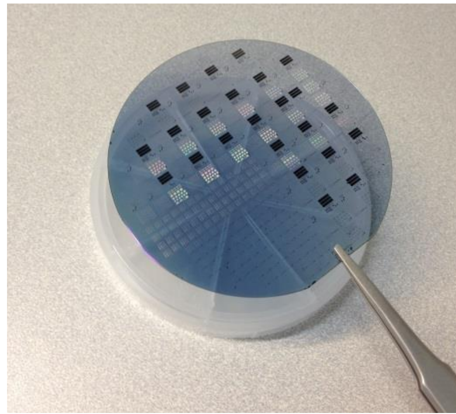

Figure 3.7: Fabricated 3” 4H-SiC wafer.

Devices were characterized on a hot chuck of high temperature probe station (Signatone Inc.) as shown in Figure 3.8. This high temperature probe station consists of ceramic hot chunk, thermal heater, and water cooler, and the chunk temperature goes up to 600 ℃ with low thermal noise of 10^{-9}-10^{-8} A at 600 ℃. An HP 4156B semiconductor parameter analyzer and Agilent B2912A precision source/measurement unit with tungsten probe tips were used to measure the I-V characteristics of the devices as shown in Figure 3.9.

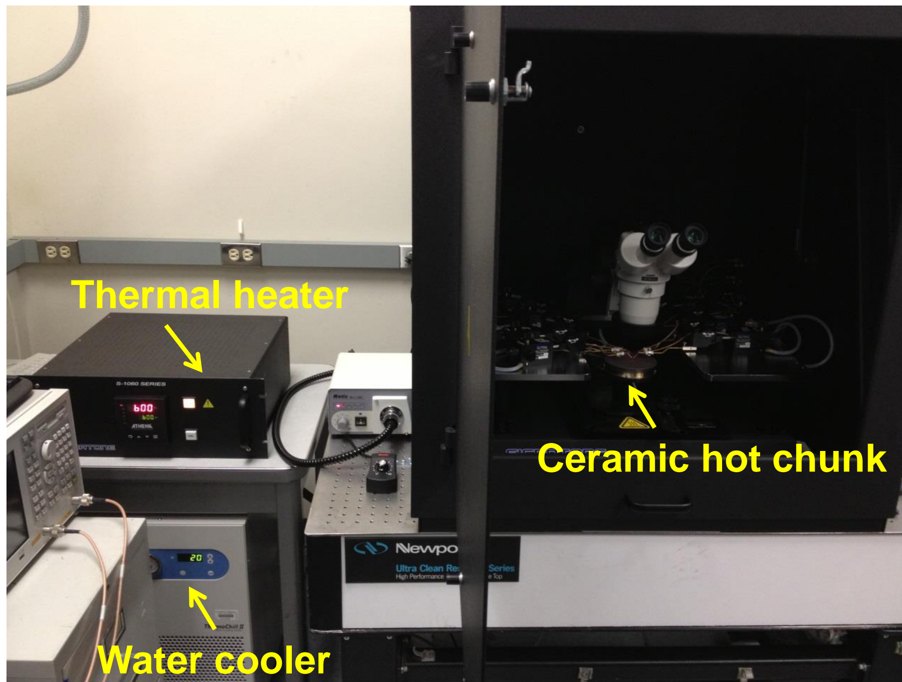

Figure 3.8: High temperature probe station.

Figure 3.9: HP 4156B semiconductor parameter analyzer and Agilent B2912A precision source/measurement unit.

3.4 Metallization of N-Channel Raised Gate JFET

Metallization of 4H-SiC is probably the most difficult problem before the success of commercialization of SiC electronics for high temperature applications. There are many issues to be addressed, such as low-resistance Ohmic contact of both p- and n- type 4H-SiC at elevated temperatures, and the long-term stability of these metal at high temperatures. As shown in Figure 3.10, for an ideal metal n-semiconductor Ohmic contact, metal workfunction (Φ_m) must be smaller than semiconductor workfunction (Φ_s). For an ideal metal p-type semiconductor Ohmic contact, Φ_m must be larger than Φ_s.

Conventionally, it is easier to deposit one metal forms an Ohmic contact with both n-type and p-type semiconductors to save the extra lithography processes. However, it is theoretically impossible to find one metal that forms Ohmic contact with n-type and p-type for the wide-bandgap material such as 4H-SiC. For n-type 4H-SiC, Φ_m has to be smaller than 5.8 eV, and for p-type 4H-SiC, Φ_m has to be larger than 5.8 eV. Some metal workfunctions and 4H-SiC band diagram are shown in Figure 3.11. One practical way to produce Ohmic of 4H-SiC is through heavily doping the surface region of 4H-SiC. Another method is to anneal the metal to introduce a reaction between the metal and 4H-SiC.

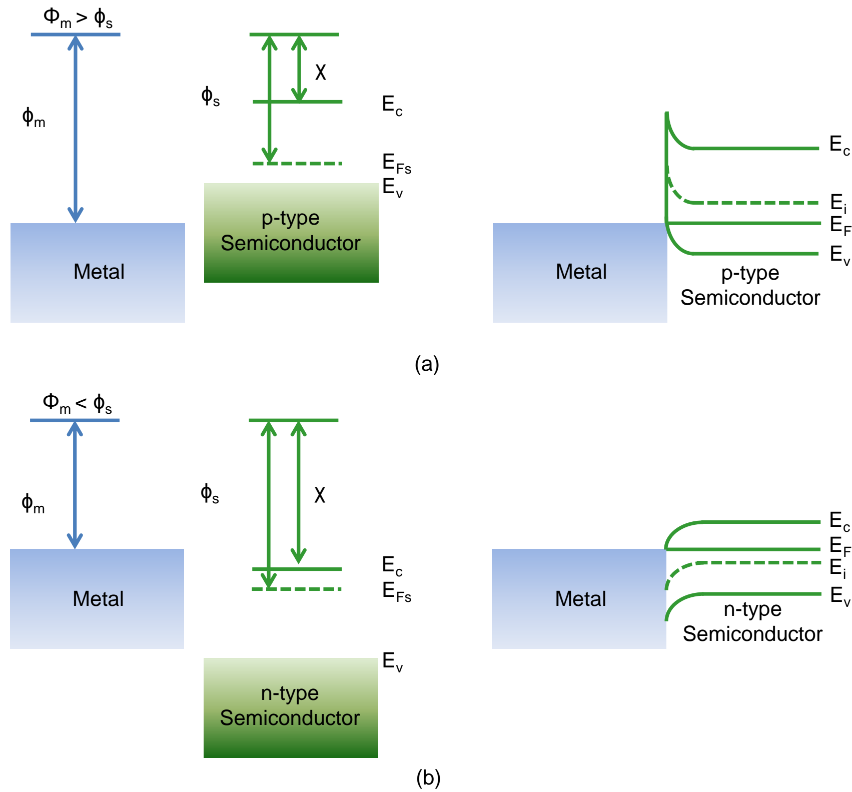

Figure 3.10: Ideal Ohmic contact of metal with (a) p-type semiconductor and (b) n-type semiconductor.

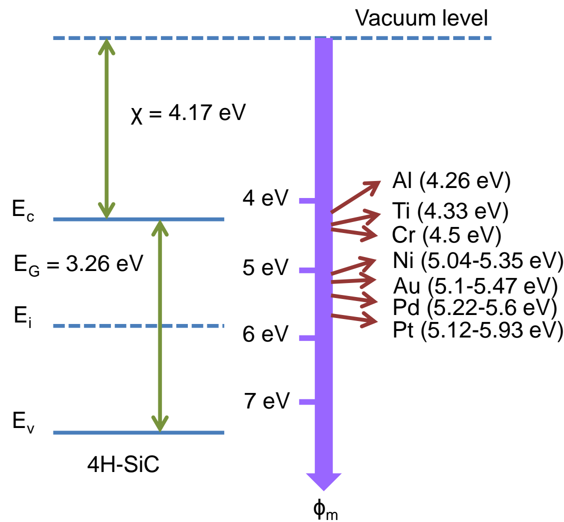

Figure 3.11: Several metal workfunctions compared with the 4H-SiC band diagram.

The specific contact resistance (ρ_c) between metal and semiconductor can be measured using linear transfer length method which is also known as the transmission line method (TLM) [15]. Figure 3.12 shows the optical image of structure of TLM. The mesa must be etched to constrict the current in one direction and the resolution of specific contact resistant is $10^{-6}\ \Omega\ \text{cm}^2$. The contact resistance (R_c) is given by

$$R_c = \frac{\sqrt{\rho_c R_{sh}}}{W} \tag{3.7}$$

where ρ_c is the specific contact resistance between metal and semiconductor (Ω cm^2), R_{sh} is the sheet resistance of the semiconductor (Ω/□), and W is the width of the contact. The sheet resistance is given by

$$R_{sh} = \frac{1}{q\mu_n nD} \tag{3.8}$$

The R_{sh} and ρ_c can be estimated by measuring resistance between contacts with variable distances (d), namely the TLM shown in Figure 3.12, using the following equation,

$$R = \frac{R_{sh}}{W} d + 2\frac{\sqrt{\rho_c R_{sh}}}{W} \tag{3.9}$$

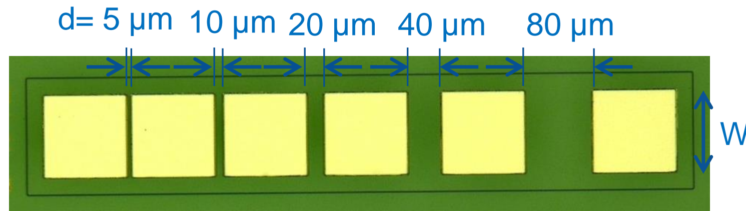

Figure 3.12: Optical image of TLM structure.

In order to simplify the fabrication process of the first generation of raised gate 4H-SiC JFET, one metal stack of 50 nm Ti/100 nm Ni/ 50 nm TiW was chosen for the contact electrodes for both p^+ gate and n^+ source/drain areas. Ti acts as an adhesion layer, Ni is the main contact electrode, and TiW acts as a capping layer which has a high melting point and has been proven to have long term stability after high temperature exposure of 500 °C [22]. Figure 3.13 shows the current-voltage (I-V) measurement of metal and n-type 4H-SiC for TLM structure. The contact is a Schottky contact before RTA and it becomes Ohmic contact after the RTA.

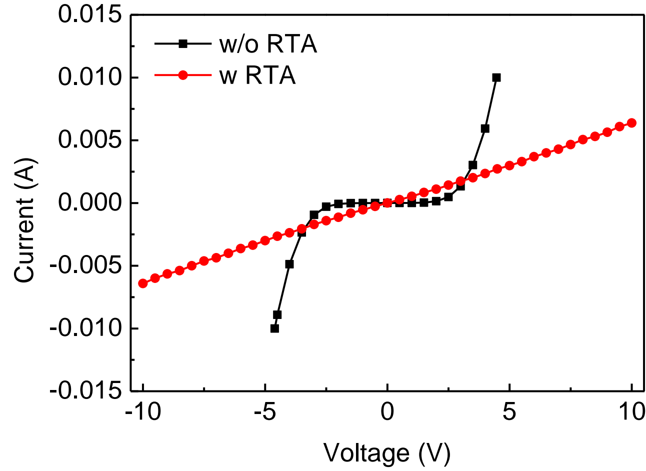

Figure 3.13: Measure I-V curves of metal and n-type 4H-SiC before and after RTA annealing for TLM structure with d = 80 µm.

The measured resistance between contacts versus different distances at room temperature is shown in Figure 3.14. At room temperature, the R_{sh} is 1.84 kΩ/□ and ρ_c is 3.2×10^{-4} Ω cm^2. Several specific contact resistance measurements on 4H-SiC in the literature are listed and summarized in Table 3.1. The specific contact resistance of n-type 4H-SiC, approximately 10^{-4} to 10^{-6} Ω cm^2, is usually lower than that to p-type 4H-SiC, which is approximately 10^{-3} to 10^{-5} Ω cm^2. The temperature dependencies of measured ρ_c are shown in Figure 3.15. The specific contact resistance is slightly decreased from 25 ℃ to 400 ℃, and it begins to rise from 500 ℃ to 600 ℃. The decreases of the specific contact resistance is due to more carriers being excited above the Fermi level at elevated temperature, and this the current density is increased [23]. However, when the temperature is further increased to 550 ℃, the metal contacts, Ti/Ni/TiW, become more unstable as well as show a smaller degree of oxidation [24]. Therefore, the specific contact resistance suddenly increases to 1.14×10^{-3} Ω cm^2 at 600 ℃, implying that a more stable metallization scheme is needed for 4H-SiC.

The fitted ρ_c and R_{sh} are listed in Table 3.2. The total drain and source resistance ($R_{S,D}$) is given by

$$R_{S,D} = R_{sh} \times NR_{S,D} + \frac{\sqrt{\rho_c R_{sh}}}{W} \tag{3.10}$$

where $NR_{S,D}$ are the number of squares of the n-type 4H-SiC between the edge to the edge of the source or drain contacts (Ω/□) [25].

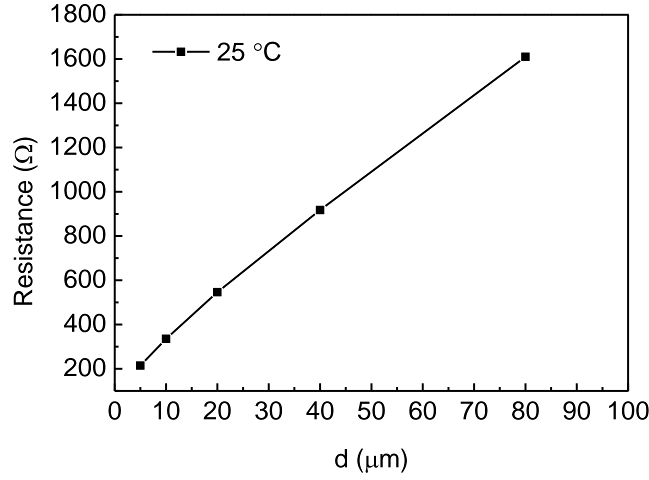

Figure 3.14: Measured resistance between contacts vs. different distances at room temperature of Ti/Ni/TiW metal stacks and n-type 4H-SiC.

Poly type	Metals	Doping (cm^{-3})	ρ_c(Ω cm^2)	Ref
n	Ni-Cr	1.3×10^{19}	1.2×10^{-5}	[26]
n	TiC	1.3×10^{19}	4×10^{-5}	[27]
n	Ni	1×10^{19}	6×10^{-6}	[28]
n	TiW (30:70)	1.3×10^{19}	1.2×10^{-4}	[22]
n	W-Ni (50:50)	2×10^{19}	5.81×10^{-4}	[29]
p	TiC	1×10^{20}	6×10^{-5}	[27]
p	Ni	1×10^{21}	1.5×10^{-4}	[28]
p	TiW (30:70)	6×10^{18}	1.2×10^{-4}	[22]
p	Ge/Ti/Al	4.5×10^{18}	1.03×10^{-4}	[30]
p	Al-Si-Ti	$3\text{-}5\times10^{19}$	9.6×10^{-5}	[31]
p	Ni/Ti/Al/Ni	$3\text{-}4\times10^{19}$	1.5×10^{-5}	[32]

Table 3.1: Specific contact resistance measurements on 4H-SiC in the literature.

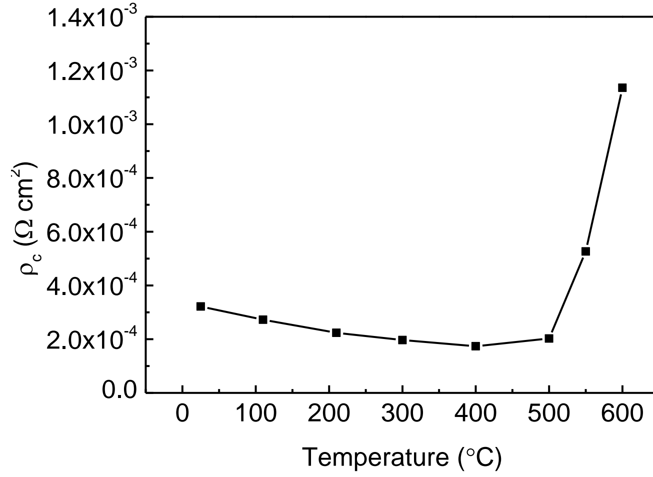

Figure 3.15: Temperature dependences of specific contact resistance of Ti/Ni/TiW metal stacks to n^+ 4H-SiC.

Temperature (°C)	R_{sh} (kΩ/□)	ρ_c (Ω cm^2)
25	1.842	3.22×10^{-4}
110	1.700	2.72×10^{-4}
210	1.666	2.24×10^{-4}
300	1.660	1.97×10^{-4}
400	1.664	1.74×10^{-4}
500	1.627	2.02×10^{-4}
550	1.378	5.26×10^{-4}
600	1.090	1.136×10^{-3}

Table 3.2: Sheet resistance and specific contact resistance of Ti/Ni/TiW metal stacks and n-type 4H-SiC at different temperatures.

Figure 3.16 shows the *I-V* measurement of metal and p^+ gate of 4H-SiC for the TLM structure. The contact is still Schottky in nature after the RTA except the current intensity is increased. There is one study that reported the 50 nm Ti/ 100 nm Ni is able to form an Ohmic contact with both n- and p-type 4H-SiC after RTA [33]. In our case, it only works for the n-type 4H-SiC. However, a non ideal or semi-rectifying contact to JFET's gate region is still acceptable for the JFET operation [5].

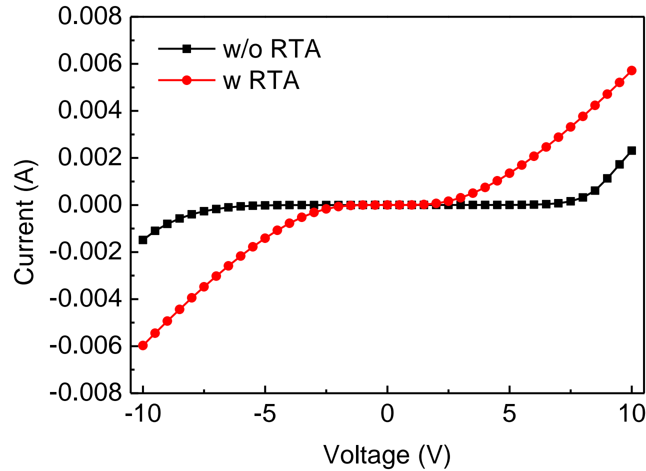

Figure 3.16: Measure I-V curves of metal and p-type 4H-SiC for TLM structure with d = 5 μm.

3.5 Electrical Properties of N-Channel Raised Gate JFET

3.5.1 Characterization of N-JFET at Room Temperature

Figure 3.17 shows the optical image of as-fabricated 4H-SiC lateral JFET with L = 10 μm and W = 100 μm. The active channel area is 2×10^{-5} cm^2. The top square is the gate probing area and the bottom two squares can be either drain or source areas. The contact metal of the gate region is protected by the PECVD oxide for the better life time of the device. Figure 3.18 shows the drain current versus drain-to-source voltage characteristics of a 100 μm /10 μm JFET before and after RTA at room temperature. It is clear that there is a high resistance in the linear region from 0 V to 2.5 V without RTA, and the saturation current is 2.5 times smaller than the one after RTA due to the large source and drain resistance ($R_{S,D}$). After the RTA, the on-resistance of JFET (R_{on}) decreased to 59.3 mΩ cm^2. The device is fully-on at V_{GS} = 0 V and cut-off at V_{GS} = -8 V. λ is estimated to be 3.88×10^{-3} V^{-1}. The drain-to-source saturation current is 16.8 mA/mm and the current density is 84 A/cm^2 at V_{DS} = 20 V and V_{GS} = 0 V. Figure 3.19 (a) shows the drain current versus gate-to-source voltage characteristics at V_{DS} = 20 V and the threshold voltage can be extracted from the extrapolated intercept of x axis of $\sqrt{\frac{I_{DS}}{1+\lambda V_{DS}}}$ vs. V_{GS} plot at V_{DS} = 20 V in Figure 3.19 (b). The threshold voltage is approximately -6.8 V at 25 °C.

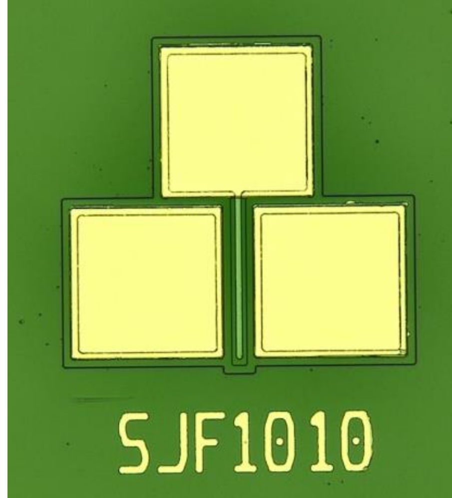

Figure 3.17: Optical image of a n-channel raised gate 4H-SiC JFET with $L = 10$ µm and $W = 100$ µm.

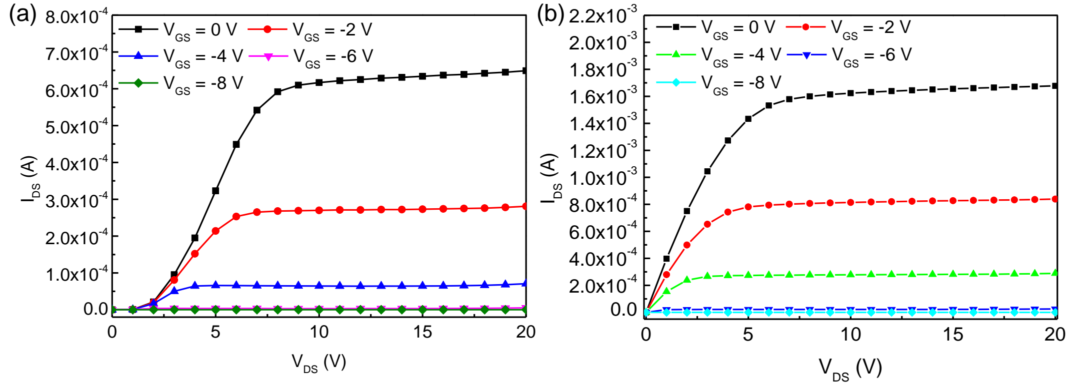

Figure 3.18: I_{DS}-V_{DS} characteristics of a n-channel 4H-SiC JFET (a) before RTA (b) after RTA under different V_{GS} and with W/L= 100 µm/10 µm at 25 ℃.

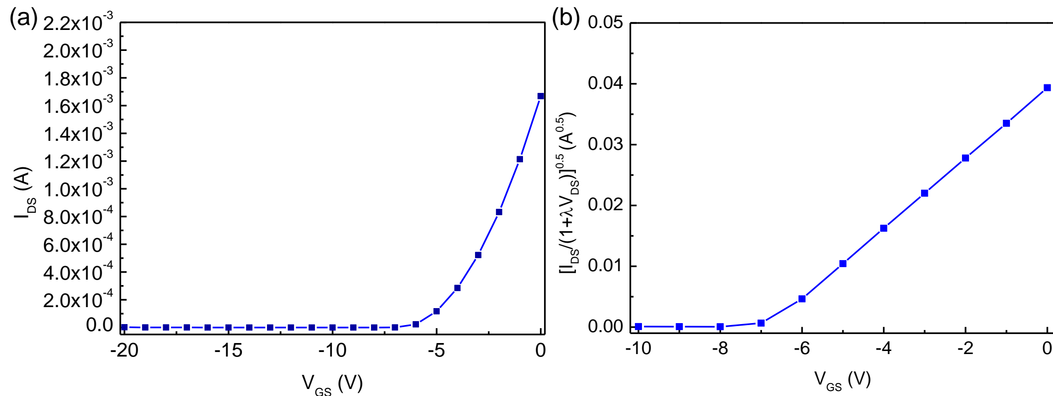

Figure 3.19: (a) I_{DS}-V_{GS} (b) $\sqrt{I_{DS}}$-V_{GS} characteristics of a n-channel 4H-SiC JFET with W/L= 100 µm/10 µm and $V_{DS} = 20$ V at 25 ℃.

The transconductance (g_m) could be extracted from square-law model using Taylor expansion near $V_{GS} = V_T$ as follows [5, 25]

$$k' = \frac{3I'_P}{4V'_{po}} = \frac{\mu_n \varepsilon_s n}{2DN_D} \tag{3.11}$$

$$g_m = 2\sqrt{\frac{W}{L}k' I_{DS}} = \frac{2I_{DS}}{V_{GS}-V_T} \tag{3.12}$$

The estimated g_m of 4H-SiC JFET is 4.94 μS/μm (normalized with the channel width of 100 μm) at room temperature and is approximately two times larger than the reported JFET with the similar device configuration using 6H-SiC [25]. The estimated output resistance (r_o) is 1.65×10^5 Ω. The intrinsic gain ($g_m r_o$) of single 4H-SiC JFET is approximately 81.5 or 38.2 dB at $V_{GS} = 0$ V.

3.5.2 Characterization of N-JFET at High Temperatures

Figure 3.20 (a)-(g) show the I_{DS}-V_{DS} characteristics of n-channel raised gate 4H-SiC JFET from 110 to 600 ℃. The JFET shows excellent I_{DS}-V_{DS} characteristics over the entire temperature range. Figure 3.20 (h) shows the I_{DS}-V_{DS} curves under a gate-to-source 0 V bias and at incremental temperatures up to 600 ℃. Figure 3.21 shows the I_{DS}-V_{GS} curves under a drain-to-source 20 V bias and at incremental temperatures up to 600 ℃. A monotonic decrease in saturation current is observed, and this can be attributed to the power law degradation of the electron mobility at elevated temperatures [34]. At the zero temperature coefficient (ZTC) point approximately at -6.6 V, the current is insensitive to temperature [34]. The degradation of the mobility also causes the R_{on} to increase from 72.0 to 280.2 mΩ cm^2. The I_{Dsat} of JFET at $V_{GS} = 0$ V and 600 ℃ is approximately 82 % less than its value at room temperature. However, the device is fully functional that the change of I_{Dsat} is in response to the applied gate voltage at 600 ℃, as shown in Figure 3.20 (g). The off current (I_{off}) at $V = -9$ V increases from 6.31×10^{-9} A to 1.97×10^{-7} A as the temperature increase from 110 ℃ to 600 ℃ due to the decrease of the energy bandgap of 4H-SiC at elevated temperatures (Figure 1.4) [34, 35]. However, the order of 10^{-7} A leakage current is quite larger than theoretically predicted, and this issue requires further study [25]. The calculated on/off drain saturation current ratio (I_{Dsat}/I_{off}) is 2.66×10^5 at room temperature and decreases to 1.53×10^3 at 600 ℃. Unlike the n-channel raised gate 6H-SiC JFET with W/L= 200 μm/10 μm reported from NASA, the I_{Dsat}/I_{off} at 500 ℃ is approximately 50 in the beginning and needs hundred hours of "burning time" to make the Ti/$TaSi_2$/Pt metal contact achieve good Ohmic contacts and increases the I_{Dsat}/I_{off} to more than 10^3 [6, 36]. The fabricated 4H-SiC JFET shows a decent on/off current ratio even at 600 ℃ in the first hour of operation.

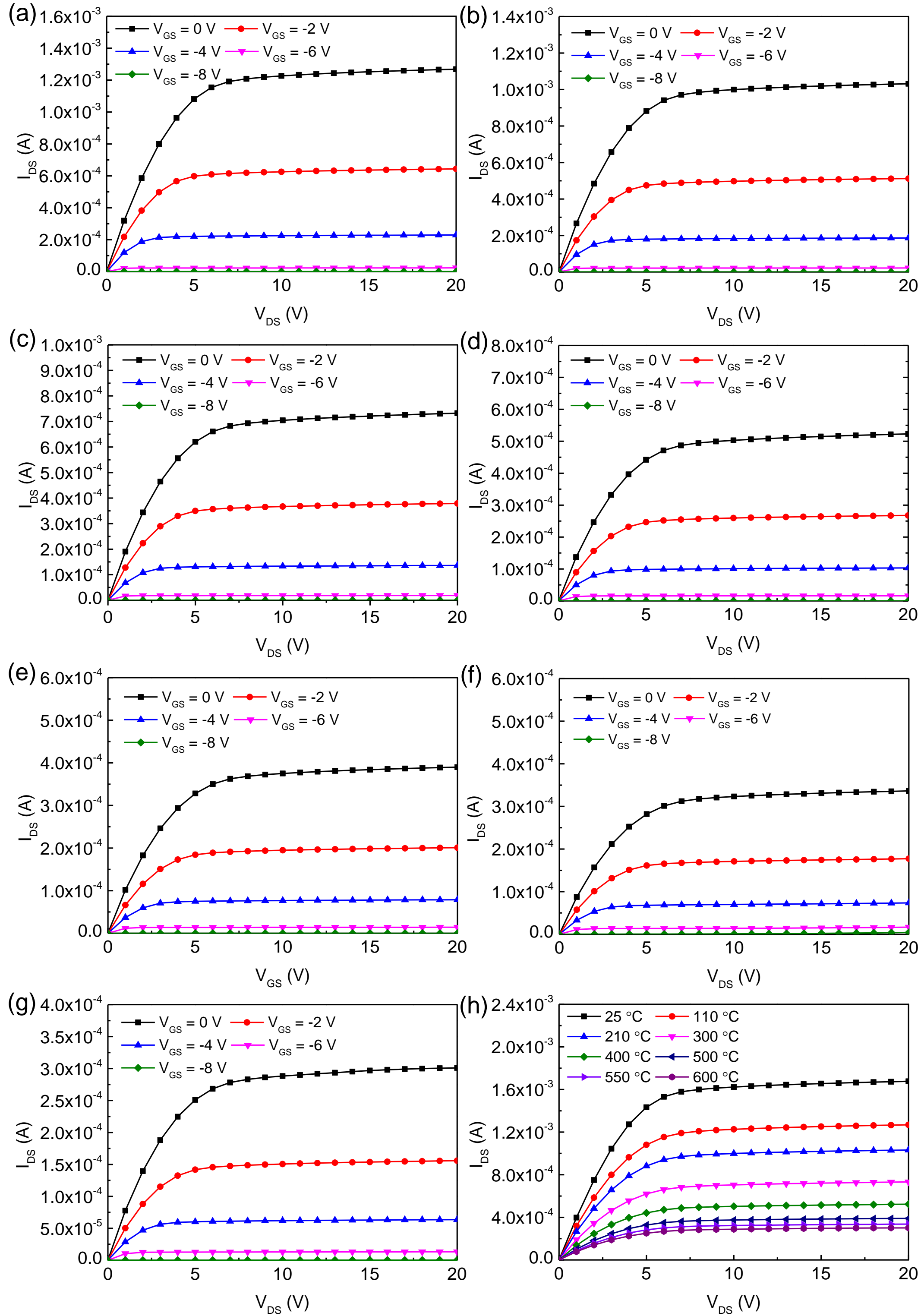

Figure 3.20: I_{DS}-V_{DS} characteristics of a n-channel 4H-SiC JFET under different V_{GS} and with W/L= 100 μm/10 μm (a) at 110 ℃ (b) at 210 ℃ (c) at 300 ℃ (d) at 400 ℃ (e) at 500 ℃ (f) at 550 ℃ (g) at 600 ℃. (h) Temperature dependences of I_{Dsat} of a n-channel 4H-SiC JFET at V_{GS} = 0 V and with W/L= 100 μm/10 μm.

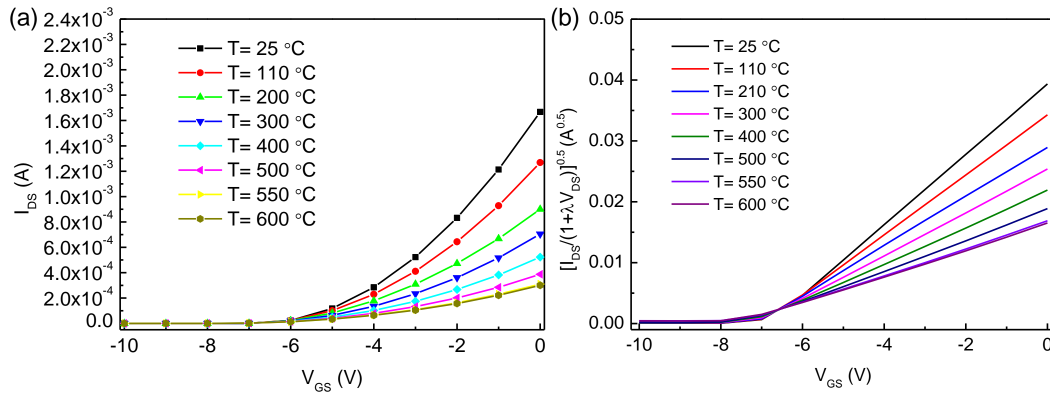

Figure 3.21: (a) I_{DS}-V_{GS} (b) $\sqrt{I_{DS}}$-V_{GS} characteristics of a n-channel 4H-SiC JFET under V_{DS} = 20 V and with W/L= 100 µm/10 µm at different temperatures.

Figure 3.22 shows the extracted threshold voltage at different temperatures. The V_T is approximately shifted with the rate of -1.38 mV/ ˚C. The temperature dependencies of estimated transconductances based on the equation 3.12 and the intrinsic gain of the JFET at V_{GS} = 0 V are shown in Figure 3.23. The g_m at 600 ˚C is 0.79 µS/µm, which is only 16 % of its value at room temperature. The g_m of 4H-SiC JFET 600 ˚C is larger than the g_m of 6H-SiC JFET with similar doping concentration and structure (~0.55 µS/µm at 595 ˚C) [25]. Note that the 6H-SiC JFET only has I_{Dsat}/I_{off} = 7.2 at 595 ˚C. The intrinsic gain of the JFET has relatively weak temperature dependence but the overall tendency is to decrease with temperature, because the output resistance is increased from 1.65×10^5 to 7.25×10^5 Ω, compensating for the effect of the reduced g_m at high temperatures. The results suggest that 4H-SiC JFET shows promising performance for high temperature amplifier applications. The complete electrical properties of n-channel raised gate 4H-SiC JFET are listed and summarized in Table 3.3.

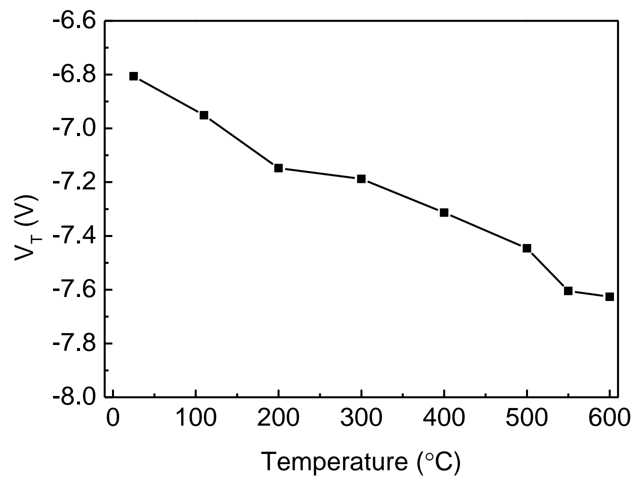

Figure 3.22: Temperature dependence of threshold voltage of a n-channel 4H-SiC JFET with W/L= 100 µm/10 µm.

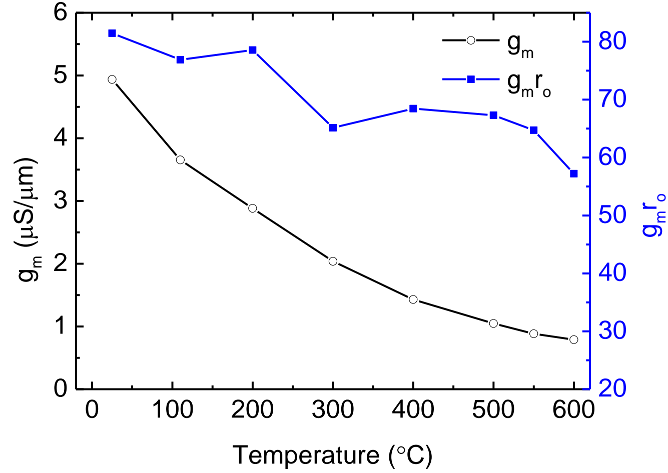

Figure 3.23: Temperature dependence of transconductance and intrinsic gain of of a n-channel 4H-SiC JFET with W/L= 100 µm/10 µm.

Temperature (℃)	$V_T(V)$	g_m $(\mu S/\mu m)$	R_{on} $(m\Omega\ cm^2)$	$r_o\ (\Omega)$	$\lambda\ (mV^{-1})$	$g_m r_o$	I_{Dsat}/I_{off}
25	-6.81	4.94	59.3	1.65×10^5	3.88	81.5	2.66×10^5
110	-6.95	3.65	72.0	2.10×10^5	4.03	76.9	9.88×10^4
210	-7.15	2.88	87.3	2.73×10^5	3.81	78.6	8.96×10^4
300	-7.19	2.04	123.21	3.20×10^5	4.65	65.1	4.24×10^4
400	-7.31	1.43	172.24	4.78×10^5	4.33	68.4	2.44×10^4
500	-7.45	1.05	214.00	6.42×10^5	4.32	67.3	1.15×10^4
550	-7.60	0.88	249.17	7.32×10^5	4.41	64.7	1.56×10^3
600	-7.63	0.79	280.23	7.25×10^5	5.02	57.2	1.53×10^3

Table 3.3: Extracted parameters of n-channel raised gate 4H-SiC JFET with W/L= 100 µm/10 µm at various temperatures. g_m, R_{on}, r_o , λ and $g_m r_o$ is based on V_{GS} = 0 V. I_{Dsat}/I_{off} is the ratio of current at V_{GS} = 0 V and V_{GS} = -9 V.

3.5.3 Reliability

Compared to Si and III-V semiconductors, 4H-SiC is nearly chemically inert and has high thermal stability with low atom mobility [37]. However, thermally activated degradation between metal-SiC interface and other materials, such as the insulator, metal and packaging, will limit the high temperature durability and consequently hinder the commercialization of 4H-SiC electronics [5, 6, 24]. Therefore, it is important to study the reliability of the fabricated 4H-SiC JFET. Two adjacent 4H-SiC n-channel JFET devices with W/L = 100 µm/10 µm on the same chip were used in this reliability test. Due to the temperature limitation of the hot-plate, the temperature 540 ℃ was set up for the

reliability test. The sample was periodically heated to 540 ℃ on a pre-heated hot-plate in ambient air. The hot-plate was turned off and the sample is naturally cooled down by air for at least twenty minutes on the hotplate. The sample was then placed on a high-temperature probe station for the measurement of *I*-*V* characteristics. This method was repeated hourly for the first twenty hours and then extended to five hour periods. Figure 3.24 shows the I_{DS}-V_{DS} and I_{DS}-V_{GS} characteristics of one JFET at 0, 25th, 50th, 75th, and 90 hours at 540 ℃. Figure 3.25 illustrates the measured variation of transconductance for two n-channel JFETs as a function of 540 ℃ operating time over 90 hours. The g_m is normalized to the initial value of g_{m0}. The fluctuation of I_{DS} and g_m is due to the different probing forces applied on the metal contact for each measurement. The measured g_m changed less than 10 % and 3 % for the first and second JFETs, respectively, over the 90 hour test at 540 ℃. After the 90 hours testing time, the devices no longer exhibited any transistor characteristics. Figure 3.26 is the optical image of one JFET after 90 hours. The metal contacts become very rough. The heating and cooling cycle for each test caused the metal contacts to delaminate due to the thermal stress developed within the three layers of metal stacks. To avoid this, the device can be bonded to the high temperature ceramic packaging such as aluminum oxide [5] or aluminum nitride [38, 39]; however, the failure of the wire bonding must also be considered in the reliability test.

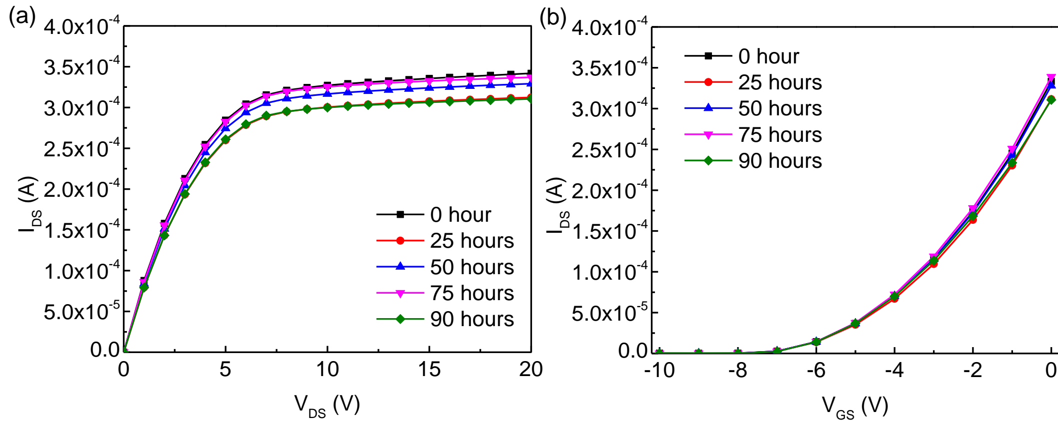

Figure 3.24: (a) I_{DS}-V_{DS} characteristics at V_{GS} = 0 V and (b) I_{DS}-V_{GS} characteristics at V_{DS} = 20 V during 0, 25th, 50th, 75th, and 90 hours of electrical operation at 540 ℃ for a n-channel 4H-SiC JFET with W/L = 100 μm/10 μm .

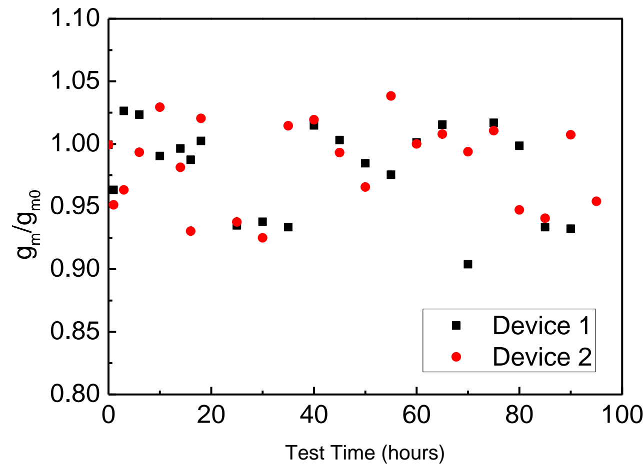

Figure 3.25: Normalized g_m versus test time at 540 ℃ through 90 hours for a n-channel 4H-SiC JFET with W/L = 100 μm/10 μm.

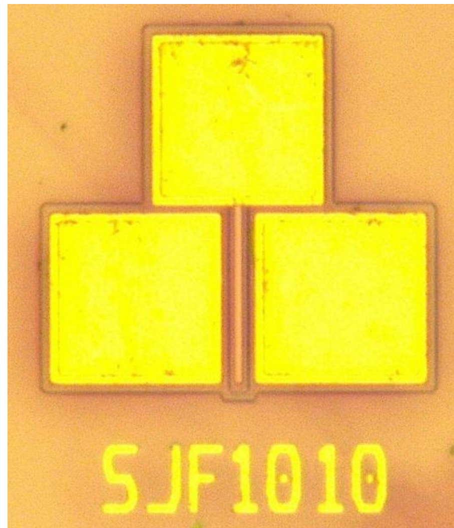

Figure 3.26: Optical image of a n-channel 4H-SiC JFET with W/L = 100 μm/10 μm after thermal reliability test at 540 ℃ after 90 hours.

3.6 TCAD Simulation of N-Channel Raised Gate JFET

Technology Computer Aided Design (TCAD) device simulator allows the device engineer to design and optimize the current and other electrical properties for the device. In this section, Synopsys Sentaurus device simulation was used to model the behavior of the n-channel raised gate 4H-SiC JFET. Because the Sentaurus process is not fully functional for 4H-SiC process modeling, we only use the modified example of 4H-SiC IGBT for doping concentration and distribution of ion implantation which has already been discussed in Section 3.3. Note that the Silvaco International does offer both process and device simulation of 4H-SiC [40]. Due to the lack of the access to Silvaco device

simulation, Sentaurus structure editor was used to build the two-dimensional device structure of 4H-SiC as shown in Figure 3.27. The JFET has a gate length of 10 μm and the source/drain width of 100 μm. The distance between the edge of the gate and the edge of the source/drain is 5 μm. For comparison, Figure 3.28 shows the *I*-*V* curves of the simulated and measured devices at 25 and 600 ℃. In the saturation region, the simulated device exhibits a similar I_{DS} and r_o with the measured one for both at 25 and 600 ℃. The main difference is that the simulated device has smaller V_T and leakage current. The V_T of the simulated device at 25 and 600 ℃ are approximately 4.65 and 5.89 V, respectively, while the V_T of the measured device varies from -6.8 to -7.63 V from 25 to 600 ℃. The leakage current at V_{GS} = -8 V and at 25 and 600 ℃ are < 10^{-18} A and 8.16×10^{-11} A, respectively. The main reasons for these differences could be attribute to:

(1) The quality of material. There are some uncertainties in the material parameters for the real device, such as doping density of the p-n junction, defects, etc. The manufacturer specifies a ±5% variation in doping concentration and thickness of the three epitaxial layers. This contributes to the different built-in voltage of pn junction. Besides, the defects inside the channel region may cause the leakage current increases [41, 42]. Figure 3.29 represents an Arrhenius plot of the log of the drain current versus 1/T at V_{GS} = - 10 V. From the slope fit at different data points, the activation energy is approximately 0.05 – 0.5 eV. These values are significantly less than the half the energy bandgap of the 4H-SiC, which means there is an extrinsic leakage mechanism. This leakage mechanism could either be impurities, defect related, or a surface oxide conduction process [43]. In this process, the PECVD oxide was used for the surface passivation and its resistance to the high thermal heats has not been fully studied, which could contribute the leakage current path at high temperature [6].

(2) Abrupt interface of nitrogen implanted box and n channel. Sentaurus structure editor assumes an abrupt interface between implantation box and channel area, which is not a case in the real fabrication process (Figure 3.5). When the junction is formed, the current generation at reverse bias can be simplified as (assuming one side doping is significantly larger than the other side) [39]

$$I = -qAn_i\left[\frac{n_i}{N}\sqrt{\frac{Dm}{\tau}} + \frac{W}{2\tau}\right] \tag{3.13}$$

Where *A* is the area of the junction, *N* is the doping density of the light doping side, *D* is the minority diffusion constant, and τ is the effect minority carrier lifetime. The first term is the minority carrier diffusion current and the second term is from thermal generation or recombination of carriers that occurs in the depletion region at a biased diode. The non-abrupt nature of the n^+-n junction and the non-recoverable crystal damage caused by the ion implantation after thermal annealing must be considered in future TCAD simulation.

(3) Stable Ohmic contact of both p and n junction. The rectifying behavior of metal contacts at p^+ gate in the real device adds to the leakage current path at high temperature [44].

In summary, the built structure for simulation has some deviation from the exact value of V_T and leakage current value, but it can still be used to predict I_{Dsat} and the temperature trend of JFET electrical properties. In the future, calibration of TCAD to the measured data of JFET will benefit the design optimization study.

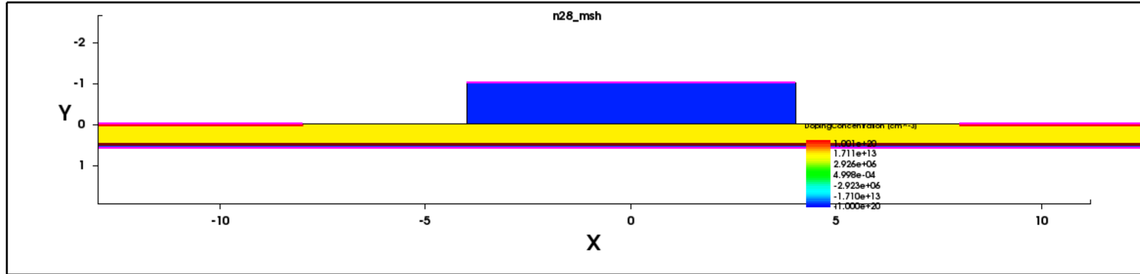

Figure 3.27: Raised gate JFET structure generated by the Sentaurus structure editor.

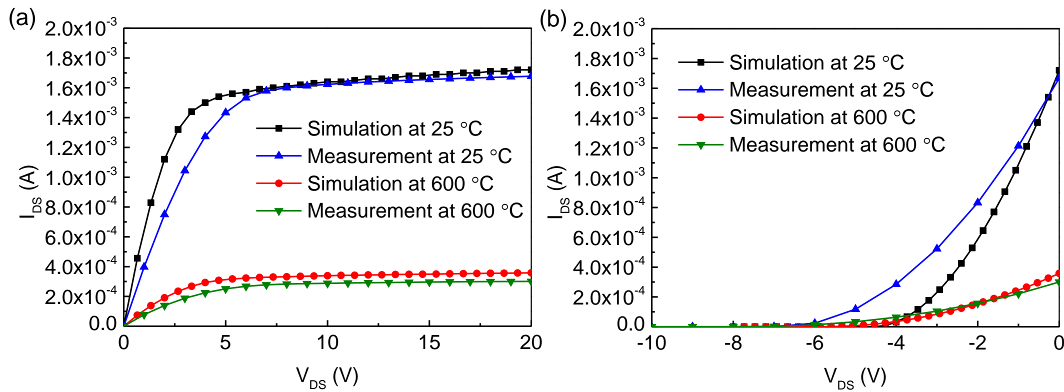

Figure 3.28: Measured and Simulated (a) I_{DS}-V_{DS} characteristics at V_{GS} = 0 V and (b) I_{DS}-V_{GS} characteristics at V_{DS} = 20 for n-channel 4H-SiC JFETs with W/L = 100 μm/10 μm at 25 and 600 °C.

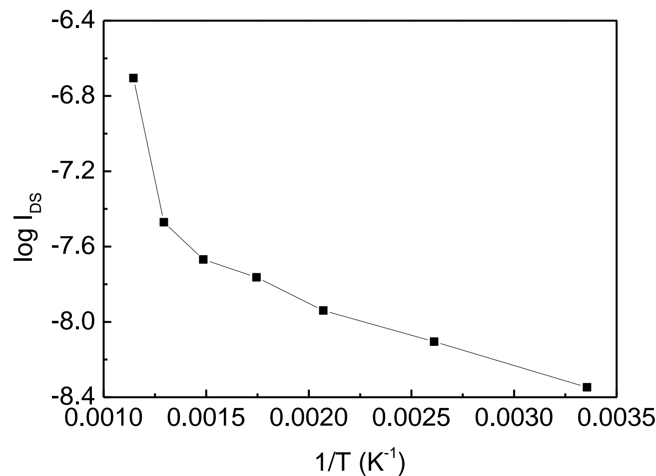

Figure 3.29: Arrhenius plot of log of drain leakage current versus $1/T$ at V_{GS} = -10 V of a n-channel 4H-SiC JFET with W/L = 100 μm/10 μm.

3.7 SPICE Parameter Extraction and Device Modeling

To fully realize the SiC JFET integrated circuit technology, simulation of circuit topology and understanding its high temperature behavior is needed [45-47]. In this section, the SPICE model of individual JFET is built at temperatures up to 600 ℃. A JFET SPICE DC model level 1 was chosen, and I_{DS} is expressed in SPICE with the extracted parameters as follows

If V_{GS}-$V_T < 0$,

$$I_{DS} = 0 \tag{3.14}$$

If $V_{DS} < V_{GS}$-V_T,

$$I_{DS} = \beta(1+\lambda V_{DS})V_{DS}[2(V_{GS}-V_T)-V_{DS}] \tag{3.15}$$

If $V_{DS} < V_{GS}$-V_T,

$$I_{DS} = \beta(1+\lambda V_{DS})(V_{GS}-V_T)^2 \tag{3.16}$$

where is the β transconductance coefficient which can be obtained by squaring the slope of linear function in Figure 3.19 (b). The parameters for the SPICE model are listed in Table 3.4.

Temperature (℃)	$V_T(V)$	β	λ (mV^{-1})
25	-6.81	3.34×10^{-5}	3.88
110	-6.95	2.43×10^{-5}	4.03
210	-7.15	1.83×10^{-5}	3.81
300	-7.19	1.29×10^{-5}	4.65
400	-7.31	8.82×10^{-6}	4.33
500	-7.45	6.30×10^{-6}	4.32
550	-7.60	5.31×10^{-6}	4.41
600	-7.63	4.62×10^{-6}	5.02

Table 3.4: The extracted SPICE parameters of a n-channel 4H-SiC JFET with W/L= 100 μm/10 μm from 25 to 600 ℃.

Figure 3.30 compares the measured I_{DS}-V_{DS} with the device simulation with SPICE. Good agreement between simulations and measurements has been achieved for all the temperature ranges.

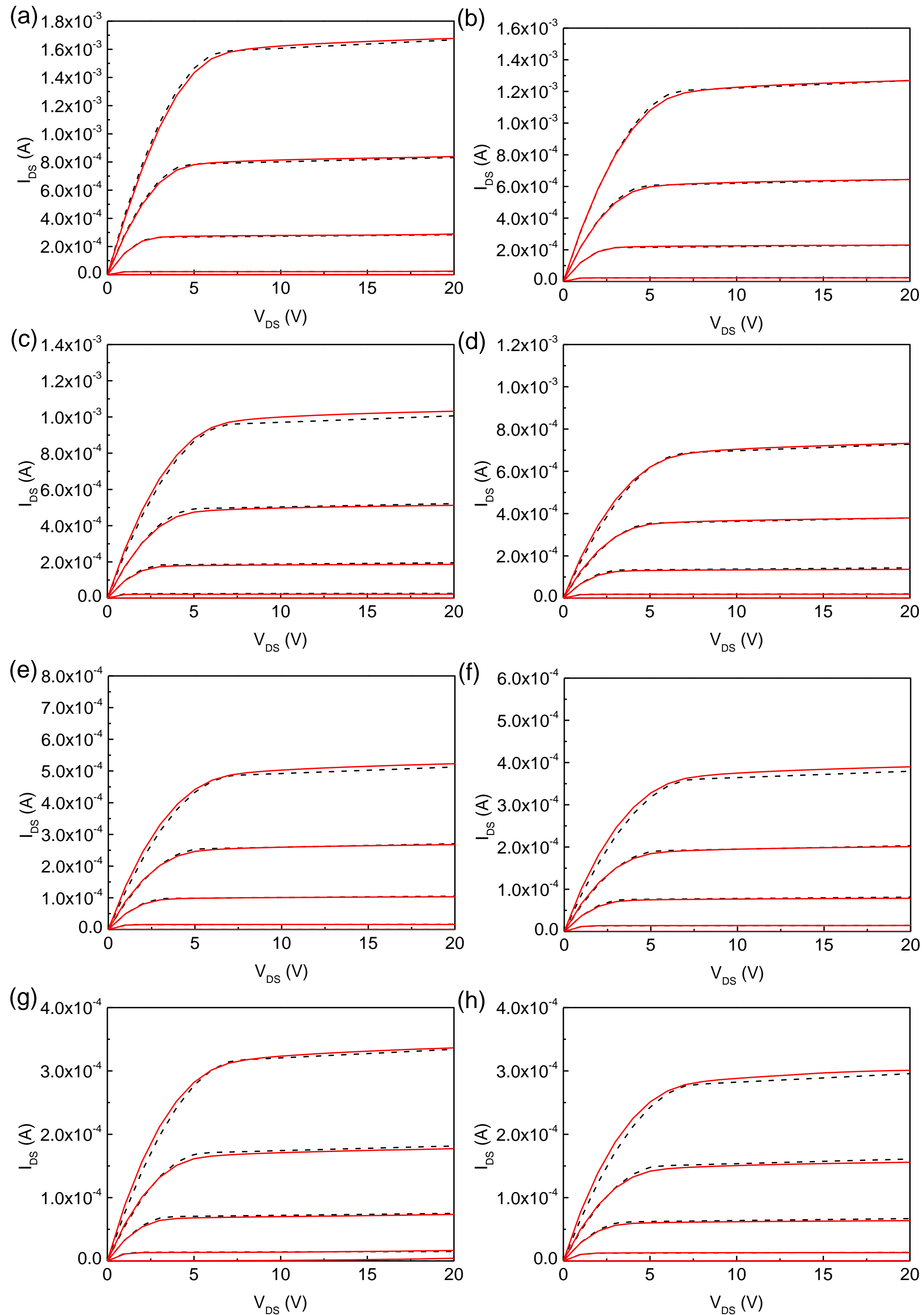

Figure 3.30: Modeled and measured I_{DS}-V_{DS} characteristics of a n-channel 4H-SiC JFET under different V_{GS} and with W/L= 100 μm/10 μm (a) at 110 ℃ (b) at 210 ℃ (c) at 300 ℃ (d) at 400 ℃ (e) at 500 ℃ (f) at 600 ℃. The black dot lines are modeled devices and the red solid lines are measured devices. From the top curve to the bottom curve, V_{GS} are 0, -2, -4, -6, -8 V, respectively.

3.8 Summary

The low voltage, normally on n-channel JFETs with raised gate configuration using 4H-SiC are fabricated and characterized with operational temperature up to 600 ℃. The threshold voltage at 25 ℃ is -6.81 with a high transconductance of 4.94 μS/μm and small on-resistance of 59.3 mΩ cm^2. As the temperature increases, the threshold voltage shifts with the rate of -1.38 mV/ ℃. Even at 600 ℃, the JFET still exhibits a transconductance of 0.79 μS/μm and an on/off drain saturation current ratio of 10^3. Hence, the SPICE DC fitting model agrees well with the measured data.

3.9 Reference

[1] W. R. Chang, Y. K. Fang, S. F. Ting, Y. S. Tsair, C. N. Chang, C. Y. Lin, and S. F. Chen, "The hetero-epitaxial SiCN/Si MSM photodetector for high-temperature deep-UV detecting applications," *IEEE Electron Device Letters,* vol. 24, pp. 565-567, Sep 2003.

[2] E. Monroy, F. Omnes, and F. Calle, "Wide-bandgap semiconductor ultraviolet photodetectors," *Semiconductor Science and Technology,* vol. 18, pp. R33-R51, Apr 2003.

[3] A. Vijayakumar, R. M. Todi, and K. B. Sundaram, "Amorphous-SiCBN-B ased metal-semiconductor-metal photodetector for high-temperature applications," *IEEE Electron Device Letters,* vol. 28, pp. 713-715, Aug 2007.

[4] W.-C. Lien, D.-S. Tsai, D.-H. Lien, D. G. Senesky, J.-H. He, and A. P. Pisano, "4H–SiC Metal–Semiconductor–Metal Ultraviolet Photodetectors in Operation of 450 ℃," 2012.

[5] P. G. Neudeck, S. L. Garverick, D. J. Spry, L. Y. Chen, G. M. Beheim, M. J. Krasowski, and M. Mehregany, "Extreme temperature 6H-SiC JFET integrated circuit technology," *Physica Status Solidi A,* vol. 206, pp. 2329-2345, Oct 2009.

[6] P. G. Neudeck, D. J. Spry, L.-Y. Chen, G. M. Beheim, R. S. Okojie, C. W. Chang, R. D. Meredith, T. L. Ferrier, L. J. Evans, and M. J. Krasowski, "Stable Electrical Operation of 6H–SiC JFETs and ICs for Thousands of Hours at 500," *IEEE Electron Device Letters,* vol. 29, pp. 456-459, 2008.

[7] D. Brown, E. Downey, M. Ghezzo, J. Kretchmer, V. Krishnamurthy, W. Hennessy, and G. Michon, "Silicon carbide MOSFET integrated circuit technology," *Physica Status Solidi A,* vol. 162, pp. 459-479, 1997.

[8] S.-H. Ryu, K. T. Kornegay, J. A. Cooper Jr, and M. R. Melloch, "Digital CMOS IC's in 6H-SiC operating on a 5-V power supply," *IEEE Transactions on Electron Devices,* vol. 45, pp. 45-53, 1998.

[9] D. Clark, E. P. Ramsay, A. Murphy, D. A. Smith, R. Thompson, R. Young, J. D. Cormack, C. Zhu, S. Finney, and J. Fletcher, "High temperature silicon carbide CMOS integrated circuits," in *Materials Science Forum*,2011, pp. 726-729.

[10] C.-W. Soong, A. C. Patil, S. L. Garverick, F. XIAOAN, and M. Mehregany, "550 C integrated logic circuits using 6H-SiC JFETs," *IEEE Electron Device Letters,* vol. 33, pp. 1369-1371, 2012.

[11] S. L. Garverick, C.-W. Soong, and M. Mehregany, "SiC JFET integrated circuits for sensing and control at temperatures up to 600° C," in *IEEE Energytech 2012,* 2012, pp. 1-6.

[12] L. Lanni, R. Ghandi, B. G. Malm, C. Zetterling, and M. Ostling, "Design and characterization of high-temperature ECL-based bipolar integrated circuits in 4H-SiC," *IEEE Transactions on Electron Devices,* vol. 59, pp. 1076-1083, 2012.

[13] M. Domeij, M. Ö stling, C. M. Zetterling, R. Ghandi, B. Buono, and B. G. Malm, "Current Gain Degradation in 4H-SiC Power BJTs," in *Materials Science Forum*, 2011, pp. 702-705.

[14] B. Ozpineci and L. Tolbert, "Smaller, faster, tougher," *IEEE Spectrum,* vol. 48, pp. 45-66, 2011.

[15] C.-M. Zetterling, *Process technology for silicon carbide devices*: IET, 2002.

[16] R. F. Pierret, *Semiconductor device fundamentals*: Pearson Education India, 1996.

[17] S. M. Sze and K. K. NG, *Physics of semiconductor devices*: Wiley, 2007.

[18] P. G. Neudeck, G. M. Beheim, and C. S. Salupo, "600 C Logic Gates Using Silicon Carbide JFET's," in *2000 Government Microcircuit Applications Conference, March*, 2000, pp. 20-23.

[19] M. Laube, F. Schmid, G. Pensl, G. Wagner, M. Linnarsson, and M. Maier, "Electrical activation of high concentrations of N^+ and P^+ ions implanted into 4H–SiC," *Journal of Applied Physics,* vol. 92, pp. 549-554, 2002.

[20] M. V. Rao, J. B. Tucker, M. Ridgway, O. Holland, N. Papanicolaou, and J. Mittereder, "Ion-implantation in bulk semi-insulating 4H–SiC," *Journal of Applied Physics,* vol. 86, pp. 752-758, 1999.

[21] S.-K. Lee, C.-M. Zetterling, M. Ö stling, J.-P. Palmquist, and U. Jansson, "Low resistivity ohmic contacts on 4H-silicon carbide for high power and high temperature device applications," *Microelectronic Engineering,* vol. 60, pp. 261-268, 2002.

[22] S. Lee, C.-M. Zetterling, and M. Ostling, "Titanium Tungsten (TiW) for Ohmic contacts to n-and p-type 4H-SiC," in *Materials Research Society Symposium Proceedings*, 2001, pp. H7. 2-H7. 2.

[23] C. Chang, Y. Fang, and S. Sze, "Specific contact resistance of metal-semiconductor barriers," *Solid-State Electronics,* vol. 14, pp. 541-550, 1971.

[24] A. B. Horsfall, N. G. Wright, H. K. Chan, J. P. Goss, and R. C. Stevens, "Reliability Evaluation of 4H-SiC JFETs Using IV Characteristics and Low Frequency Noise," in *Materials Science Forum*, 2013, pp. 934-937.

[25] A. C. Patil, "Silicon Carbide JFET Integrated Circuit Technology For High-Temoerature Sensors," Electrical Engineering and Computer Science, Case Western Reserve University, 2009.

[26] E. Luckowski, J. Delucca, J. Williams, S. Mohney, M. Bozack, T. Isaacs-Smith, and J. Crofton, "Improved ohmic contact to n-type 4H and 6H-SiC using nichrome," *Journal of Electronic Materials,* vol. 27, pp. 330-334, 1998.

[27] S.-K. Lee, C.-M. Zetterling, M. Östling, J.-P. Palmquist, H. Högberg, and U. Jansson, "Low resistivity ohmic titanium carbide contacts to n-and p-type 4H-silicon carbide," *Solid-State Electronics,* vol. 44, pp. 1179-1186, 2000.

[28] L. Fursin, J. Zhao, and M. Weiner, "Nickel ohmic contacts to p and n-type 4H-SiC," *Electronics Letters,* vol. 37, pp. 1092-1093, 2001.

[29] R. S. Okojie, L. J. Evans, D. Lukco, and J. P. Morris, "A Novel Tungsten–Nickel Alloy Ohmic Contact to SiC at 900," *IEEE Electron Device Letters,* vol. 31, pp. 791-793, 2010.

[30] S. Tsukimoto, T. Sakai, and M. Murakami, "Electrical properties and microstructure of ternary Ge/Ti/Al ohmic contacts to p-type 4H–SiC," *Journal of Applied Physics,* vol. 96, pp. 4976-4981, 2004.

[31] R. Kakanakov, L. Kassamakova, I. Kassamakov, K. Zekentes, and N. Kuznetsov, "Improved Al/Si ohmic contacts to p-type 4H-SiC," *Materials Science and Engineering: B,* vol. 80, pp. 374-377, 2001.

[32] F. Laariedh, M. Lazar, P. Cremillieu, J. Penuelas, J. Leclercq, and D. Planson, "The role of nickel and titanium in the formation of ohmic contacts on p-type 4H–SiC," *Semiconductor Science and Technology,* vol. 28, p. 045007, 2013.

[33] D. Planson, C. Raynaud, M. Lazar, D. Tournier, M. Soueidan, and D. M. Nguyen, "Process Optimization for High Temperature SiC Lateral Devices," in *Materials Science Forum*, 2009, pp. 585-588.

[34] V. Lauer, E. Niemann, S. Sheppard, and W. Wondrak, "High temperature performance of implanted-gate n-channel JFETs in 6H-SiC," in *Materials Science Forum*, 1997, pp. 1077-1080.

[35] T. Ayalew, "SiC Semiconductor Devices Technology, Modeling, and Simulation ", Technical University of Vienna, 2004.

[36] R. S. Okojie, D. Lukco, Y. L. Chen, and D. J. Spry, "Reliability assessment of Ti/TaSi 2/Pt ohmic contacts on SiC after 1000 h at 600 C," *Journal of Applied Physics,* vol. 91, pp. 6553-6559, 2002.

[37] A. A. Stephen E. Saddow, *Advances in Silicon Carbide Processing and Applications*, 2004.

[38] A. Maralani and M. S. Mazzola, "The design of an operational amplifier using silicon carbide JFETs," *IEEE Transactions on Circuits and Systems I: Regular Papers,* vol. 59, pp. 255-265, 2012.

[39] P. G. Neudeck, R. S. Okojie, and L.-Y. Chen, "High-temperature electronics-a role for wide bandgap semiconductors?," *Proceedings of the IEEE,* vol. 90, pp. 1065-1076, 2002.

[40] V. Cell and T. Videos, "State of the Art 3D SiC Process and Device Simulation."

[41] Q. Wahab, A. Ellison, A. Henry, E. Janzén, C. Hallin, J. Di Persio, and R. Martinez, "Influence of epitaxial growth and substrate-induced defects on the breakdown of 4H–SiC Schottky diodes," *Applied Physics Letters,* vol. 76, pp. 2725-2727, 2000.

[42] T. Kimoto, N. Miyamoto, and H. Matsunami, "Performance limiting surface defects in SiC epitaxial pn junction diodes," *, IEEE Transactions on Electron Devices* vol. 46, pp. 471-477, 1999.

[43] F. McLean, C. Tipton, J. McGarrity, and C. Scozzie, "Modeling the electrical characteristics of n-channel 6H–SiC junction-field-effect transistors as a function of temperature," *Journal of Applied Physics,* vol. 79, pp. 545-552, 1996.

[44] H. Daimon, M. Yamanaka, M. Shinohara, E. Sakuma, S. Misawa, K. Endo, and S. Yoshida, "Operation of Schottky-barrier field-effect transistors of 3C-SiC up to 400° C," *Applied Physics Letters,* vol. 51, pp. 2106-2108, 1987.

[45] S. Zappe, E. Obermeier, S. Sheppard, U. Schmid, V. Lauer, and W. Wondrak, "Advanced SPICE-modelling of 6H-SiC-JFETs including substrate effects," in *1998 Fourth International High Temperature Electronics Conference,* 1998, pp. 261-264.

[46] Y. Wang, C. J. Cass, T. P. Chow, F. Wang, and D. Boroyevich, "SPICE model of SiC JFETs for circuit simulations," in *Computers in Power Electronics, 2006. COMPEL'06. IEEE Workshops on*, 2006, pp. 212-215.

[47] R. Mousa, D. Planson, H. Morel, B. Allard, and C. Raynaud, "Modeling and high temperature characterization of SiC-JFET," in *IEEE Power Electronics Specialists Conference,* 2008, pp. 3111-3117.

Chapter 4

Silicon Carbide Complementary Buried Gate Junction Field-Effect Transistors

4.1 Introduction

CMOS is widely used for constructing integrated circuits, both digital logic and analog circuits. The advantages of using complementary devices are high noise immunity, larger bandwidth, and low power consumption [1, 2]. Certain applications, such as in-situ monitoring of fuel combustion, subsurface reservoirs (deep well drilling), and Venus and Jupiter surface exploration, require the electronics and their circuitry to work in the temperature range of 300-600 ℃ [3]. However, the operating temperature of Si CMOS devices, both bulk and silicon-on-insulator, is limited to 400 ℃ due to the more intrinsic carriers present than dopants carriers at this temperature [3-5]. Silicon carbide has become the candidate for these harsh environment electronics and circuitry because of its wide bandgap (3.2 eV for 4H-SiC), excellent chemical and thermal stability, and high breakdown electric field strength (5 MV/cm) [6]. However, much effort has been dedicated to the development of SiC n-channel transistors, and several reports show promising electrical properties of SiC n-channel devices, such as MOSFET [7], JFET [8] and BJT [9]. On the other hand, very few papers have reported SiC p-channel transistors. The reasons is that the hole mobility of SiC is more than eight times smaller than electron mobility [10] and the thermal activation energy of p-type dopants is higher than n-type dopants [11]. While SiC MOSFET suffers from the low inversion mobility and gate oxide reliability issues limiting the operating temperature up to 400 ℃ [12-14], majority-carrier JFET seems to be a promising candidate for complementary transistors.

In this chapter, we first propose the fabrication process of 4H-SiC complementary JFETs (c-JFETs). Despite the lack of success with an of the n-channel buried gate JFET (n-JFET), we have developed the first prototype of the low voltage, p-channel buried gate JFET (p-JFET) using 4H-SiC and characterize the electrical properties from room temperature up to 600 ℃ in air.

4.2 Design of Complementary Buried Gate JFET

To design and optimize the performance of the complementary device, Sentaurus TCAD structure editor was used to build the two-dimensional device structure of 4H-SiC as shown in Figure 4.1. The JFET has a gate length of 10 μm and the source/drain width of 100 μm. The distance between the edge of the gate and the edge of the source/drain is 5 μm.

Figure 4.1: Buried gate JFET structure generated by the Sentaurus structure editor.

A previous study shows that the V_T is most sensitive to the depth of the channel and gate, and doping concentration of the channel [15]. To reduce the number steps in the lithography process, the depth of the p^+ gate of n-JFET and the depth of the p^+ source/drain p-JFET are fixed with the same value of 50 nm, as in the n^+ case. Therefore, the simulation focuses mainly on the effects of the channel depth and doping concentration for both p- and n-JFETs. Figures 4.2 and 4.3 show examples of effects of the channel depth and doping concentration to both n- and p-JFETs with L = 8 μm at room temperature. In order to achieve the low power, complementary JFET circuitry, the threshold voltage of p- (V_{Tp}) and n-JFET (V_{Tn}) and the saturation current of p- ($I_{Dsat,p}$) and n-JFET ($I_{Dsat,n}$) should match with one another. The goal of the optimization of the parameters is as follows:

(1) $|V_{Tp}| = |V_{Tn}| = \sim 5$ V
(2) $|I_{Dsat,p}| = |I_{Dsat,n}| = \sim 10^{-5}$ -10^{-6} A

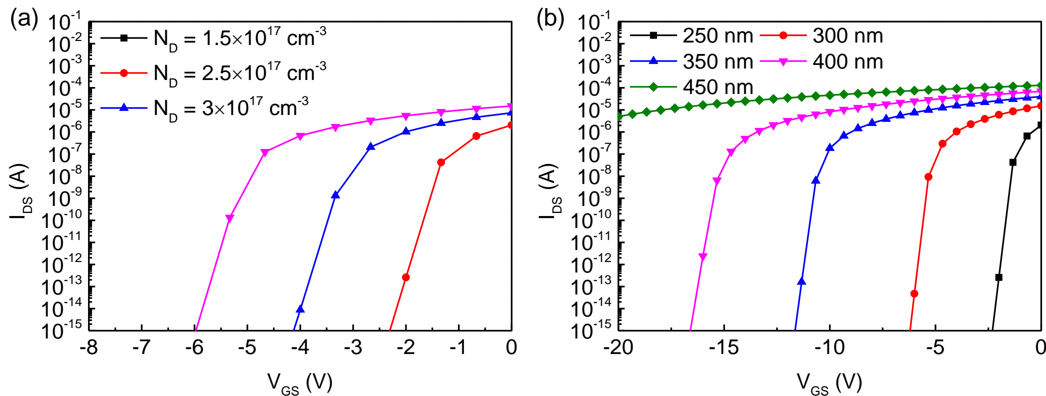

Figure 4.2: Simulated I_{DS}-V_{GS} of n-channel JFETs with L = 8 μm and (a) different channel doping with fixed channel depth of 250 nm (b) different channel depth with fixed channel doping of 2.5×10^{17} cm^{-3} at 25 ℃.

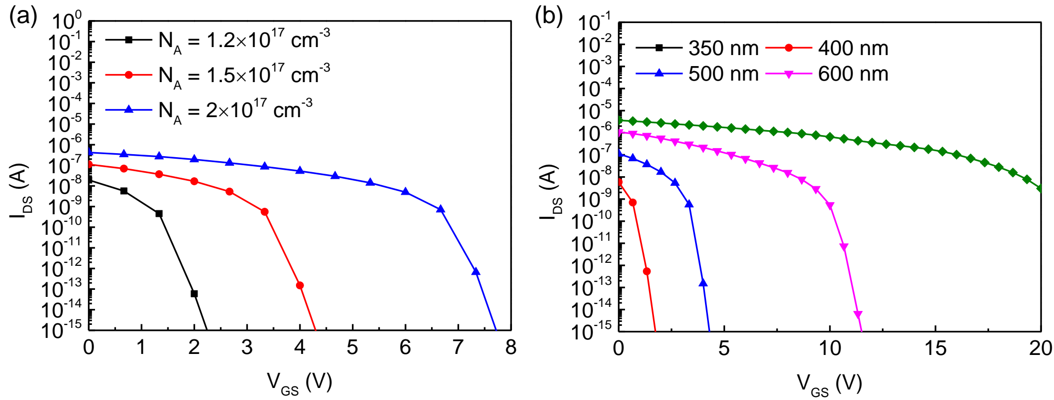

Figure 4.3: Simulated I_{DS}-V_{GS} of p-channel JFETs with L = 8 μm and (a) different channel doping with fixed channel depth of 400 nm (b) different channel depth with fixed channel doping of 1.5×10^{17} cm^{-3} at 25 °C.

Based on the simulation results, it is not easy to achieve the same intensity of saturation current with the same intensity of threshold voltage for both p- and n-JFET due to the smaller hole mobility compared with the electron mobility of 4H-SiC. The strategy of the optimization is to have similar voltage for both devices and a larger width of source/drain area or multi-finger gates of p-JFET. Figure 4.4 and Table 4.1 show and summarize the optimized I_{DS}-V_{GS} curves and parameters of complementary JFETs for gate length of 8 μm.

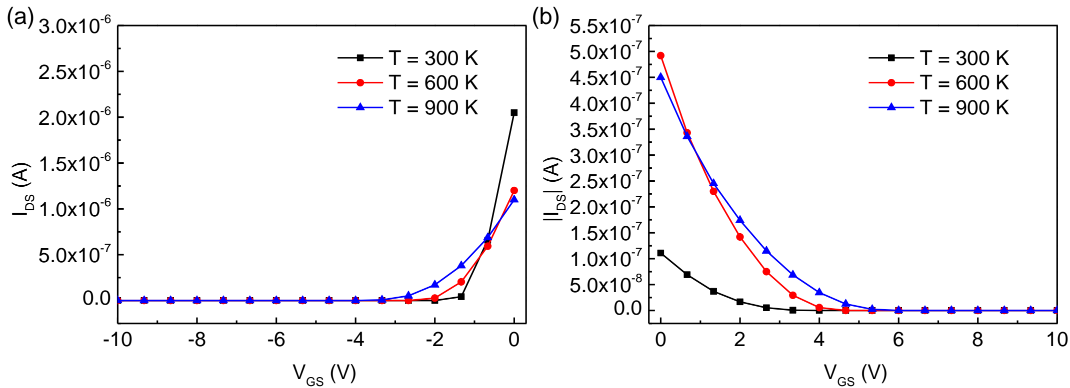

Figure 4.4: Simulated I_{DS}-V_{GS} of a (a) n-channel (b) p-channel JFET with L = 8 μm.

Device type	Temperature (℃)	V_T (V)	g_m (μS/μm)	r_o (Ω)
n	25	-1.3	3.15	4.08×10^8
n	600	-2.3	0.957	8.81×10^8
p	25	2	0.111	8.29×10^8
p	600	3.5	0.257	3.30×10^8

Table 4.1: Optimized parameters of complementary JFETs with L = 10 μm. g_m, r_o, and $g_m r_o$ is based on V_{GS} = 0 V.

Note that the saturation current of p-JFET increases from 25 ℃ to 327 ℃ and then decreases from 327 ℃ to 627 ℃. Unlike the case of the 4H-SiC n-channel JFET where I_{DS} and g_m decrease as temperature increases, these trends of 4H-SiC p-channel JFET acting in an opposite direction can be attributed to the effect of carrier mobility and degree of ionization with elevated temperature. The saturation current will increase by increasing the carrier mobility and ionized carrier concentration as shown in the conventional 3/2 power model [16]. The electron and hole mobility, μ_n and μ_p, at low electric field could be calculated using Caughey-Thomas equation given by [17]

$$\mu_{n,p} = \mu_{n,p}^{min} + \frac{\mu_{n,p}^{max} - \mu_{n,p}^{min}}{1+(\frac{N_D+N_A}{N_{n,p}^{\mu}})^{\alpha_{n,p}}} \tag{4.1}$$

$$\mu_{n,p}^{min} = \mu_{n,p(300K)}^{min}(\frac{T}{300K})^{\beta_{n,p}} \tag{4.2}$$

$$\mu_{n,p}^{max} = \mu_{n,p(300K)}^{max}(\frac{T}{300K})^{\gamma_{n,p}} \tag{4.3}$$

where N_D and N_A are the doping concentration of the dopants and acceptors, which are 2.5×10^{17} cm^{-3} and 2.5×10^{17} cm^{-3}, respectively. The $\mu_{n,p}^{max}$ is the mobility of unintentionally doped 4H-SiC, where the lattice scattering is the main scattering mechanism. The $\mu_{n,p}^{min}$ is the mobility of heavily doped 4H-SiC, where the dominant mechanism is impurity scattering. The values of $\mu_{n,p}^{max}$ and $\mu_{n,p}^{min}$ at 300 K are $\mu_{n,p(300K)}^{max}$ and $\mu_{n,p(300K)}^{min}$, respectively. $N_{n,p}^{ref}$ is the doping concentration at which the mobility is half of the sum of $\mu_{n,p}^{max}$ and $\mu_{n,p}^{min}$. $\alpha_{n,p}^{\mu}$ denotes how fast the mobility changes from $\mu_{n,p}^{min}$ to $\mu_{n,p}^{max}$, $\beta_{n,p}^{\mu}$ is the constant temperature coefficient, and $\gamma_{n,p}^{\mu}$ describes how mobility of undoped 4H-SiC changes due to lattice scattering. All the parameters except N_D and N_A are the fitting parameters and are listed in the Table 4.2 [17].

Doping type	$\mu_{n,p(300K)}^{min}$ (cm^2/Vs)	$\mu_{n,p(300K)}^{max}$ (cm^2/Vs)	$N_{n,p}^{ref}$ (cm^{-3})	$\alpha_{n,p}^{\mu}$	$\beta_{n,p}^{\mu}$	$\gamma_{n,p}^{\mu}$
n	40	950	1.94×10^{17}	0.61	-0.5	-2.40
P	15.9	125	1.76×10^{19}	0.34	-0.5	-2.15

Table 4.2: Fitting parameters for low field mobility of 4H-SiC.

Figure 4.5 (a) shows the temperature dependence of the carrier mobility. The electron mobility decreases from ~526 cm^2/Vs at 300 K to ~294 cm^2/Vs at 900 K for n-type 4H-SiC, and the hole mobility decreases from ~102 cm^2/Vs at 300 K to ~11 cm^2/Vs at 900 K for p-type 4H-SiC. Both electron and hole mobility decrease as temperature increases. Therefore, a certain portion of saturation current is reduced due to the decreases of the carrier mobility. Note that the hole mobility is smaller than electron mobility, which leads to lower transconductance is p-channel JFET. On the other hand, most of the common dopants in 4H-SiC, which are nitrogen and phosphorus for n-type, and boron and aluminum for p-type, have activation energies larger than the thermal energy at room temperature [18]. This leads the incomplete ionization of these dopants and strong temperature and frequency dependence of junction differential admittance [19]. The degree of ionization could be calculated as follows [17]

$$I_n = \frac{N_D^+}{N_D} = \frac{-1+\sqrt{1+2g_D\frac{N_D}{N_C}\exp(\frac{\Delta E_{Dh}}{k_BT})}}{2g_D\frac{N_D}{N_C}\exp(\frac{\Delta E_{Dh}}{k_BT})} + \frac{-1+\sqrt{1+2g_D\frac{N_D}{N_C}\exp(\frac{\Delta E_{Dk}}{k_BT})}}{2g_D\frac{N_D}{N_C}\exp(\frac{\Delta E_{Dk}}{k_BT})} \tag{4.4}$$

$$I_p = \frac{N_A^-}{N_A} = \frac{-1+\sqrt{1+4g_A\frac{N_A}{N_V}\exp(\frac{\Delta E_A}{k_BT})}}{2g_A\frac{N_A}{N_V}\exp(\frac{\Delta E_A}{k_BT})} \tag{4.5}$$

where I_n and I_p are degree of ionization for nitrogen and aluminum, respectively, N_D^+ and N_A^+ are concentration of ionized donors and acceptors, respectively, g_D and g_A are degeneracy factor with value of 2 and 4, respectively, N_C and N_V are effective density of states of the conduction band and valence band, respectively, ΔE_{Dh}, ΔE_{Dk} and ΔE_A are ionization energy of nitrogen on hexagonal site, nitrogen on cubic site and aluminum, respectively, k_B is Boltzmann and T is temperature. The estimated degrees of ionization of electron and hole are shown in Figure 4.5 (b). The electrons in 4H-SiC already have 82 % of ionization at 25 ℃, and they reach nearly 100% ionization at 600 ℃. For n-channel JFET, such a small increase of degree of ionization cannot counterbalance the decrease of saturation current caused by the electron mobility degradation. However, the holes in 4H-SiC only have 11% ionization at 25 ℃, but they reach 93% ionization at 600 ℃, because the acceptor level of aluminum is relatively deeper (ΔE_A = 200 meV) than nitrogen (ΔE_{Dh} = 50 meV and ΔE_{Dk} = 92 meV) in 4H-SiC. The significant amount activation of aluminum acceptors in 4H-SiC accounts for increase of the saturation current at higher temperature.

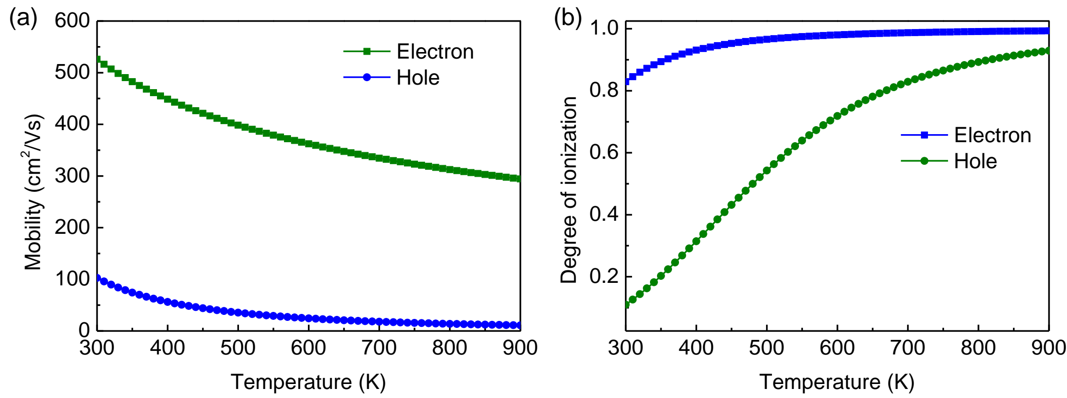

Figure 4.5: Temperature dependence of (a) carrier mobility and (b) degree of ionization.

4.3 Fabrication Process

Figure 4.6 is a cross-sectional schematic of the lateral 4H-SiC complementary JFETs used in this work. The transistor consists of n-type 4H-SiC wafer (from SiCrystal AG) with four epitaxial layers (from Ascatron AB). A 5 µm p^- epitaxial layer with doping concentration of 2×10^{15} cm^{-3}, followed by 250 nm n epitaxial layer with doping concentration of 1×10^{19} cm^{-3}, a 400 nm p^+ epitaxial layer with doping concentration of 1.5×10^{17} cm^{-3}, and a 250 nm n^+ epitaxial layer with doping concentration of 2.5×10^{17} cm^{-3} were grown on the substrate. Figure 4.7 presents the entire fabrication process flow including eight lithography masks. First, the device area of n-JFET is time etched using TCP etcher with 90 sccm Cl_2 and 10 sccm BCl_3 under RF bias of 150 W. Secondly, the device area of p-JFET is also time etched using TCP etcher with 90 sccm Cl_2 and 10 sccm BCl_3 under RF bias of 150 W. 1 µm PECVD SiO_2 was patterned to define the source/drain area of n-JFET and gate area of p-JFET with ion implantation to form n^+ box profile at 600 °C. Unlike using nitrogen for the ion implanted n^+ region of n-channel raised gate JFET, as discussed in Chapter 3, phosphorous was used for ion implantation. The nitrogen forms a donor state when substituting for carbon in the SiC lattice while phosphorous form a donor state on substituting Si sites [20]. The phosphorous implanted n^+ region can reach above 10^{20} cm^{-3} while nitrogen implanted one will saturate at 2 to 3×10^{19} cm^{-3} due to the limitation of solubility of nitrogen and formation of nitrogen-related precipitates [21, 22]. The phosphorous implantation in this work used 1.5×10^{15} does at 5 keV. The phosphorous doping concentration and distribution determined from TCAD simulation are presented in Figure 4.8. The oxide masks were then removed by buffer oxide etching solution (hydrofluoric acid). 1 µm PECVD SiO_2 was patterned to define the gate area of n-JFET and source/drain area of p-JFET with aluminum implantation at 600 °C. The implantation of a box profile was formed using 1×10^{15} and 1×10^{15} doses at 5 and 7 keV energies, respectively. The phosphorous doping concentration and distribution determined TCAD simulation are presented in Figure 4.9. After ion implantation, oxide layers were removed by buffer oxide etching solution. The implanted dopants were electrically activated by annealing samples capped with 2 µm PECVD SiO_2 at 1550 °C under Argon atmosphere for 15 minutes [23]. Figure 4.10 is the

SEM image of the 4H-SiC after annealing, and there are some etching pits present on the surface. Better capping technology such as graphite or extra SiC resource is required for the future fabrication [21, 24]. A mesa etch was then used to define the device area and expose the base region of p-JFET using TCP etcher. The JFET surface was then passivated with PECVD SiO_2 and the 25 nm Ni, 45 nm Ti, 95 nm Al and 50 nm TiW (10% Ti, 90% W) contact was deposited and patterned via lift-off to form the contact electrodes. The metal contacts were annealed via rapid thermal annealing (RTA) at 800 ℃ for 2 minute under Ar ambient. 200 nm TiW (10% Ti, 90% W) was used for the 1st level of metal interconnects. Finally, the 20 nm Cr and 180 nm Pt was used for 2nd level of metal interconnect.

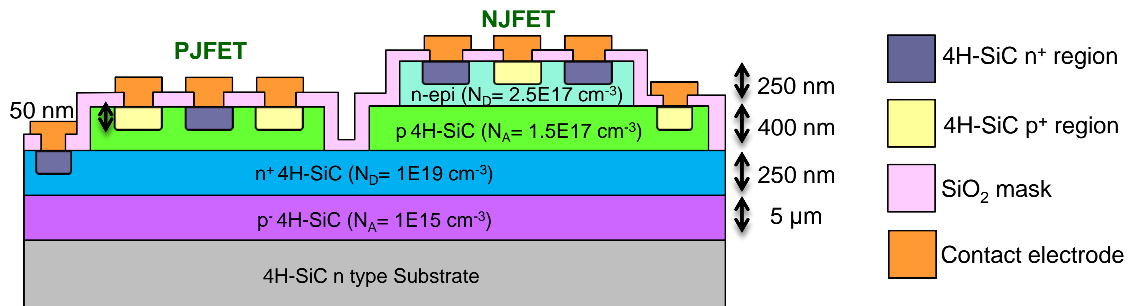

Figure 4.6: Schematic of 4H-SiC complementary JFETs.

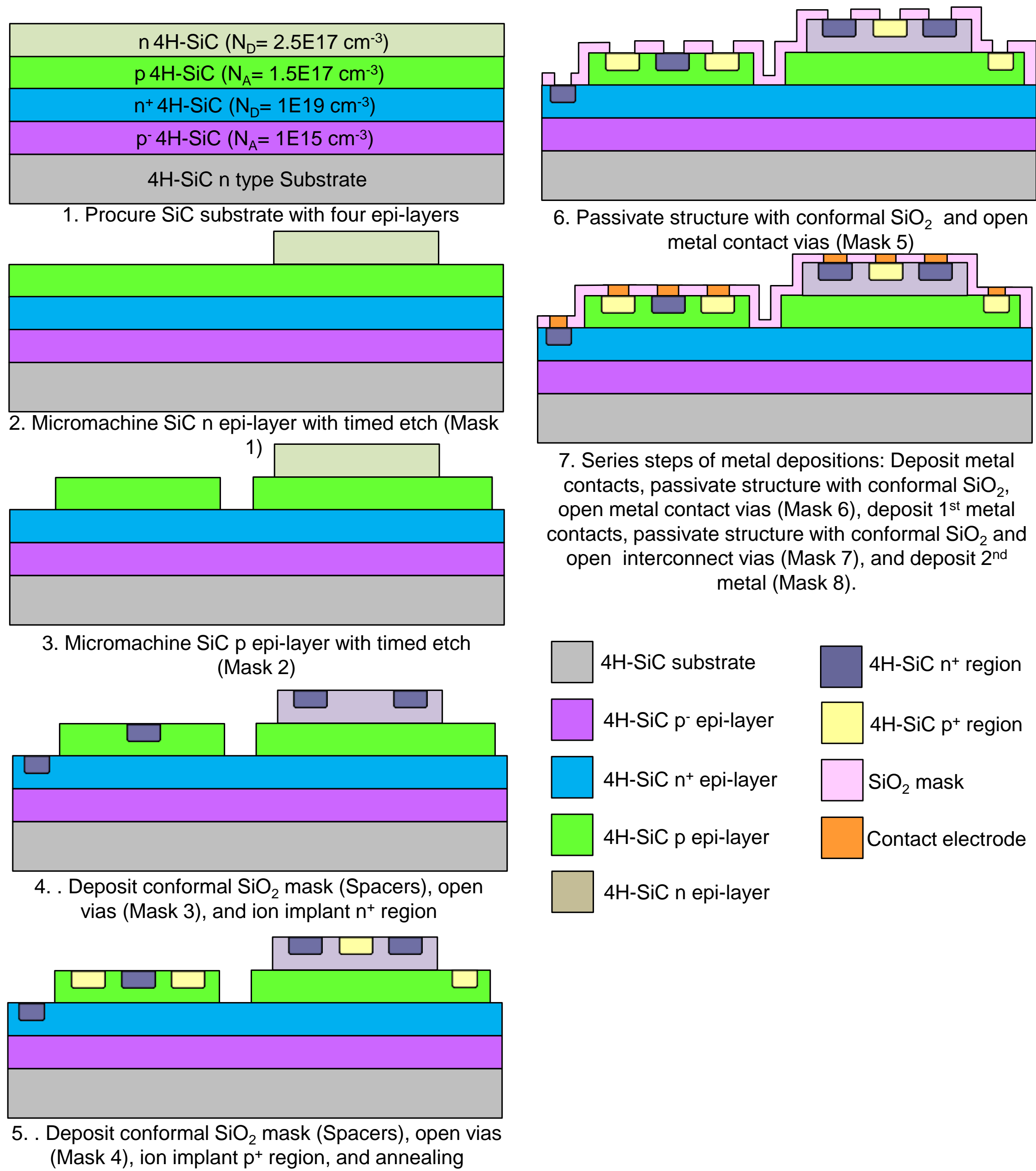

Figure 4.7: Completed fabrication process flow of 4H-SiC c-JFETs.

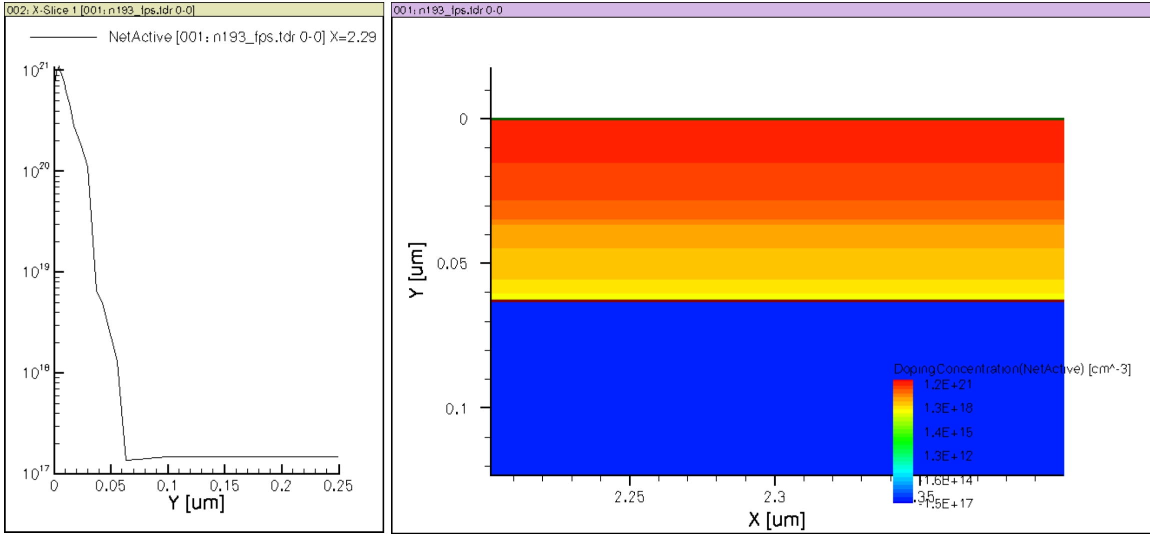

Figure 4.8: Simulated phosphorous doping profile in the p-channel area with $N_A = 1.5\times10^{17}$ cm^{-3}.

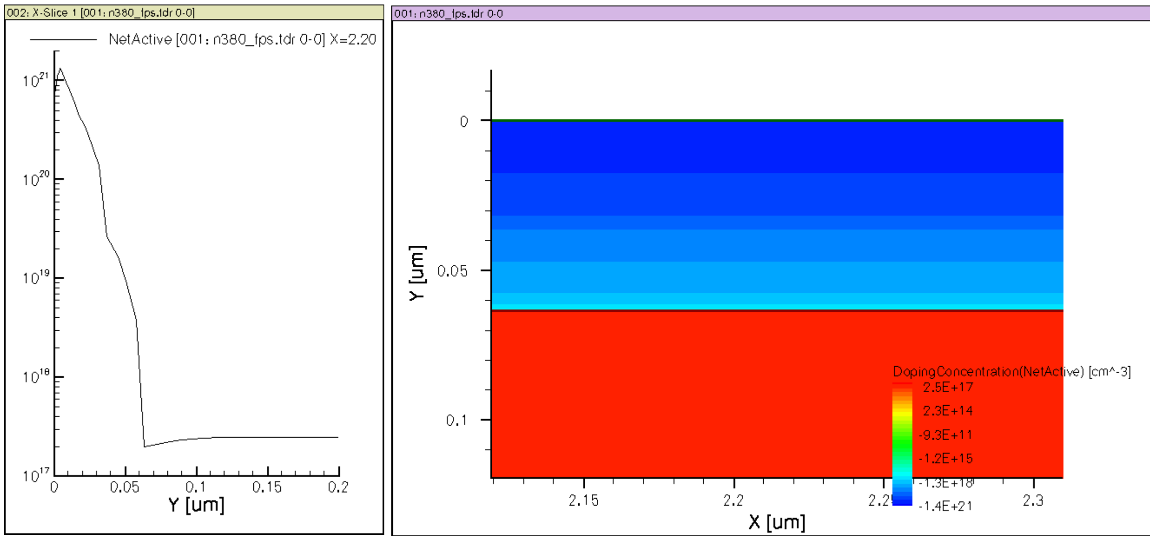

Figure 4.9: Simulated aluminum doping profile in the n-channel area with $N_D = 2.5\times10^{17}$ cm^{-3}.

Devices were characterized on a hot chuck of high temperature probe station (Signatone Inc.). This high temperature probe station consists of ceramic hot chunk, thermal heater and water cooler and the chunk temperature goes up to 600 ℃ with low thermal noise of 10^{-9}-10^{-8} A at 600 ℃. An Agilent B2912A precision source/measurement unit and with tungsten probe tips was used to measure the I-V characteristics of the devices.

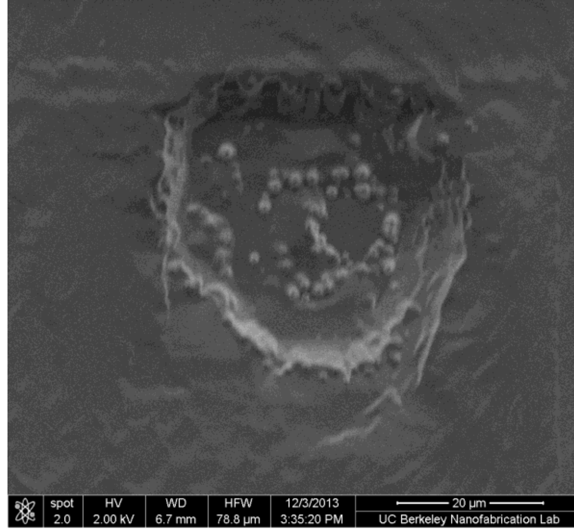

Figure 4.10: SEM image of etching pits after thermal annealing at 1550 ℃ for 15 minute.

4.4 Metallization of Complementary Buried Gate JFET

Figure 4.11 shows the *I-V* measurement of Ni/Ti/Al/TiW metal stacks and n-type 4H-SiC for TLM structure. The contact is originally Ohmic with large resistance before RTA and the resistance decreases after the RTA. This is possible because the doping concentration of phosphorous in 4H-SiC achieves more than 10^{20} cm^{-3} and a high degree of ionization even at room temperature, as shown in Figure 4.8. The temperature dependences of measured ρ_c are shown in Figure 4.12, and the value of ρ_c is on the order of 10^{-5} Ω cm^2 up to 550 ℃, indicating a stable metal contact is formed after RTA. The monotonic increase of the specific contact resistance with temperature is due to the increases of the tunneling effective mass of carriers at a high doping range of 10^{20}-10^{21} cm^{-3} [25]. Typically, a smaller tunneling effective mass has a smaller ρ_c value. Possible instability or oxidation might be responsible for the sudden increase of ρ_c to 3.383×10^{-4} Ω cm^2 at 600 ℃. The fitted ρ_c and R_{sh} are listed in Table 4.3.

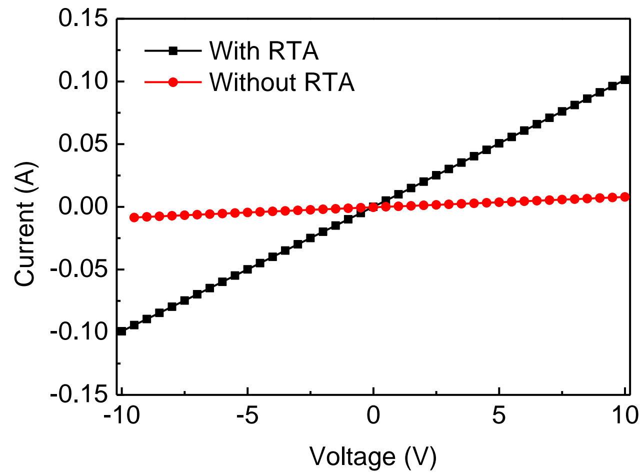

Figure 4.11: Measure I-V curves of metal and n-type 4H-SiC before and after RTA annealing for TLM structure with d = 5 μm.

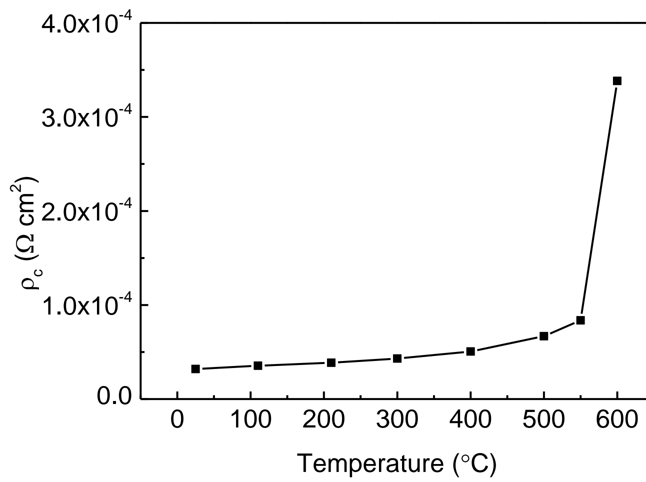

Figure 4.12: Temperature dependences of specific contact resistance of Ni/Ti/Al/TiW metal stacks to n^+ 4H-SiC.

Temperature (℃)	R_{sh} (kΩ/□)	ρ_c (Ω cm^2)
25	1.324	3.20×10^{-5}
110	1.381	3.54×10^{-5}
210	1.480	3.86×10^{-5}
300	1.566	4.31×10^{-5}
400	1.686	5.06×10^{-5}
500	1.678	6.68×10^{-5}
550	1.745	8.37×10^{-5}
600	1.586	3.383×10^{-4}

Table 4.3: Sheet resistance and specific contact resistance of Ni/Ti/Al/TiW metal stacks and n-type 4H-SiC at different temperatures.

The *I-V* measurement of Ni/Ti/Al/TiW metal stacks and n-type 4H-SiC for TLM structure is shown in Figure 4.13. The contact is Schottky contact before RTA and it becomes Ohmic after the RTA. The temperature dependencies of measured ρ_c are shown in Figure 4.14, and the value of ρ_c is on the order of 10^{-3} Ω cm^2 which is higher than the n-type case. Although the p-type doping concentration should reach more than 10^{20} cm^{-3} after aluminum ion implantation based on the TCAD simulation (Figure 4.9), specific contact resistance decreased with temperature up to 550 ℃ due to the higher degree of ionization and the current density at elevated temperature. Again, the sudden change of ρ_c value at 600 C implies a possible oxidation mechanism or the metal instability. Table 4.4 summarizes the value of R_{sh} and ρ_c. The R_{sh} is at least one order of magnitude higher than for the n-type case due to the low hole mobility and less degree of ionization.

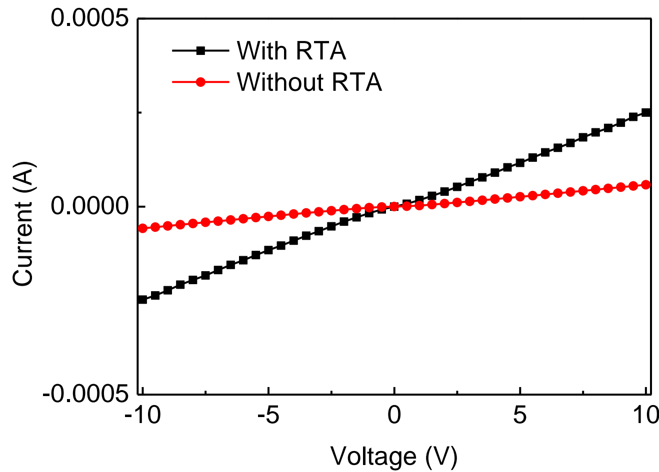

Figure 4.13: Measure I-V curves of metal and p-type 4H-SiC before and after RTA annealing for TLM structure with d = 20 µm.

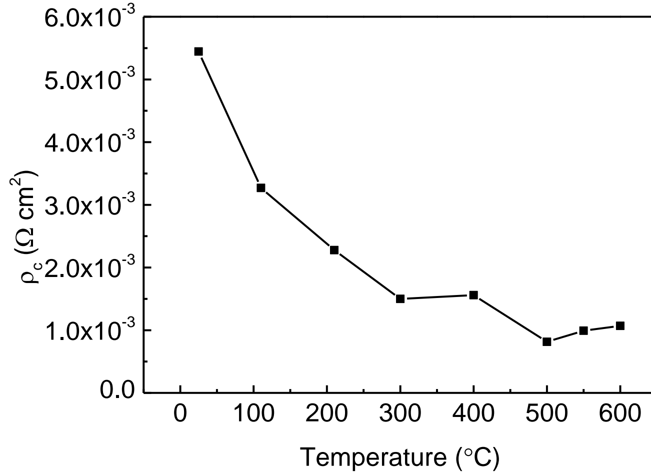

Figure 4.14: Temperature dependences of specific contact resistance of Ni/Ti/Al/TiW metal stacks to p^+ 4H-SiC.

Temperature (°C)	R_{sh} (kΩ/□)	ρ_c (Ω cm^2)
25	170	5.45×10^{-3}
110	99.2	3.27×10^{-3}
210	62.7	2.28×10^{-3}
300	48.3	1.50×10^{-3}
400	38.9	1.56×10^{-3}
500	37.5	8.14×10^{-4}
550	35.1	9.92×10^{-4}
600	33.3	1.07×10^{-3}

Table 4.4: Sheet resistance and specific contact resistance of Ni/Ti/Al/TiW metal stacks and p-type 4H-SiC at different temperatures.

4.5 Electrical Properties of N-Channel Buried Gate JFET

Figure 4.15 shows the optical image of as-fabricated n-channel buried gate 4H-SiC JFET with L = 10 μm and W = 100 μm. Figure 4.16 shows the I_{DS}-V_{DS} characteristics of a 100 μm /10 μm JFET at room temperature. The device exhibits resistor-like behavior with a very small output resistance at V_{GS} = 0 V. Furthermore, the device cannot completely turn off by applying a gate bias from 0 V to -10 V which means the JFET is not fully functional. By inspecting the I-V curve between p+ gate and n channel as shown in Figure 4.17, the built-in voltage is approximately 2.9 V which is similar to the

theoretical value of 3.11 V. However, as the intensity of drain current did not change with the gate bias, the possible failure point might be the unsuccessful fabrication of the p^+ gate. More characterization techniques such as cross-sectional TEM and secondary ion mass spectrometry (SIMS) analysis are necessary to verify the doping distribution and concentration of p^+ gate.

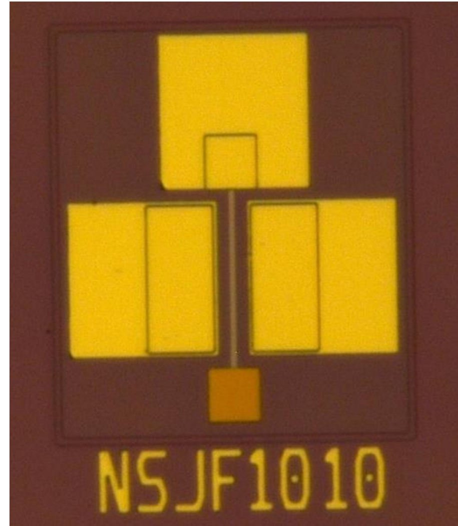

Figure 4.15: Optical image of a n-channel buried gate 4H-SiC JFET with L = 10 μm and W = 100 μm.

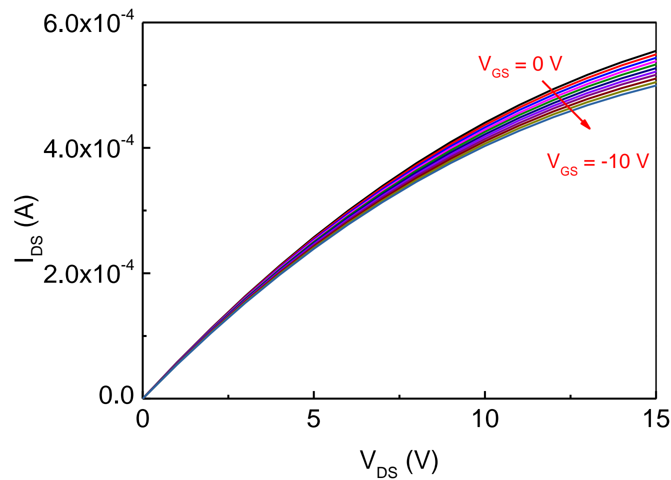

Figure 4.16: I_{DS}-V_{DS} characteristics of a n-channel buried gate 4H-SiC JFET under different V_{GS} and with W/L= 100 μm/10 μm at 25 °C.

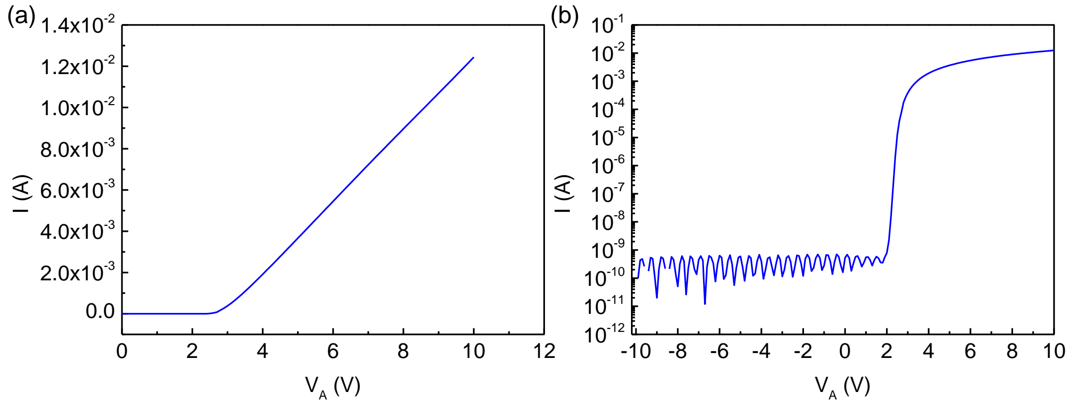

Figure 4.17: I-V characteristics of pn junction in the n-channel buried gate 4H-SiC JFET structure.

4.6 Electrical Properties of P-Channel Buried Gate JFET

4.6.1 Characterization of P-Channel Buried Gate JFET at Room Temperature

Figure 4.18 shows the optical images of as-fabricated p-channel 4H-SiC JFET with L equal to 10 μm and W equals to 100 μm. The p-channel thickness is approximately 370 nm which is slightly different than the target thickness of 400 nm due to the imprecise control of etching time. Figure 4.19 shows the drain current ($|I_{DS}|$) versus V_{DS} characteristics of a 100 μm /10 μm JFET at room temperature. The characteristic curves clearly show the linear and saturation regions. The device is a depletion mode JFET which is fully-on at V_{GS} = 0 V and is cut-off at V_{GS} = 5 V. Figure 4.20 (a) is the $|I_{DS}|$ versus V_{GS} characteristics at V_{DS} = 20 V, and the p-channel reaches pinch-off state approximately at 5 V. Figure 4.20 (b) represents the more precise threshold voltage which is extracted from the extrapolated intercept of x axis of $\sqrt{\frac{|I_{DS}|}{1+\lambda V_{DS}}}$ vs. V_{GS} plot at V_{DS} = 20 V. The threshold voltage is approximately 4.39 V. The calculated g_m of 4H-SiC p-channel JFET is 0.009 μS/μm at room temperature. Here the transconductance is calculated by normalizing with the channel width of 100 μm. The estimated r_o and λ are 2.36×10^{8} Ω and 2.28×10^{-3} V^{-1}, respectively. The intrinsic gain of single 4H-SiC p-channel JFET is approximately 46.3 dB at V_{GS} = 0 V and 25 °C.

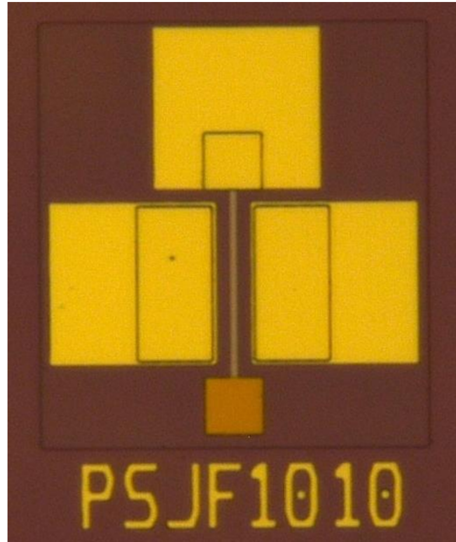

Figure 4.18: Optical image of a p-channel buried gate 4H-SiC JFET with $L = 10$ μm and $W = 100$ μm.

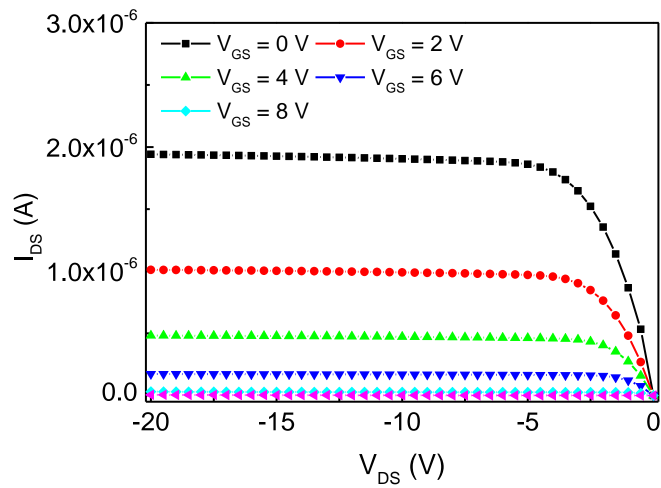

Figure 4.19: $|I_{DS}|$-V_{DS} characteristics of a p-channel 4H-SiC JFET under different V_{GS} and with W/L= 100 μm/10 μm at 25 °C.

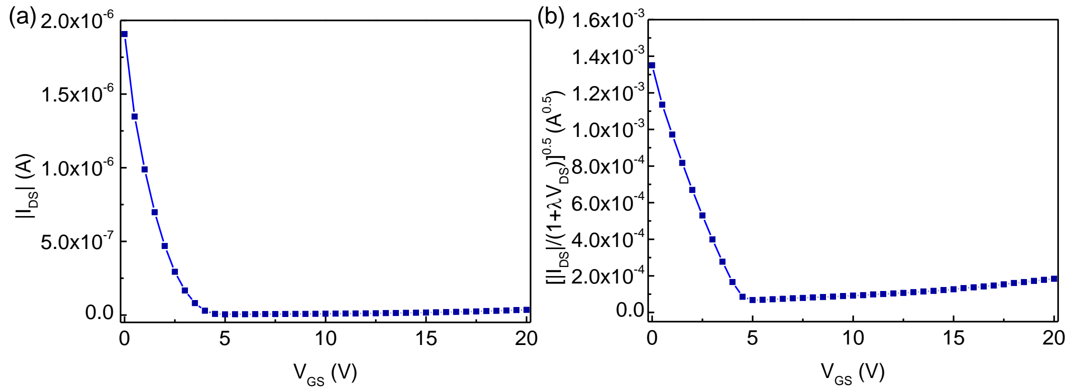

Figure 4.20: (a) $/I_{DS}|$-V_{GS} (b) $\sqrt{|I_{DS}|}$-V_{GS} characteristics of a p-channel 4H-SiC JFET with W/L= 100 µm/10 µm and V_{DS} = -20 V at 25 ℃.

4.6.2 Characterization of P-Channel Raised Gate JFET at High Temperature

Figure 4.21 (a)-(g) shows the $|I_{DS}|$ verses V_{DS} characteristics of a 100 µm /10 µm p-channel JFET from 110 to 600 ℃. The device can be turned on and off by applying different gate voltage for the entire temperature range. Figure 4.21 (h) shows the I_{DS}-V_{DS} curves at V_{GS} = 0 V and at incremental temperatures up to 600 ℃. The intensity of the saturation current at V_{GS} = 0 V increases as the temperature increases, but this rate decreases at 400℃. The activation of aluminum acceptors in 4H-SiC accounts for this increase of the saturation current and decreases of R_{on} described in Section 4.2. Due to the relatively deep acceptor level of aluminum (ΔE_A = 200 meV), higher current is induced at elevated temperatures.

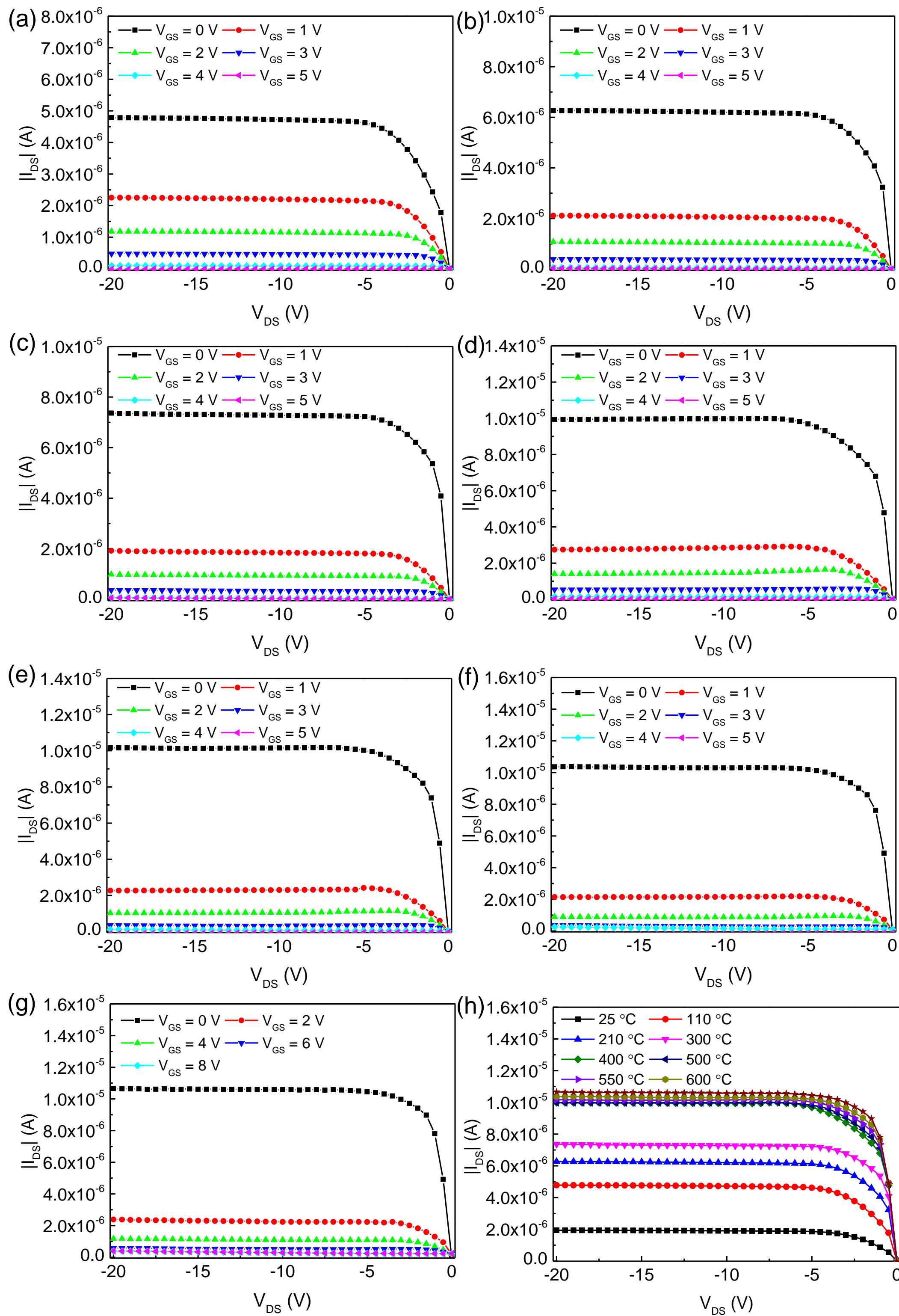

Figure 4.21: I_{DS}-V_{DS} characteristics of a p-channel 4H-SiC JFET under different V_{GS} and with W/L= 100 μm/10 μm (a) at 110 ℃ (b) at 210 ℃ (c) at 300 ℃ (d) at 400 ℃ (e) at 500 ℃ (f) at 550 ℃ (g) at 600 ℃. (h) Temperature dependences of I_{Dsat} of a p-channel 4H-SiC JFET at V_{GS} = 0 V and with W/L= 100 μm/10 μm.

However, there are some non-ideal behaviors of the device when increasing the operating temperature. Figure 4.22 shows the I_{DS}-V_{GS} curves under a drain-to-source -20 V bias and at incremental temperatures up to 600 ℃. The saturation currents exhibit a kink effect around V_{GS} of 0 to 0.5 V at temperature greater than 25 ℃, and the I_{Dsat} at V_{GS} < 0 has the a smaller degree of increase or remains roughly the same when increasing the temperature, unlike the I_{Dsat} at V_{GS} = 0 V. The whole JFET can be divided into many 2D JFETs, and the whole saturation current is the superposition of the current from these 2D transistors. Therefore, if these devices exhibit different threshold voltages, then they will have different saturation current for same V_{GS}. A clear definition of gate area with uniform doping is more difficult to achieve if the gate is ion implanted rather than mesa etched on the epitaxial layers due to the 4-degree-off SiC wafer and thin film which might contribute the kink effect of saturation current in the I_{DS}-V_{GS} curves.

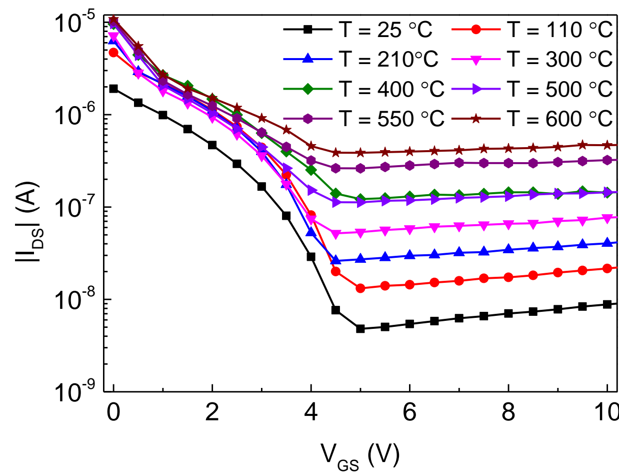

Figure 4.22: $|I_{DS}|$-V_{GS} characteristics of a p-channel 4H-SiC JFET under V_{DS} = -20 V and with W/L= 100 μm/10 μm at different temperatures.

The threshold voltages increased from 4.39 V at 25 ℃ to 5.71 V at 600 ℃, respectively, and are approximately shifted with a rate of +2.1 mV/ ℃, as shown in Figure 4.23. The temperature dependencies of the estimated transconductance and the intrinsic gain of the p-channel JFET at V_{GS} = 0 V are shown in Figure 4.24. Compared with the transconductance value of room temperature, the transconductance at V_{GS} = 0 V and 600 °C is increased to 0.037 μS/μm leading to intrinsic gain increases of 55.4 dB. The intrinsic gain of the JFET does not have monotonic temperature dependence but the overall tendency is to decrease with increasing temperature. The complete electrical properties of n-channel raised gate 4H-SiC JFET are listed and summarized in Table 4.5. Compared with the performance of the n-channel raised gate JFET described in Chapter 3, the p-channel buried gate JFET has a small g_m and I_{Dsat}/I_{off} and the R_{on} is quite large. The g_m of n-channel JFET is 500 times higher than the p-channel device at 25 and reduces to 20 times at 600 ℃ owing to the increased degree of ionization of holes. For the amplifier application, the saturation current could be matched by carefully designing the device geometry. Besides, it seems that the raised gate which used in-situ doping

during the epitaxial films growth yield better quality than ion-implanted gate [26].

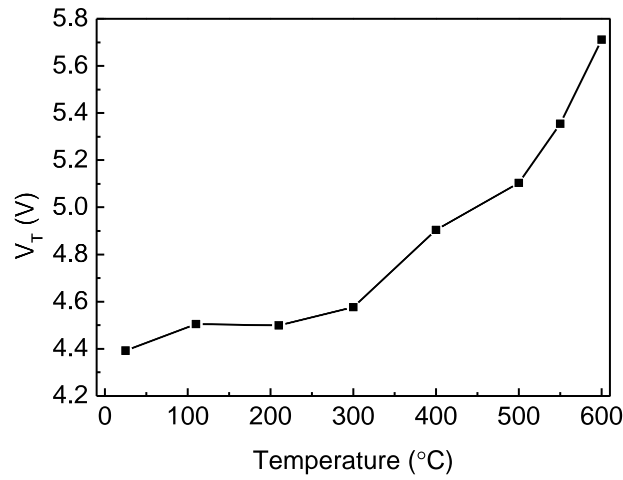

Figure 4.23: Temperature dependence of threshold voltage of a p-channel 4H-SiC JFET with *W*/*L*= 100 μm/10 μm.

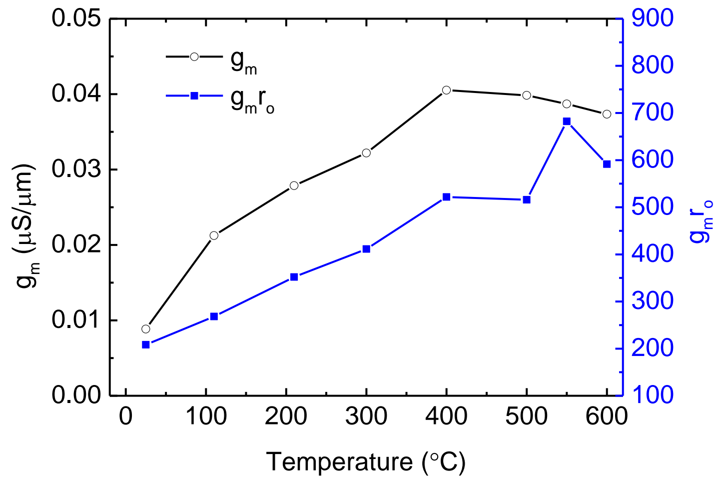

Figure 4.24: Temperature dependence of transconductance and intrinsic gain of of a p-channel 4H-SiC JFET with *W*/*L*= 100 μm/10 μm.

Temperature (℃)	$V_T(V)$	g_m ($\mu S/\mu m$)	R_{on} (Ω cm^2)	r_o (Ω)	λ (mV^{-1})	$g_m r_o$	I_{Dsat}/I_{off}
25	4.39	0.009	21.8	2.36×10^8	2.28	208.3	305
110	4.50	0.021	7.5	1.26×10^8	1.71	268.2	296
210	4.50	0.028	4.4	1.26×10^8	1.29	351.8	196
300	4.58	0.032	3.4	1.28×10^8	1.09	411.4	114
400	4.90	0.041	2.7	1.29×10^8	7.83	521.8	71
500	5.10	0.040	2.5	1.30×10^8	7.71	516.0	127
550	5.35	0.039	2.5	1.76×10^8	5.54	682.1	77
600	5.71	0.037	2.4	1.58×10^8	6.00	591.5	34

Table 4.5: Extracted parameters of p-channel buried gate 4H-SiC JFET with W/L= 100 μm/10 μm at various temperatures. g_m, R_{on}, r_o , λ and $g_m r_o$ is based on V_{GS} = 0 V. I_{Dsat}/I_{off} is the ratio of current at V_{GS} = 0 V to current at V_{GS} = 7 V.

4.7 Summary

The low voltage normally on complementary JFETs with buried gate configuration using 4H-SiC are proposed. The contact resistances between Ni/Ti/Al/TiW metal stacks and n- and p-type 4H-SiC are 3.38×10^{-4} and 1.07×10^{-3} Ω cm^2, respectively. The channel conductivity is not fully functional with applied gate bias for n-JFET. The threshold voltage at 25 ℃ is 4.39 V with low transconductance of 0.009 μS/μm. As the temperature increases, the threshold voltage shifts with the rate of 2.1 mV/ ℃. The transconductance is increased to 0.037 μS/μm with intrinsic gain of 591.5 at 600 ℃ due to the increased hole ionization. However, the kink problem at I_{DS}-V_{GS} curves and large on-resistance need to be improved for the practical use of a p-channel 4H-SiC JFET.

4.8 Reference

[1] R. Behzad, *Design of analog CMOS integrated circuits*:McGraw-Hill International Edition, 2001.

[2] P. R. Gray, P. J. Hurst, R. G. Meyer, and S. H. Lewis, *Analysis and design of analog integrated circuits*: Wiley, 2008.

[3] P. G. Neudeck, R. S. Okojie, and L.-Y. Chen, "High-temperature electronics-a role for wide bandgap semiconductors?," *Proceedings of the IEEE,* vol. 90, pp. 1065-1076, 2002.

[4] M. R. Werner and W. R. Fahrner, "Review on materials, microsensors, systems and devices for high-temperature and harsh-environment applications," *IEEE Transactions on Industrial Electronics,* vol. 48, pp. 249-257, 2001.

[5] H. K. Alexander Schmidt, Rainer Kokozinski, "Enhanced high temperature performance of PD-SOI MOSFETS in analog circuits using reverse body biasing," *IMPAS Conference & Exhibition on High Temperature Network (HiTEN 2013),* 2013.

[6] W.-C. Lien, D.-S. Tsai, D.-H. Lien, D. G. Senesky, J.-H. He, and A. P. Pisano, "4H–SiC Metal–Semiconductor–Metal Ultraviolet Photodetectors in Operation of 450 ℃," 2012.

[7] D. Clark, E. P. Ramsay, A. Murphy, D. A. Smith, R. Thompson, R. Young, J. D. Cormack, C. Zhu, S. Finney, and J. Fletcher, "High temperature silicon carbide CMOS integrated circuits," in *Materials Science Forum*, 2011, pp. 726-729.

[8] P. G. Neudeck, D. J. Spry, L.-Y. Chen, G. M. Beheim, R. S. Okojie, C. W. Chang, R. D. Meredith, T. L. Ferrier, L. J. Evans, and M. J. Krasowski, "Stable Electrical Operation of 6H–SiC JFETs and ICs for Thousands of Hours at 500," *IEEE Electron Device Letters,* vol. 29, pp. 456-459, 2008.

[9] L. Lanni, R. Ghandi, B. G. Malm, C. Zetterling, and M. Ostling, "Design and characterization of high-temperature ECL-based bipolar integrated circuits in 4H-SiC," *IEEE Transactions on Electron Devices,* vol. 59, pp. 1076-1083, 2012.

[10] H. Okumura, M. Okamoto, K. Fukuda, M. Iijima, and T. Nagano, "Controlling Characteristics of 4H-SiC (0001) p-Channel MOSFETs Fabricated on Ion-Implanted n-Well," in *Materials Science Forum*, 2012, pp. 781-784.

[11] S. Seshadri, G. Eldridge, and A. Agarwal, "Comparison of the annealing behavior of high-dose nitrogen-, aluminum-, and boron-implanted 4H–SiC," *Applied Physics Letters,* vol. 72, pp. 2026-2028, 1998.

[12] A. B. Horsfall, D. Clark, N. G. Wright, L. C. Martin, E. Ramsay, A. Murphy, R. Thompson, D. A. Smith, R. Young, and J. D. Cormack, "Charge Pumping Analysis of Monolithically Fabricated 4H-SiC CMOS Structures," in *Materials Science Forum*, 2013, pp. 891-894.

[13] D. Clark, E. P. Ramsay, A. Murphy, D. A. Smith, R. Thompson, R. Young, J. D. Cormack, and S. Finney, "High Temperature Digital and Analogue Integrated Circuits in Silicon Carbide," in *Materials Science Forum*, 2013, pp. 1065-1068.

[14] J.-S. Chen and K. T. Kornegay, "Design of a process variation tolerant CMOS opamp in 6H-SiC technology for high-temperature operation," *, IEEE Transactions on Circuits and Systems I: Fundamental Theory and Applications*vol. 45, pp. 1159-1171, 1998.

[15] H. Habib, N. G. Wright, and A. B. Horsfall, "Effects of Process Variations on Silicon Carbide Devices for Extreme Environments," in *Materials Science Forum*, 2011, pp. 401-404.

[16] S. M. Sze and K. K. NG, *Physics of semiconductor devices*: Wiley, 2007.

[17] T. Ayalew, "SiC Semiconductor Devices Technology, Modeling, and Simulation ", Technical University of Vienna, 2004.

[18] C.-M. Zetterling, *Process technology for silicon carbide devices*: IET, 2002.

[19] M. Lades, W. Kaindl, N. Kaminski, E. Niemann, and G. Wachutka, "Dynamics of incomplete ionized dopants and their impact on 4H/6H-SiC devices," , *IEEE Transactions on Electron Devices,* vol. 46, pp. 598-604, 1999.

[20] S. Greulich-Weber, M. Feege, J.-M. Spaeth, E. Kalabukhova, S. Lukin, and E. Mokhov, "On the microscopic structures of shallow donors in 6H SiC: studies with EPR and ENDOR," *Solid State Communications,* vol. 93, pp. 393-397, 1995.

[21] M. Laube, F. Schmid, G. Pensl, G. Wagner, M. Linnarsson, and M. Maier, "Electrical activation of high concentrations of N+ and P+ ions implanted into 4H–SiC," *Journal of Applied Physics,* vol. 92, pp. 549-554, 2002.

[22] A. A. Stephen E. Saddow, *Advances in Silicon Carbide Processing and Applications*, Artech House, Inc., 2004.

[23] K. Tone, J. H. Zhao, L. Fursin, P. Alexandrov, and M. Weiner, "4H-SiC normally-off vertical junction field-effect transistor with high current density," *IEEE Electron Device Letters,* vol. 24, pp. 463-465, 2003.

[24] M. V. Rao, J. B. Tucker, M. Ridgway, O. Holland, N. Papanicolaou, and J. Mittereder, "Ion-implantation in bulk semi-insulating 4H–SiC," *Journal of Applied Physics,* vol. 86, pp. 752-758, 1999.

[25] C. Chang, Y. Fang, and S. Sze, "Specific contact resistance of metal-semiconductor barriers," *Solid-State Electronics,* vol. 14, pp. 541-550, 1971.

[26] D. Planson, C. Raynaud, M. Lazar, D. Tournier, M. Soueidan, and D. M. Nguyen, "Process Optimization for High Temperature SiC Lateral Devices," in *Materials Science Forum*, 2009, pp. 585-588.

Chapter 5

Conclusion and Future Work

5.1 Contributions of This Work

Integrated SiC UV sensing chips are promising candidates for the real time condition monitoring of power systems and for space exploration. This dissertation addresses the two building blocks of the sensing system, namely UV sensor and transistor.

Conventional SiC pn photodiodes show stable performance and high responsivity up to 300 ℃. However, the extra thin film deposition for the specific junction doping concentration might hinder the development of an integrated sensing chip. An integrated compatible SiC metal-semiconductor-metal UV sensor has been designed, fabricated and characterized. High temperature tests confirm that the MSM PD can work up to 400 ℃ and possibly extend the temperature to 450 ℃. The speed measurement was conducted at 400 ℃ and the MSM photodetector shows a fast response time, able to detect the flicker frequency of flame in combustion engine [1].

To further explore the possibility of integrating the whole UV sensing system, a junction field effect transistor was chosen to evaluate the ability to design the transimpedance amplifier, which can convert photocurrent generated from MSM PD to voltage. While most SiC JFETs for low voltage amplifier application use 6H-SiC, few works discuss the performance of low power JFET using 4H-SiC [2]. Most device research on 4H-SiC target the high power electronics, such as vertical JFET, MOSFET and BJT. Given the largest SiC wafer manufacture, Cree Inc., has announced to shut down the production line of 6H-SiC, it is worth investigating the performance of 4H-SiC JFET at elevated temperatures. A lateral, depletion mode, low voltage n-channel 4H-SiC JFET has been design, fabricated and completely characterized in the temperature range of 25 to 600 ℃. High transconductance and on/off drain saturation current, decent output resistance and low on-resistance suggest that 4H-SiC is suitable for the high temperature electronics. The complete model of the SPICE DC level 1 for n-channel raised 4H-SiC JFET has been developed which is beneficial for the future analog circuit design.

Finally, the complementary JFET was proposed in order to add the flexibility to amplifier circuit design and increase the bandwidth of the amplifier. The first prototype of cJFET is designed using a buried gate configuration in order to reduce the number of fabrication steps. The fabricate n-channel buried gate JFET has the problem of being completely turn-off even at a gate bias of 10 V. The p-channel buried gate JFET was characterized up to 600 ℃. The transconductance at room temperature is fairly low due

to the low mobility and low degree of ionization of holes. As the ambient temperature increased to 600 C, more than 90 % of acceptor carries were ionized and thus boost the transconductance value of p-channel JFET.

5.2 Integrated SiC Sensor Design Challenges

Many challenges must be addressed for further integrated SiC sensor development. The lists below highlight some of the fundamental problems.

Semiconductor device modeling for JFET. The simulation model built with Synopsys Sentaurus in this work cannot completely match the measured data of both raised and buried gate configurations. More specifically, the simulated device exhibits the ultra low leakage current (< 10^{-15} A) and small subthreshold swing (~74 mV/dec), suggesting that more non-ideal parameters should be taken into account in the future TCAD simulations.

Fabrication complexity. This includes the challenge of precise time-etched process to define the device structure, usually the thickness of the channel. This is crucial for fabricating the complementary devices, which usually entail multiple etching processes of epitaxial layers. Failure to control the etch thickness of SiC will result in different electrical properties than the designed value. Furthermore, a stable annealing cap is required for activating the implanted p-type dopants with an annealing temperature greater than 1500 ℃.

Complementary Device Geometry. It seems that the raised gate JFET has a greater chance of success and more stable performance at extreme high temperature, most likely due to the epitaxially grown gate having better crystallinity than the implanted gate. However, it is very challenging to integrate the complementary devices if both of them are raised gate configuration. One possible solution would be to use the back gate configuration [3, 4]. The advantage of this configuration is using the epitaxially grown gate and also reducing the chance of using ion implantation to facilitate the Ohmic contact between the contact metal and the source/drain area. The disadvantage is that this geometry requires many steps in the precise time-etched process described earlier.

Metallization. In order to integrate the MSM UV sensor and JFET into the same fabrication process, it is important to have the contact metal forming an Ohmic contact with n^+ or p^+ area for JFET and Schottky contact with low doped film for MSM PDs at the same time. Currently, there are very few candidates able to achieve this requirement with high thermal stability for high temperature operation. A novel tungsten-nickel alloy seems to show promising preliminary results for both n- and p-type 4H-SiC [5]. More studies on metallization are needed in the future.

5.3 Reference

[1] D. M. Brown, E. Downey, J. Kretchmer, G. Michon, E. Shu, and D. Schneider, "SiC flame sensors for gas turbine control systems," *Solid-State Electronics,* vol. 42, pp. 755-760, 1998.
[2] A. B. Horsfall, N. G. Wright, H. K. Chan, J. P. Goss, and R. C. Stevens, "Reliability Evaluation of 4H-SiC JFETs Using IV Characteristics and Low Frequency Noise," in *Materials Science Forum*, 2013, pp. 934-937.
[3] S. Zappe, M. Leone, F. Yang, and E. Obermeier, "Characterisation of silicon carbide JFETs with respect to microsystems for high temperature applications," *Microsystem Technologies,* vol. 3, pp. 134-138, 1997.
[4] F. McLean, C. Tipton, J. McGarrity, and C. Scozzie, "Modeling the electrical characteristics of n-channel 6H–SiC junction-field-effect transistors as a function of temperature," *Journal of Applied Physics,* vol. 79, pp. 545-552, 1996.
[5] R. S. Okojie, L. J. Evans, D. Lukco, and J. P. Morris, "A Novel Tungsten–Nickel Alloy Ohmic Contact to SiC at 900," *IEEE Electron Device Letters,* vol. 31, pp. 791-793, 2010.